AD-A075 320 EFFECTS TECHNOLOGY INC SANTA BARBARA CA F/G 14/2
TRI-THE DEVELOPMENT OF A FAST-RESPONSE TIME-RESOLVED IMPULSE GA--ETC(U)
APR 78 W M ISBELL, W J NAUMAN DNA001-76-C-0357
UNCLASSIFIED ETI-CR-78-550 DNA-4658F NL

1 OF 2
AD
A075320

AD-E300 592

(12) LEVEL III

NW

DNA 4658F

# TRI-THE DEVELOPMENT OF A FAST-RESPONSE TIME-RESOLVED IMPULSE GAGE

AD A075320


W.M. Isbell

W.J. Naumann

Effects Technology, Inc.

5383 Hollister Avenue

Santa Barbara, California 93111




30 April 1978

Final Report for Period 29 July 1976—30 April 1978

CONTRACT No. DNA 001-76-C-0357

APPROVED FOR PUBLIC RELEASE;
DISTRIBUTION UNLIMITED.


THIS WORK SPONSORED BY THE DEFENSE NUCLEAR AGENCY UNDER RDT&E RMSS CODE B34207T462 J11AAXAX00232 H2590D.




Prepared for

Director

DEFENSE NUCLEAR AGENCY

Washington, D. C. 20305

(18) DNA, SBIE

UNCLASSIFIED

SECURITY CLASSIFICATION OF THIS PAGE (When Data Entered)

| (19) REPORT DOCUMENTATION PAGE | | READ INSTRUCTIONS BEFORE COMPLETING FORM |
|---|---|---|
| 1. REPORT NUMBER<br>DNA 4658F, AD-E300 592 | 2. GOVT ACCESSION NO. | 3. RECIPIENT'S CATALOG NUMBER |
| 4. TITLE (and Subtitle)<br>(6) TRI—THE DEVELOPMENT OF A FAST-RESPONSE TIME-RESOLVED IMPULSE GAGE, | | 5. TYPE OF REPORT & PERIOD COVERED<br>(9) Final Report for Period 29 Jul 76—30 Apr 78,<br>6. PERFORMING ORG. REPORT NUMBER<br>CR-78-550 |
| 7. AUTHOR(s)<br>(10) W. M. Isbell<br>W. J. Naumann<br>62710H | | 8. CONTRACT OR GRANT NUMBER(s)<br>(15) DNA 001-76-C-0357 new |
| 9. PERFORMING ORGANIZATION NAME AND ADDRESS<br>Effects Technology, Inc.<br>5383 Hollister Avenue<br>Santa Barbara, California 93111 | | 10. PROGRAM ELEMENT, PROJECT, TASK AREA & WORK UNIT NUMBERS<br>(16) [redacted] J11AAXA[redacted] |
| 11. CONTROLLING OFFICE NAME AND ADDRESS<br>Director<br>Defense Nuclear Agency<br>Washington, D.C. 20305<br>(17) X002, (11) | | 12. REPORT DATE<br>30 Apr[redacted]78<br>13. NUMBER OF PAGES<br>124 |
| 14. MONITORING AGENCY NAME & ADDRESS (if different from Controlling Office)<br>(12) 124 | | 15. SECURITY CLASS (of this report)<br>UNCLASSIFIED<br>15a. DECLASSIFICATION/DOWNGRADING SCHEDULE |

16. DISTRIBUTION STATEMENT (of this Report)

Approved for public release; distribution unlimited.

DDC
RECEIVED
OCT 23 1979
B

17. DISTRIBUTION STATEMENT (of the abstract entered in Block 20, if different from Report)

(14) ETI-CR-78-550

18. SUPPLEMENTARY NOTES

This work sponsored by the Defense Nuclear Agency under RDT&E RMSS Code B34207T462 J11AAXAX00232 H2590D.

19. KEY WORDS (Continue on reverse side if necessary and identify by block number)

| | |
|---|---|
| Impulse Measurement | V&H Assessment |
| UGT Instrumentation | AGT Instrumentation |
| Tamping Experiments | High Temperature EOS |

approximately

20. ABSTRACT (Continue on reverse side if necessary and identify by block number)

A time-resolved impulse gage was developed to provide data to fill the gap between the longest duration stress gages (∿5 μsec max.) and the fastest of the recoil gages (∿50 μsec min.). The characteristics of the new gage include: impulse range 0.5 to 20 ktaps, risetime 10-15 μsec, read time 300-1500 μsec, accuracy ±10%, electrical output 1.32 volt/ktap.

+ or - microSec

The gage was specifically developed to record the pressure-time history of "tamped" UGT experiments, where metallic vapors produced by rapid energy (over)

DD FORM 1 JAN 73 1473 EDITION OF 1 NOV 65 IS OBSOLETE

UNCLASSIFIED

SECURITY CLASSIFICATION OF THIS PAGE (When Data Entered)

405 842

| SECTION | | PAGE |
|---|---|---|
| VIII | GAGE CALIBRATION AND DATA ANALYSIS................. | 103 |
| IX | CONCLUSIONS.............................................. | 113 |
| X | ACKNOWLEDGEMENTS.................................... | 116 |
| | REFERENCES............................................. | 117 |

## LIST OF ILLUSTRATIONS


| FIGURE | | PAGE |
|---|---|---|
| 1 | Photographs of the field version of the TRI gage system | 10 |
| 2 | Typical output of the TRI gage. Input pulse duration $\leq$10 μsec. Risetime 13 μsec. Sensitivity 1.32 volts/ktap (7.0 mv/cm/sec) | 11 |
| 3 | Schematic of the tamping experiment. Note the use of logarithmic pressure and time scales and the linear impulse scale | 15 |
| 4 | Roadmap of the development program | 18 |
| 5 | Pellet impact system for testing impulse gages | 20 |
| 6 | Schematic of the bar impact device used to load gages | 21 |
| 7 | Wave at specimen/bar interface. Specimen leaves bar on or before first "pullback" | 21 |
| 8 | Oscillograph of three bar impact tests showing reproducibility of gage and of impact system. Note that this output is from an early version of the gage when gage vibrations were still very pronounced | 23 |
| 9 | Reproducibility of gage to impulses varying by a factor of ∿2.5 is shown in this normalized plot of gage output | 23 |
| 10 | Schematic of laser test arrangement and sample of deposition pulse seen by gage | 25 |
| 11 | Output of gage from typical laser test. Impulse is only 0.034 ktaps (early version of gage) | 27 |
| 12 | Basic elements of the time-resolved impulse (TRI) gage | 30 |
| 13 | Gaps, gaps, and more gaps. The angle of the specimen/guardring gap is exaggerated for visualization | 33 |
| 14 | Gage positions at times of prompt impulse (a) and later (tamped) impulse, (b) showing gage and tamper motion and leakage of gas around gage | 38 |

| FIGURE | | PAGE |
|---|---|---|
| 45 | The effect of a small diameter specimen sampling only the higher fluence center of the beam is demonstrated by the difference in recorded impulse..... | 96 |
| 46 | The sample contaminated with adhesive produced ∿65% more impulse.................................... | 97 |
| 47 | The "reverse tamper" arrangement (47a) tested the tamper for jamming by the impact of molten metal on its surface. The "gas flow" arrangement (47b) measured the expansion of gases towards regions of lower pressure.................................... | 99 |
| 48 | Passive weld test with tantalum sample ............... | 101 |
| 49 | Schematic of the precision drop assembly to calibrate the gage magnets....................................... | 105 |
| 50 | Calibration curve for an early magnet system showing the method of fitting the data......................... | 108 |
| 51 | An example of the ability of the FFT analysis to eliminate vibrations caused by gage from the data...... | 112 |

# SECTION I
# INTRODUCTION

This report describes the development of a time-resolved gage for measurement of impulse in underground nuclear test environments. The development program was conducted by Effects Technology, Inc. (ETI) for the Defense Nuclear Agency (Mr. Donald Kohler, COR) in support of specific underground nuclear test experiments designed by the Lawrence Livermore Laboratory (LLL) and ETI.

Although the program has resulted in a gage designed to meet certain requirements peculiar to the planned experiments, the basic gage design is adaptable to general experimentation requiring measurement of impulse resolved on a 10-15 μsec time scale. The gage exhibits good linearity, high electrical output, and a wide dynamic range. Possible utilizations of the gage besides UGT experimentation include electron-beam and laser effects studies.

## SECTION II
## BACKGROUND

Several classes of problems dealing with the response of materials to rapid heating from energy deposition require measurement of the impulse imparted to the material or structure by the melting and/or vaporization of its surface. A variety of impulse-measuring gages have been developed, falling into four basic categories:

1. Stress gages, such as quartz piezoelectric gages and carbon piezoresistive gages, which provide the early time stress-time history of a front-surface pulse transmitted through a specimen into a gage mounted at the specimen rear surface. Integration of the gage output provides the impulse delivered during the gage active time (usually 1-5 μsec).

2. Recoil type impulse gages, in which the total impulse delivered to a specimen is calculated by measuring the final velocity of a relatively heavy mass set into motion by the ejection of liquid or gases from a rapidly-heated specimen mounted on the front surface.

3. Recoil type gages which, by using a relatively light mass capable of responding to changes in impulse generation rate, measure the time-resolved impulse generated at the specimen surface.

4. Other measuring techniques for measuring total and/or time-resolved impulse such as the split-Hopkinson's bar impulse gage and diaphragm/strain gage systems.

There has consistently been a gap between the time coverage of the longest duration stress gages (∿5 μsec max.) and the fastest of the recoil gages (∿50 μsec min.). This has not proven particularly troublesome with experiments on most materials and in most experimental configurations, since total impulse is typically delivered in a few microseconds. The inability to gather impulse data in the 5-50 μsec time frame became critical, however, on a series of UGT experiments proposed for a "tamped" configuration where a "prompt" impulse delivered in 2-4 μsec is followed by a "late-time" impulse delivered in substantially longer times.

The measurements of impulse to be made on these experiments include both total impulse and impulse resolved on a 10-15 μsec time scale. Thus it was necessary to provide a measurement of impulse beginning in time as close as possible to the 5 μsec furnished by the stress gages and extending to at least 200 μsec. The gage must be capable of operating in a high-radiation environment, deliver an adequate signal for recording in an underground test and must be designed to accommodate the high-Z metal specimens of interest without self-welding by condensation of molten metal originating at the specimen surface.

Such a gage, designated the TRI (Time-Resolved-Impulse) gage, was designed and laboratory proof-tested in readiness for fielding. Photographs of the assembled and disassembled gage are shown in Figure 1. The characteristics of the gage are listed in Table I, and an example of the gage response to a short duration ( <10 μsec) impulse is shown in Figure 2.

A caveat must be inserted here regarding the operation of the gage under actual test conditions. Although extensive testing has been performed on the TRI gage to confirm its characteristics, it has not yet been possible to duplicate in the laboratory the actual high stress, short

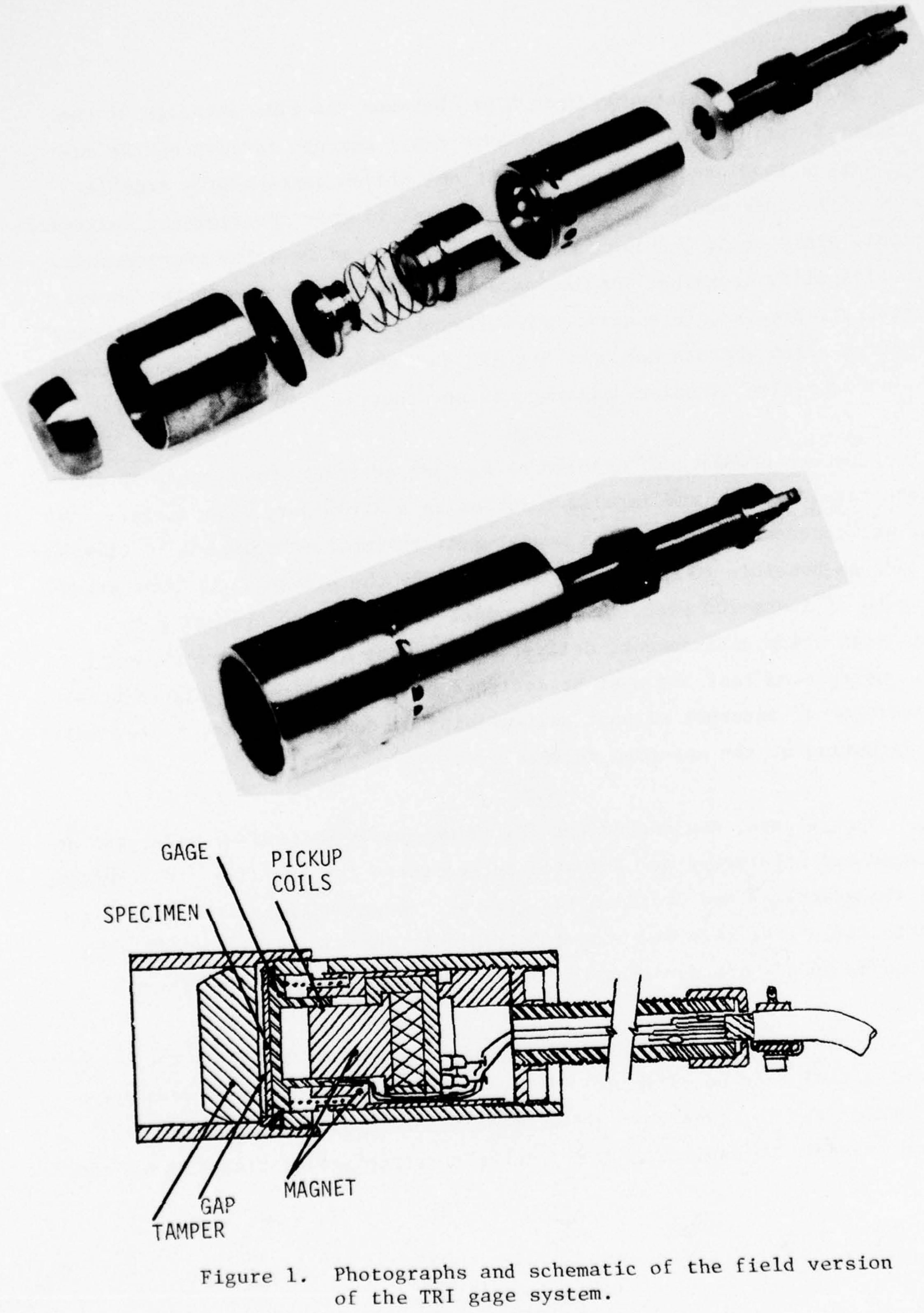


Figure 1. Photographs and schematic of the field version of the TRI gage system.

BAR'IMPACT TEST OUTPUT ON SST-4 . . .

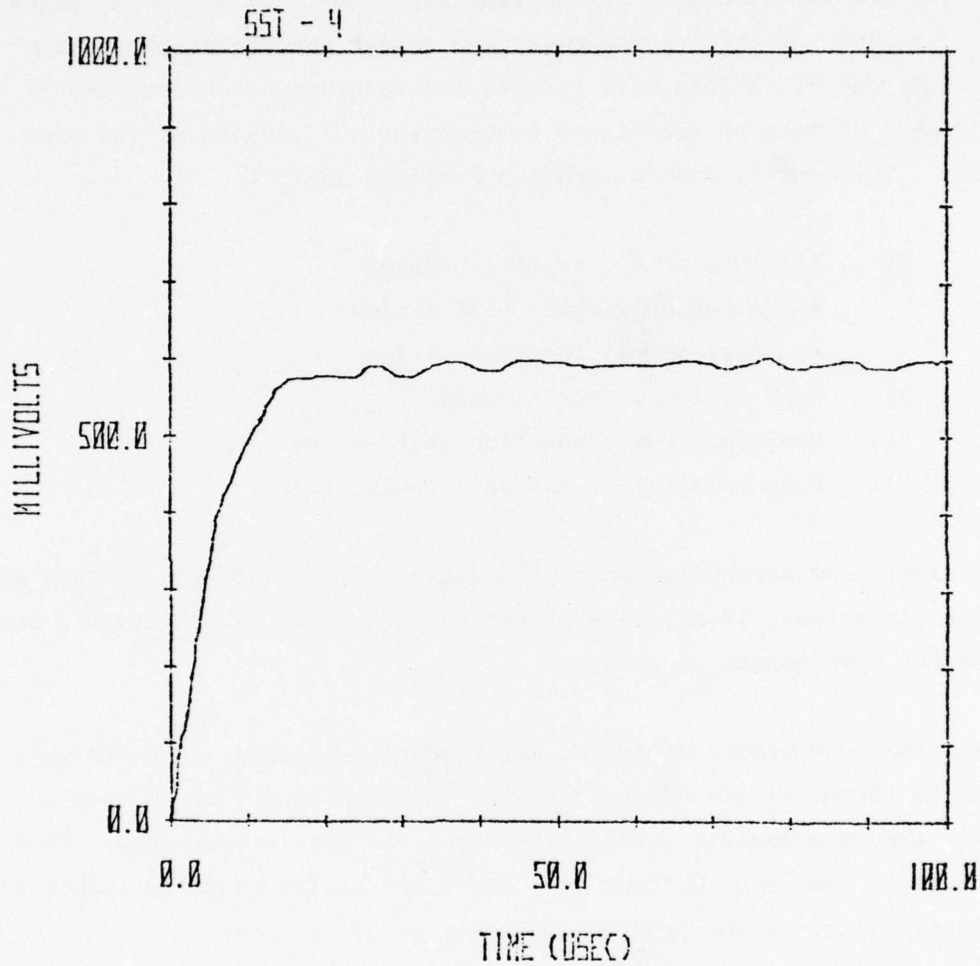


Figure 2. Typical output of the TRI gage. Input pulse duration ≤10 μsec. Risetime 13 μsec. Sensitivity 1.32 volts/ktap (7.0 mv/cm/sec).

duration pulses induced by x-ray deposition underground. Until the gage is actually tested in a UGT radiation environment, the risetime and signal to noise ratios quoted in Table I will remain unconfirmed.

This report describes the development of the TRI gage to its present form. Section III discusses the tamping experiments in which the gages will be fielded. Section V presents gage design considerations, while Sections IV and VI through VIII discuss the testing and calibration of the gage using a variety of techniques to test various aspects of the gage response. The testing and calibration Sections include:

- IV Elements of the testing program
  - Mechanical impact test series
  - Laser deposition test series
- VI High explosive test series
- VII Electron-beam deposition test series
- VIII Gage calibration and data analysis.

Data analysis and deconvolution of the data to remove non-linearities and periodic vibrations, if any, are presented in Section IX. Section X summarizes the development program.

For the convenience of the casual reader, Section V (Gage Design), and Section IX (Summary) provide most of the information one would need to evaluate the experimental configuration and the gage performance. Section VII (Electron Beam Test Series) also contains results of measurements of the generation of tamped impulse which may be of interest.

TABLE 1

- Impulse range 0.5 to 20 ktaps*
- Risetime 10-15 μsec
- Read time 300-1500 μ sec, depending on the impulse level recorded
- Absolute accuracy ±10%
- Signal to noise ratio >10:1
- Sensitivity 7.0 mv/cm/sec
- Electrical output for nominal configuration 1.1 volt/ktap
- Linearity 5% absolute, 2% after deconvolution of record

---

*1 ktap = 1000 dyne-sec/$cm^2$ = 100 newton-second/$m^2$.

## SECTION III

## CONFIGURATION OF THE UGT EXPERIMENT

A schematic of the experimental configuration to be fielded is shown in Figure 3. Radiation from the nuclear source penetrates the low-Z "tamper" and is deposited in the high-Z specimen. The rapid deposition of energy causes melting and vaporization of the specimen surface and creates a shock wave which propagates through the specimen and into the gage.

Approximately 60% of the impulse delivered to the specimen surface is created by the initial, short duration impulse as the vaporized and molten material expands. The additional 40% of the impulse occurs over a much longer time, as the hot metallic gases, entrapped between the specimen and tamper, perform a near-adiabatic expansion of the interior volume. The tamper and gage move in reaction to the time-dependent pressure generated at their surfaces, and gage velocity, as measured by the passage of the gage coils through a magnetic field, provides a time-resolved measurement of this pressure.

Schematic representations of the pressure-time history calculated for the gage surface, and the resultant velocity-time histories of the gage and tamper are also shown in Figure 3. Note that the conditions described are hardly conducive to smooth gage operation. The gage is initially shocked and expanded by the passage of a high amplitude stress wave. Molten metal under pressure is forced through gaps between gage components, threatening both welding and jamming of the gage and tamper. High pressure metallic vapors may leak past seals, lowering the pressure within the interior volume below that of the ideal case. Finally, the gage must respond to the late-time low pressure component with equal accuracy as to the component several orders of magnitude higher in amplitude.

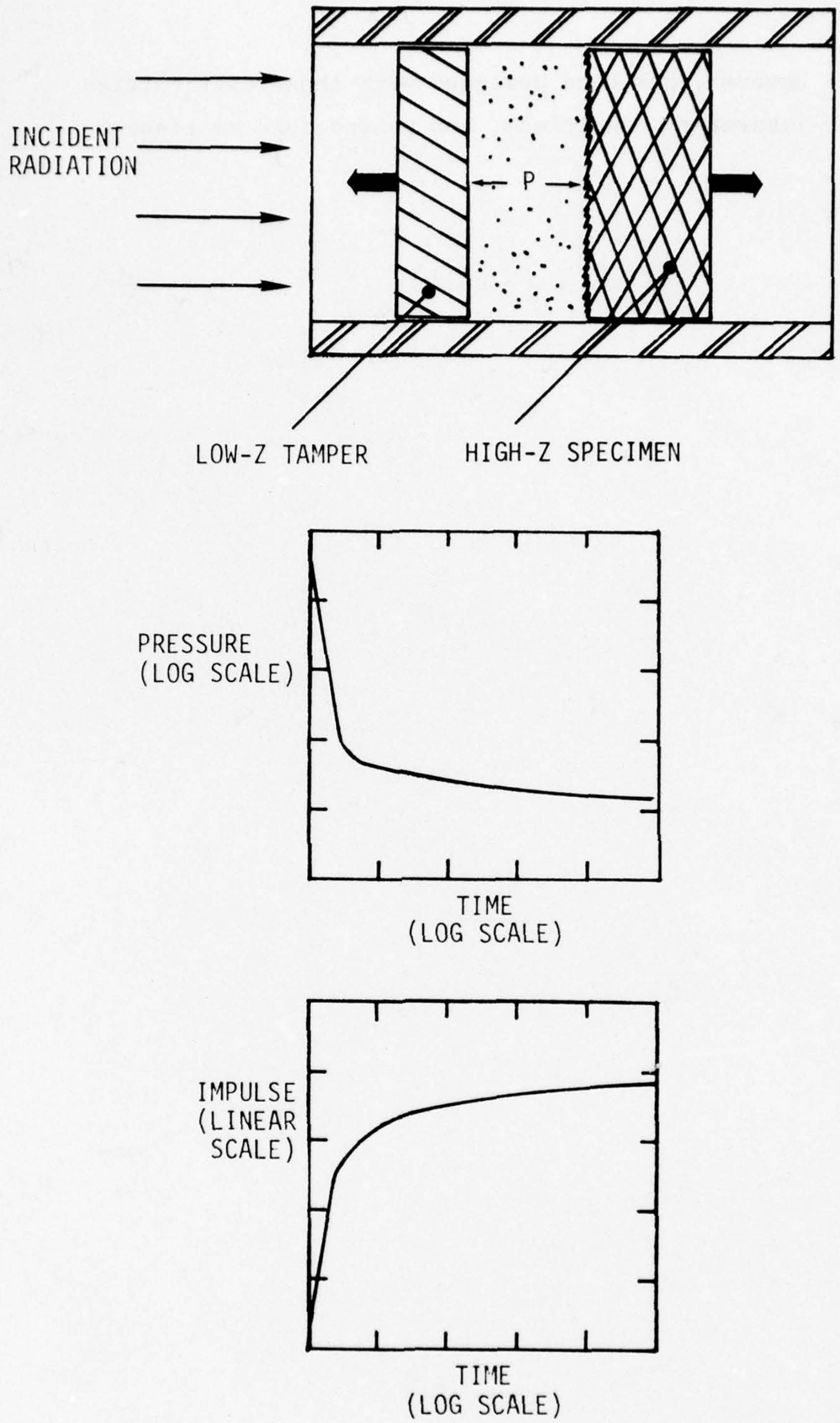


Figure 3. Schematic of the tamping experiment. Note the use of logarithmic pressure and time scales and the linear impulse scale.

The TRI gage however, has been designed with these difficulties in mind and, under laboratory conditions, has proved able to respond satisfactorily.

## SECTION IV
## ELEMENTS OF THE TESTING PROGRAM

Figure 4 provides a roadmap of the paths followed during the development program. The characteristics of the gage necessary to meet the experimental requirements of the underground test were decided upon jointly by the ETI, MDAC, and LLL groups associated with the test. A prototype gage design was then manufactured and tested using mechanical impact, electron-beam, and pulsed laser beam sources of loading. The problems explored with the prototype gage testing series included gage vibration, gas leakage, welding, nonlinearity, gage risetime, etc.

Once the basic characteristics of the gage were measured, two paths to the final gage package were followed. A redesign (actually, numerous redesigns) was made to eliminate undesirable characteristics such as gage vibration and low electrical output. Secondly, a deconvolution technique was developed to remove remaining nonlinearities and periodic vibrations from the analyzed record using Fast Fourier Transform (FFT) techniques. The result of the effort was a gage design thought capable of meeting the exacting requirements of the UGT experiment and a data reduction system for calibrating the gages before testing and reducing the data after testing.

The next two subsections of the report briefly describes two of the testing techniques, mechanical impact testing and pulsed laser testing. High explosive proof testing of the field version of the gage is described in Section VI and, electron beam testing, which requires more extensive explanation than the first two techniques, is described in Section VII.

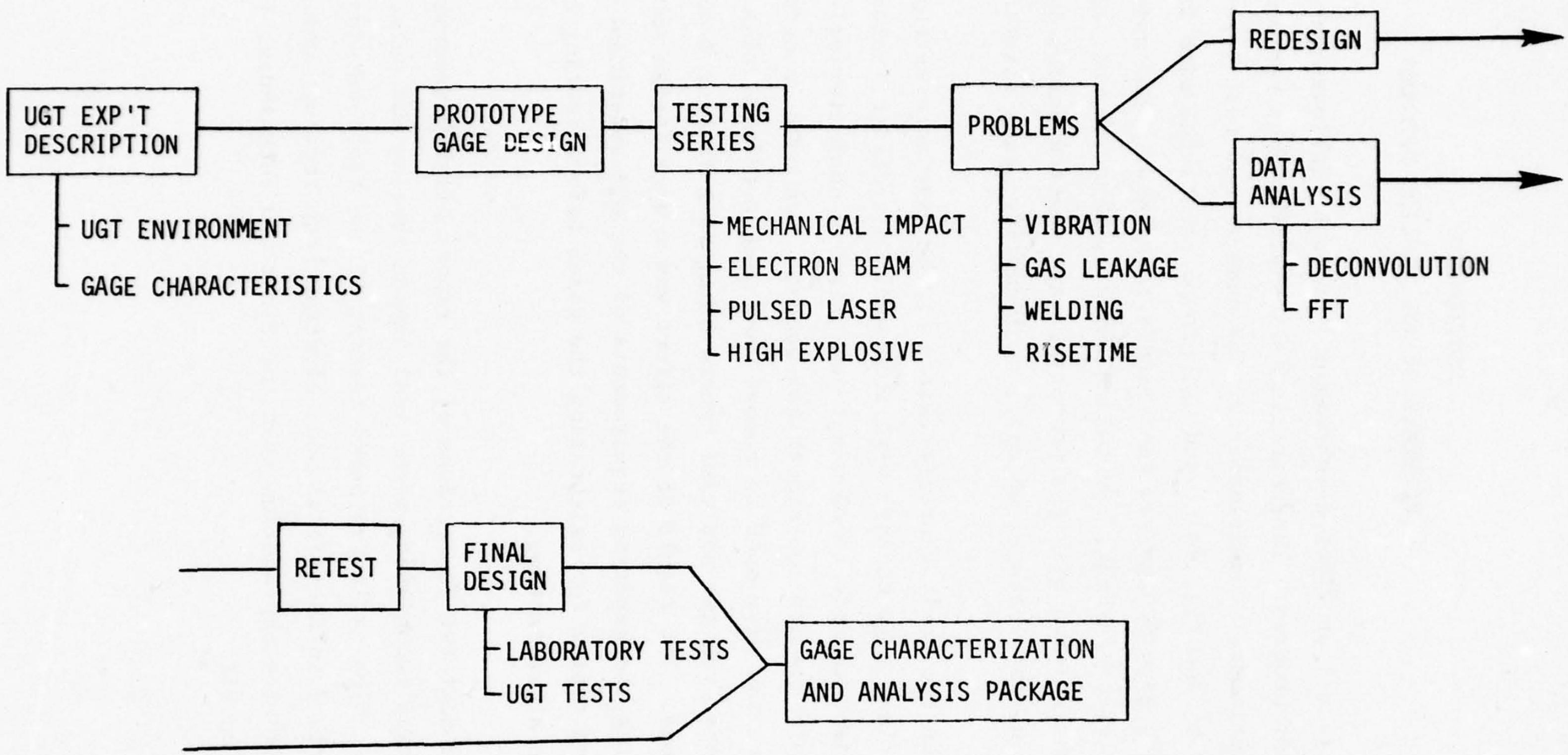


Figure 4. Roadmap of the development program.

MECHANICAL IMPACT TESTING

Because of the large number of tests contemplated for a wide variety of gage parameters to be varied, it was necessary to develop an inexpensive, rapid turn-around, repeatable source of impulsive loading for the gage assembly. After examination of several alternatives, two techniques were chosen for further study.

The pellet gun device shown in Figure 5 was tested first and provided impulses in the range of 1 to 3 ktaps. While reasonably reproducible results were obtained, the arrangement had several deficiencies:

1. Projectile velocity was not repeatably variable over the entire velocity range.

2. Projectile velocity decreased with each test as the $CO_2$ cartridge was depleted.

3. The relatively high velocity (0.10 to 0.25 mm/μsec) pellet caused sufficient specimen surface damage that the specimen periodically needed replacement.

4. The small diameter of the pellet, compared to the diameter of the gage, caused cocking of the gage assembly when the impact was slightly off the centerline.

The second apparatus, referred to as the "bar device," was substantially more successful. Figure 6 shows the bar device schematically. A 10 cm long steel bar (the striker) with the impact end ground to a large

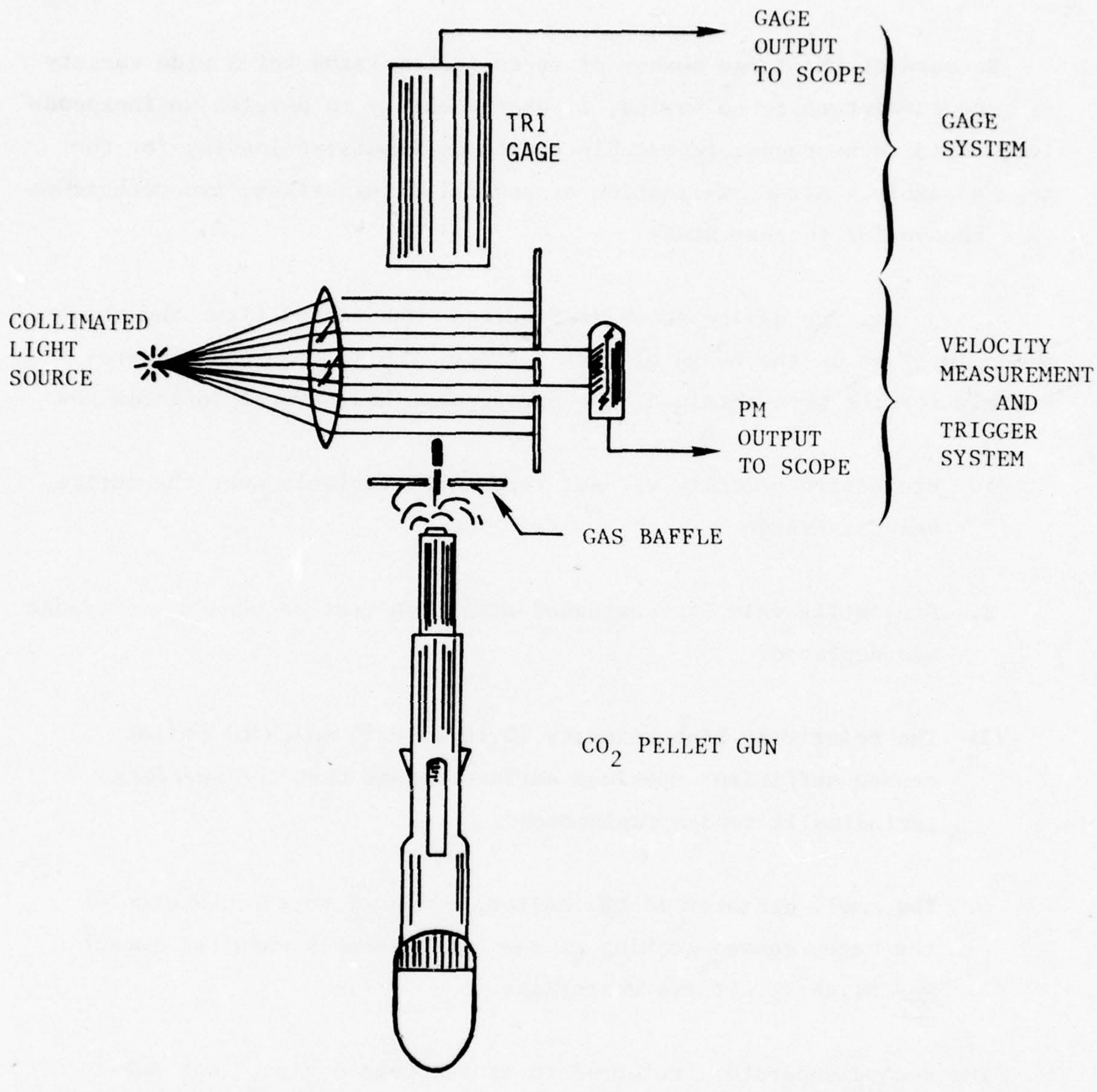


Figure 5. Pellet impact system for testing impulse gages.

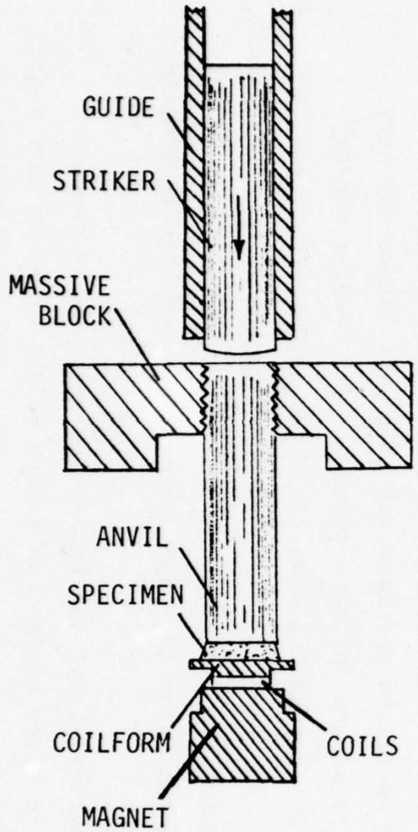


Figure 6. Schematic of the bar impact device used to load gages.

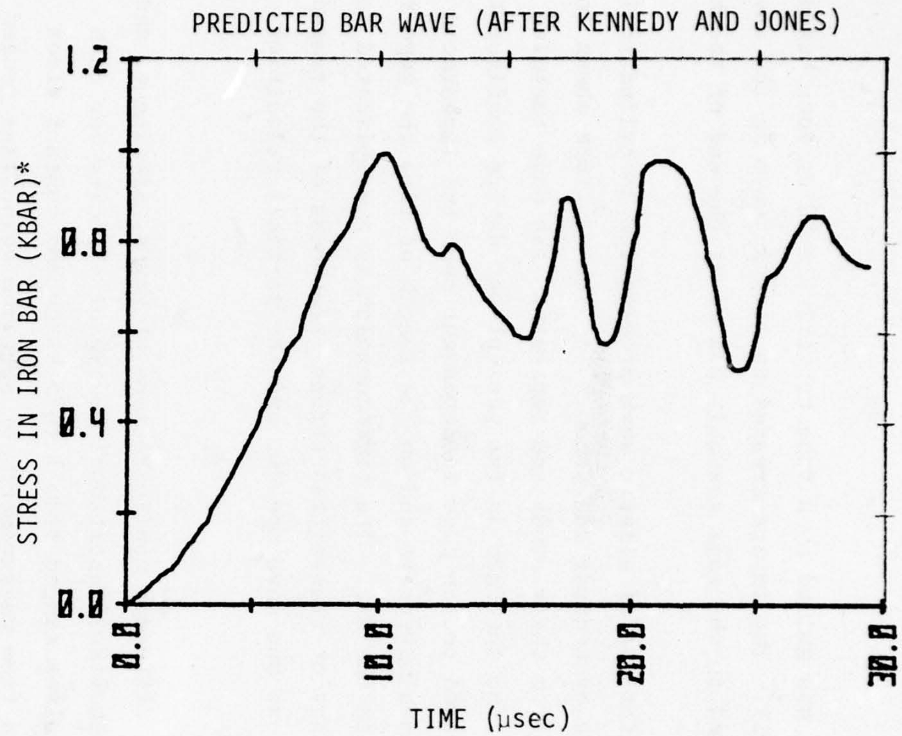


Figure 7. Wave at specimen/bar interface. Specimen leaves bar on or before first "pullback."

* 1 kbar = 0.1 GPa

radius of curvature was guided by a tube to strike a 10 cm long hardened steel bar (the anvil). The impact created an elastic wave in the anvil which was transmitted to the gage assembly placed at the end of the bar.

Extensive calculations of elastic wave propagation in cylindrical bars have been made by Kennedy and Jones.[1] The waveform shown in Figure 7 is taken from their study and represents the wave emerging from the anvil into the specimen in the present bar device configuration. The impulse transmitted to the gage is dependent upon the impedances of the anvil and specimen materials and on the length of time the gage remains in contact with the bar. The time duration is a complicated function of rate of change of transmitted stress (steepness of the ramped wave), gage dimensions and wave speeds, and the particle velocities induced in the gage.

Tests made with different configurations of gages, specimens, and drop heights gave impulses proportional to impact velocity for each configuration. Impulses ranged from 1 to 5 ktaps and contact times (risetimes) inferred from measurements of specimen velocities ranged from 5 to 10 μsec.

The diameter of the anvil was the same as the diameter of the specimen. The anvil and specimen surfaces were lapped and very lightly oiled to assure intimate contact. The "self-righting" feature of waves propagating down long bars assures that, even if the impact does not occur precisely along the centerline of the anvil, the wave emerging from the anvil end will be symmetrical about the centerline. Rotation of the gage during its travel was thus minimal.

The reproducibility of the bar device and gage is shown in Figure 8 where three tests from a drop height of 90 cm show nearly identical results. Figure 9 indicates the reproducibility of the

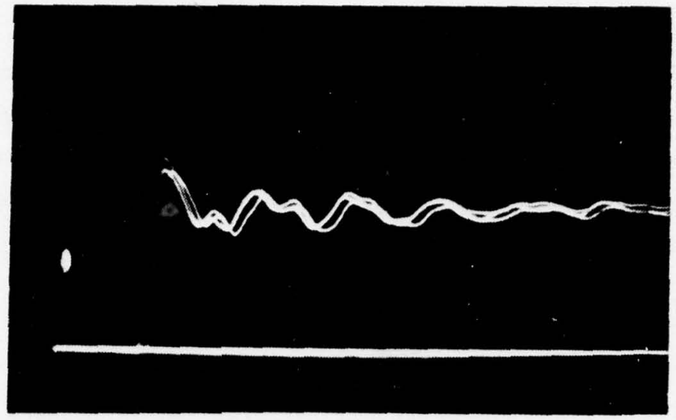

Figure 8. Oscillograph of three bar impact tests showing reproducibility of gage and of impact system. Note that the output is from an early version of the gage when gage vibrations were still very pronounced.

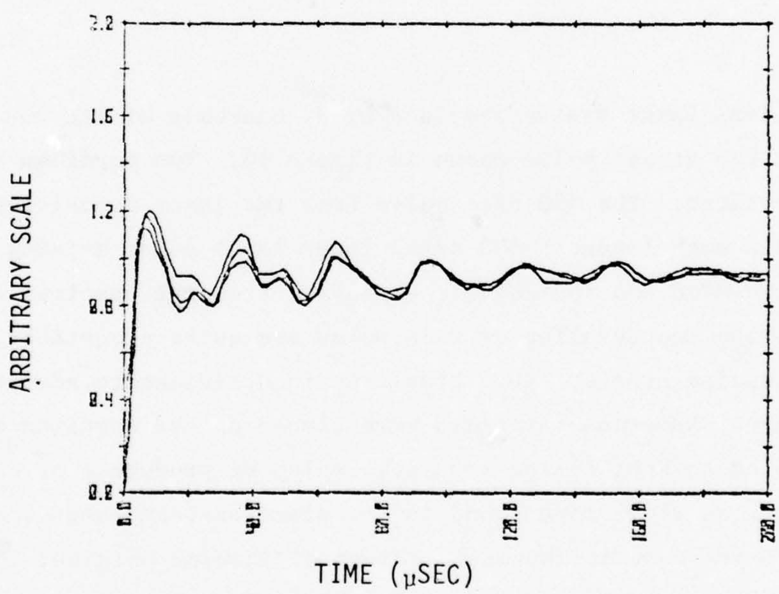


Figure 9. Reproducibility of gage to impulses varying by a factor of ∿2.5 is shown in this normalized plot of gage output.

gage to respond to different impulses. Records from tests with drop heights of 30, 90, and 180 cm were digitized and then normalized to constant final output. The outputs are seen to be similar when the impulse is varied by a factor of $\sim$2.5. During the course of the program some 500-600 tests were performed with the bar device.

## Pulsed Laser Testing

The 5-10 μsec risetime of the bar device was not sufficiently short compared to the gage response time to approximate the step (or delta) input needed to determine the true gage risetime. The much shorter pulse arising from laser deposition on the gage surface seemed likely to be a more definitive testing technique if sufficient impulse ($\geq$1 ktap) could be created at beam diameters comparable to the specimen diameter ($\sim$2.5 cm).

A Nd:Glass laser system provided by J. Dzakowic of LLL was used to generate the stress pulse shown in Figure 10. Two portions to the pulse are evident. The $\sim$30 nsec pulse from the laser deposition is followed by a much longer ($\sim$300 nsec) lower level pulse arising from the rapidly heated and ionized air expanding from the specimen surface. While the shape and duration of this pulse are quite acceptable, the low total impulse created ($\leq$0.4 ktap) was insufficient to adequately test the gage. Numerous materials were placed on the specimen surface and irradiated to enhance the impulse, including producers of gaseous products such as vinyl tape (found in the electron-beam tests to provide considerable increase in impulse). Values of impulse obtained for the same nominal input beam ranged from 0.4 ktaps for vinyl tape to 0.02 ktaps for ATJS graphite.

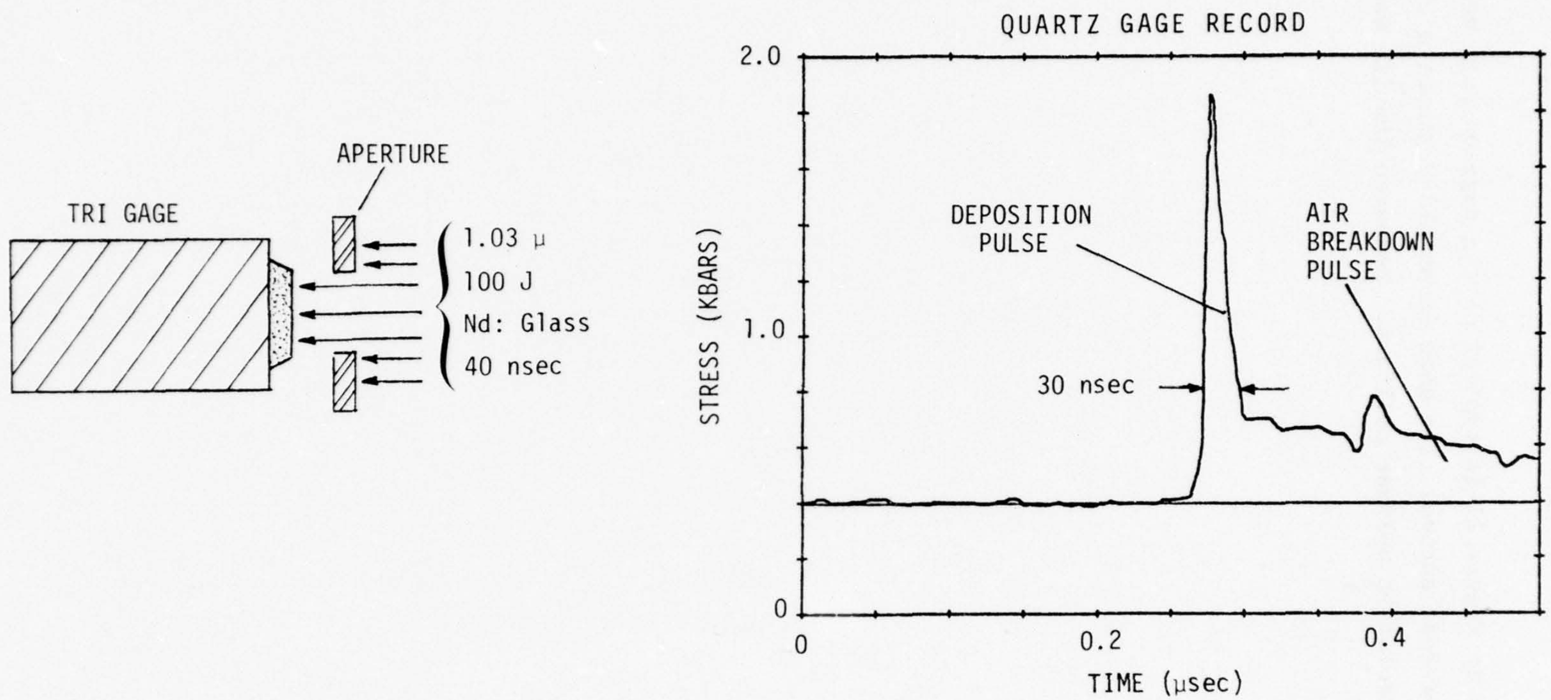


Figure 10. Schematic of laser test arrangement and sample of deposition pulse seen by gage.

The record in Figure 11 is typical of the gage outputs measured during the laser test series. The gage is an ATJ-S graphite cylinder with an early prototype polymer coilform. Measured impulse was 0.034 ktaps.

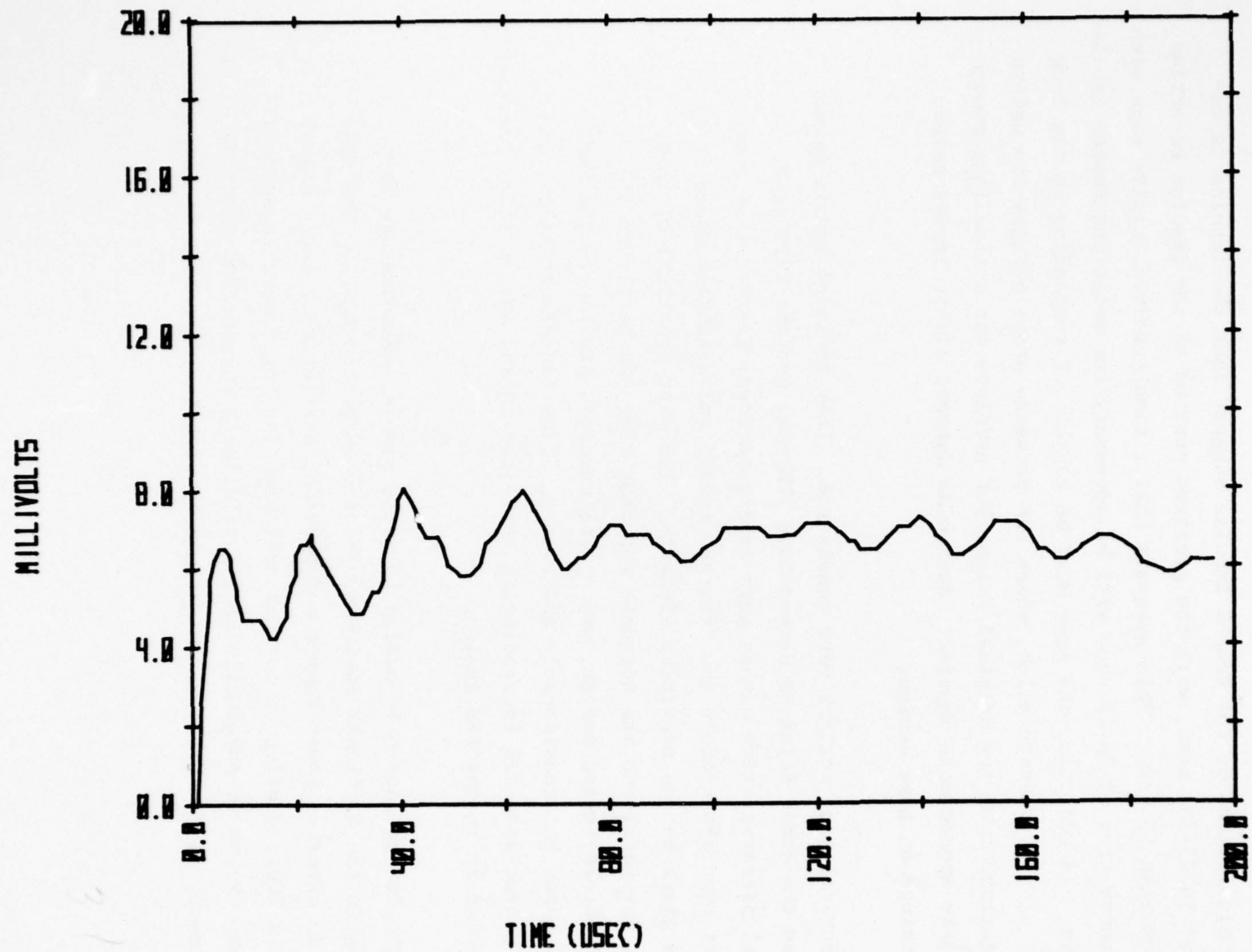


Figure 11. Output of gage from typical laser test. Impulse is only 0.034 ktaps (early version of gage).

## SECTION V
## GAGE DESIGN

Calculations of the tamped impulse suggest that the impulse is delivered in 25-200 μsec, with the greatest portion of the impulse occurring in less than 50 μsec. This suggests that a time-resolved impulse gage with a response time of 10-25 μsec will be necessary for measuring tamped impulse effects. In addition, the gage must be capable of responding to the long "tail" of the pressure pulse, where the pressure drops perhaps two orders of magnitude from its original value, but persists for a time long enough to create appreciable impulse. Such wide dynamic limits impose severe constraints on gage design.

Several gage designs were considered. They included recoil gages such as the Kaman Sciences Corporation FEM gage and the TRIM gage, special piezoresistive carbon gage configurations, Kistler-type gages (quartz crystals used in the "charge" mode), and diaphragm gages using strain gages as the sensitive elements. The most practical of these gages, due partly to its adequate response time and partly to its already field-tested design, was a configuration similar to the FEM recoil gage, but considerably modified to allow for electrically conducting specimens and incorporating anti-jamming and anti-welding features not necessary in the FEM design.

The design chosen is basically quite simple, an advantage when working in the difficult environments of underground tests. The gage needs no external power source and provides a relatively large signal (0.5v to 20v), needing no further amplification for remote recording. The gage system is physically small, relatively rugged, and needs no adjustments in the field beyond alignment with the direction of radiation.

## TRI GAGE CONFIGURATION

The basic elements of the TRI gage Model SST-13 are depicted in Figure 12. X-radiation, entering from the right of the Figure, penetrates a free-moving beryllium disc (TAMPER). After crossing the GAP, the radiation is absorbed in a narrow layer of the high-Z SPECIMEN. Vaporization of a portion of this layer causes the specimen and the SUBSTRATE upon which it is mounted to recoil to the left, while the tamper is propelled to the right.

Movement of the substrate causes the COILFORM to pass between the MAGNET pole pieces, inducing an electromotive force (EMF) in the copper coils with which the coilform is wrapped. The EMF generated is proportional to the coilform velocity, $v(t)$, length of wire in the magnetic field, $l$, and the magnetic field strength, $B$, by the formula

$$EMF(t) = Blv(t) \quad . \tag{1}$$

Departures from this proportionality caused by finite-sized coils and the non-linearities of the real world will be discussed in a later Section.

### Gage Performance Parameters Considered

There are obviously a large number of parameters affecting gage performance and a successful design is always a series of tradeoffs and compromises. High electrical output, a desirable trait, necessitates a large number of coils (for a given magnet) but increases both electrical inductance and coil mass. Both increases tend to increase the rise-time of the gage, an undesirable trend. Reducing the coilform

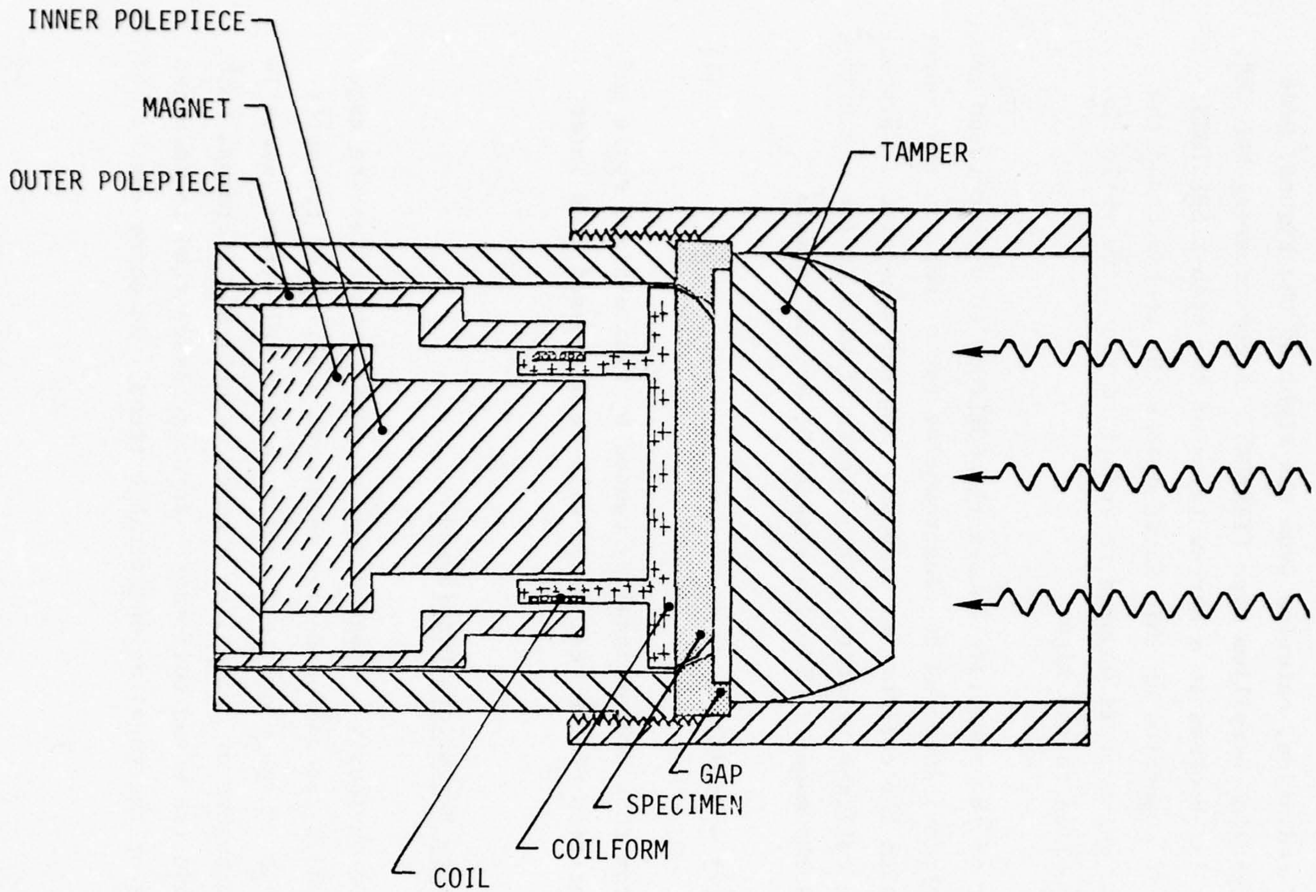


Figure 12. Basic elements of the time-resolved impulse (TRI) gage.

mass decreases the risetime but may introduce structural weaknesses leading to unwanted vibration. The design parameters listed below were each investigated theoretically and/or experimentally.

- Substrate dimensions and material
- Tamper dimensions and material
- Coilform dimensions and material
- Bonding of the specimen to the substrate
- Separate and one-piece coil forms and substrates
- Electrical and mechanical risetime
- Recording time
- Effect of gas leakage on substrate and tamper movement
- Effects of motion of gage on increasing the tamper/gage gap
- Welding of the gage or tamper by condensation of metallic gases
- Jamming of the gage or tamper by thermal expansion, shock wave motion, or cocking within either the gage housing or the magnet pole pieces
- Magnet dimensions and material
- Aperturing of the incident radiation
- Shielding of the gage electrical components from high energy direct and scattered radiation
- Shielding the gage electrical components from electrical noise
- Source of periodic vibrations affecting the gage output
- Calibration and data analysis

## Gaps, Gaps, and More Gaps

Since the TRI gage is a system with several components, and since between these components there exist gaps which affect various portions of the gage operation, it seems wise to attempt to head off confusion by locating and identifying each gap before proceeding with further discussion.

Referring to Figure 13, the following gaps are shown.

1. Tamper/specimen gap.

   Provides the gap into which initial expansion of gases occurs.

2. Tamper/housing gap.

   Provides clearance for movement of the tamper.

3. Specimen/guard ring gap.

   Allows for expansion of the specimen from both thermal expansion and shockwave motion.

4. Substrate/gap spacer gap (also referred to as primary seal).

   While initially quite small, this gap opens as the gage recoils and is an anti-jam, anti-weld feature.

5. Substrate/housing gap (also referred to as secondary seal).

   Provides clearance and guidance for movement of the specimen/substrate/coilform unit.

6. Coilform/magnet gap.

   Provides clearance between the moving coilform and the stationary magnet pole pieces.

7. Magnet/polepiece gap.

   Provides the appropriate magnetic impedance.

## MOTION OF THE GAGE AND TAMPER

After deposition, the gage and tamper separate at a rate dependent on the average pressure acting on their surfaces. Knowing the areal mass of

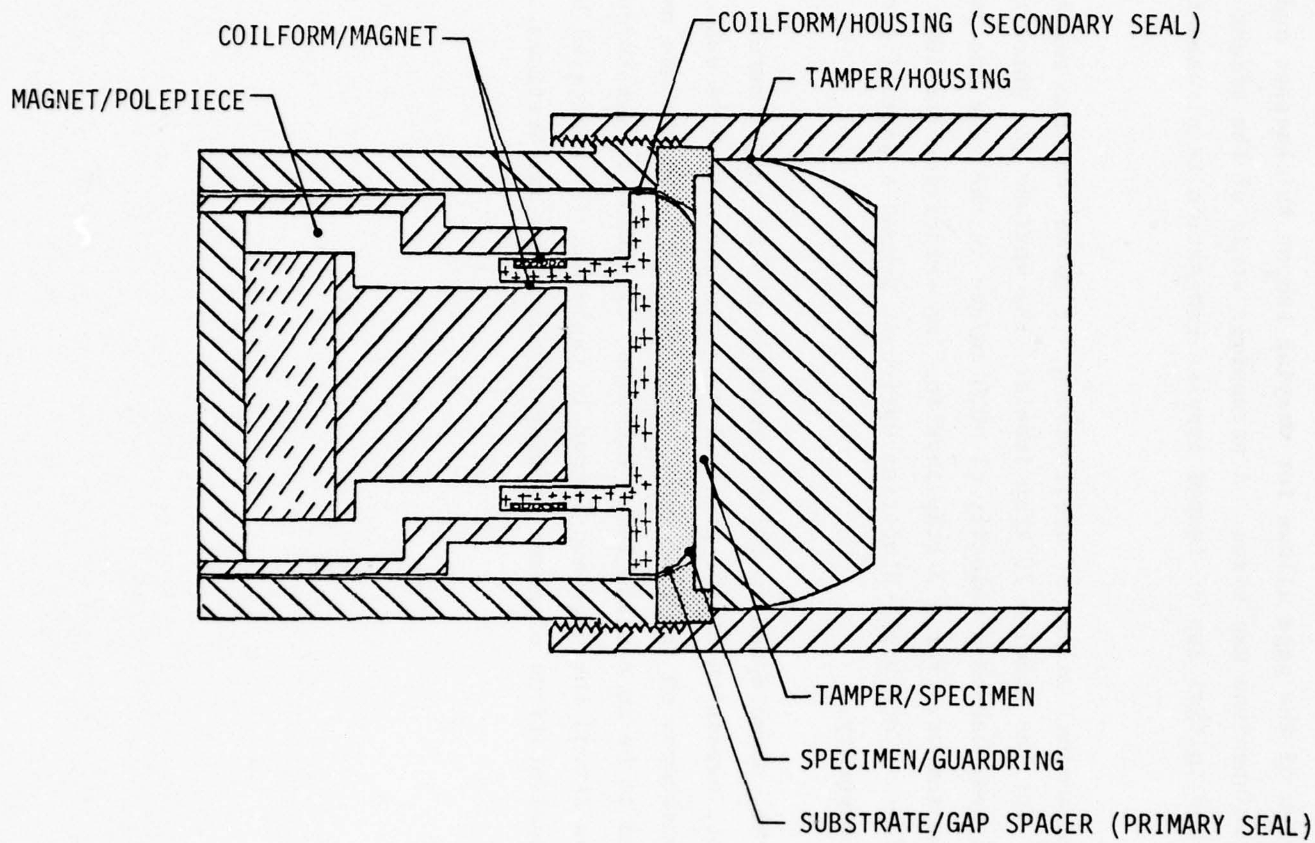


Figure 13. Gaps, gaps, and more gaps. The angle of the specimen/guard ring gap is exaggerated for visualization.

the tamper and gage, and measuring the gage motion, the average pressure in the tamper/specimen gap can be computed.

The design of the gage allows for varying tamper thicknesses and initial tamper/specimen gap sizes. A parametric study of the effect of tamper mass and initial gap on tamped impulse generation is planned for the UGT.

With the nominal values of areal masses, (2 $gm/cm^2$ for the tamper and 5 $gm/cm^2$ for the gage) a 20 ktap impulse, the maximum for which the gage is designed, causes a velocity of 4000 cm/sec in the gage and 10,000 cm/sec in the tamper. For a 5 ktap impulse, the velocities are 1000 cm/sec and 2500 cm/sec. Such high velocities obviously demand a gage of good structural integrity.

Since the sound speed in the hot metallic gas is approximately 60,000 cm/sec, expansion of the gas following surface motion is essentially instantaneous on the time scale considered here and the gas may be considered to be in equilibrium. Likewise, expansion of gas through interior gaps around the gage and tamper is rapid and is controlled by the usual considerations of gases flowing through gaps and orifices.

## SUBSTRATE AND SPECIMEN MATERIALS

The substrate material was chosen to be

1. Non-magnetic to avoid magnetic field distortion,

2. Of high modulus to decrease vibrations,

3. Dimensionally stable, and

4. Able to be bonded to the specimen material.

Stainless steel was chosen over aluminum or graphite for the final design although testing was performed with each material.

The tantalum specimen material was applied directly to the surface of the substrate by the ERDA Y-12 facility. Tests made by Y-12 of the bonding strength between the dense material and numerous types of substrates indicated the strength of the bond to be in the range of 0.1 to 0.15 kbar, dependent on the substrate material and the preparation of the surface.[2] Hydrocode calculations predicted compressive and tensile stresses at the substrate/specimen interface to be well under 0.1 kbar, although the calculated peak stress at the irradiated surface of the specimen was in the range of hundreds of kilobars. Therefore the bond is predicted to survive the underground test.

It is quite important that the specimen remain attached to the substrate during the recording period. The mass of the specimen represents a sizable portion of the mass of the gage. If the specimen becomes completely separated from the gage, the recorded gage velocity for the lightened gage mass is not representative of the impulse at the specimen surface.

High explosive tests (described in Section VI) producing 15-20 ktaps with relatively long duration, succeeded in separating the bond of a test specimen. Apparently, the higher peak pressure from the H.E. and a suspected lower bond strength on the specimen test were decisive contributors to the failure. Both scheduling and financial restraints prevented measurements at the field stress amplitude and duration to confirm favorable predictions.

### Gap Spacer Material

An annular ring of the specimen material is bonded with epoxy to the graphite gap spacer in a "guard ring" configuration. ATJ graphite was chosen for the gap spacer because the high melting point and low thermal conductivity of graphite reduce the rate of condensation of hot metallic vapors on the graphite surface and thus reduce the chance of welding the substrate to the gap spacer.

## CONFIGURATION OF THE SUBSTRATE, SPECIMEN, AND GAP SPACER

In order to obviate the need for precision apertures and to minimize the effects of finite dimensions on the quasi-one-dimensional experiment, the guard ring design shown in Figure 12 was chosen. With this design, a surface area larger than the gage area is exposed to radiation and "shadows" caused by imprecise alignment of an external aperture will fall on the guard ring area rather than on the gage itself. In addition, placing the walls at a distance from the recording portion of the gage reduces the effect of the walls on the measurement and more closely simulates a one-dimensional experiment.

The truncated cone shape of the substrate allows the substrate/gap spacer gap to enlarge as the gage recoils, preventing jamming. Also, the shape prevents radiation from passing through the gap and being deposited in the coilform/magnet area to the rear.

The bi-angle cone shape in the region of the specimen surface allows expansion of the specimen from both thermal and shockwave action without jamming. The dimensions of the gap were determined by calculating the thermal expansion of the specimen diameter at temperatures up to melt. (It was assumed that liquid and vaporized material above melt temperature would not contribute to the jamming process.) Superimposed on the thermal expansion is the temporary expansion due to the passage of the shockwave created by constant volume heating. The combined values of these two effects was calculated to be >0.6 mm. The specimen/gap spacer gap shown in Figure 5 is $\sim$0.5 mm, a somewhat less than conservative value that is a compromise with other considerations such as preventing the incident radiation from penetrating to the substrate material and the restraint on the expanding material provided by the unheated specimen and substrate materials.

## EFFECTS OF GAS LEAKAGE PAST THE SPECIMEN/SUBSTRATE

The anti-jam, anti-weld seal between the substrate and gap spacer necessarily allows some gas leakage as the gage recoils and the gap opens. This Sub-Section describes the effect of leakage on gage design and discusses the probable errors in calculation of the time-resolved impulse from this source.

Figure 14 shows the gage and tamper in their initial positions and in their positions at time t after displacement by the pressure profile shown in Figure 3. In Figure 14b the specimen has attained a velocity derived from both the prompt, short duration impulse and the much longer

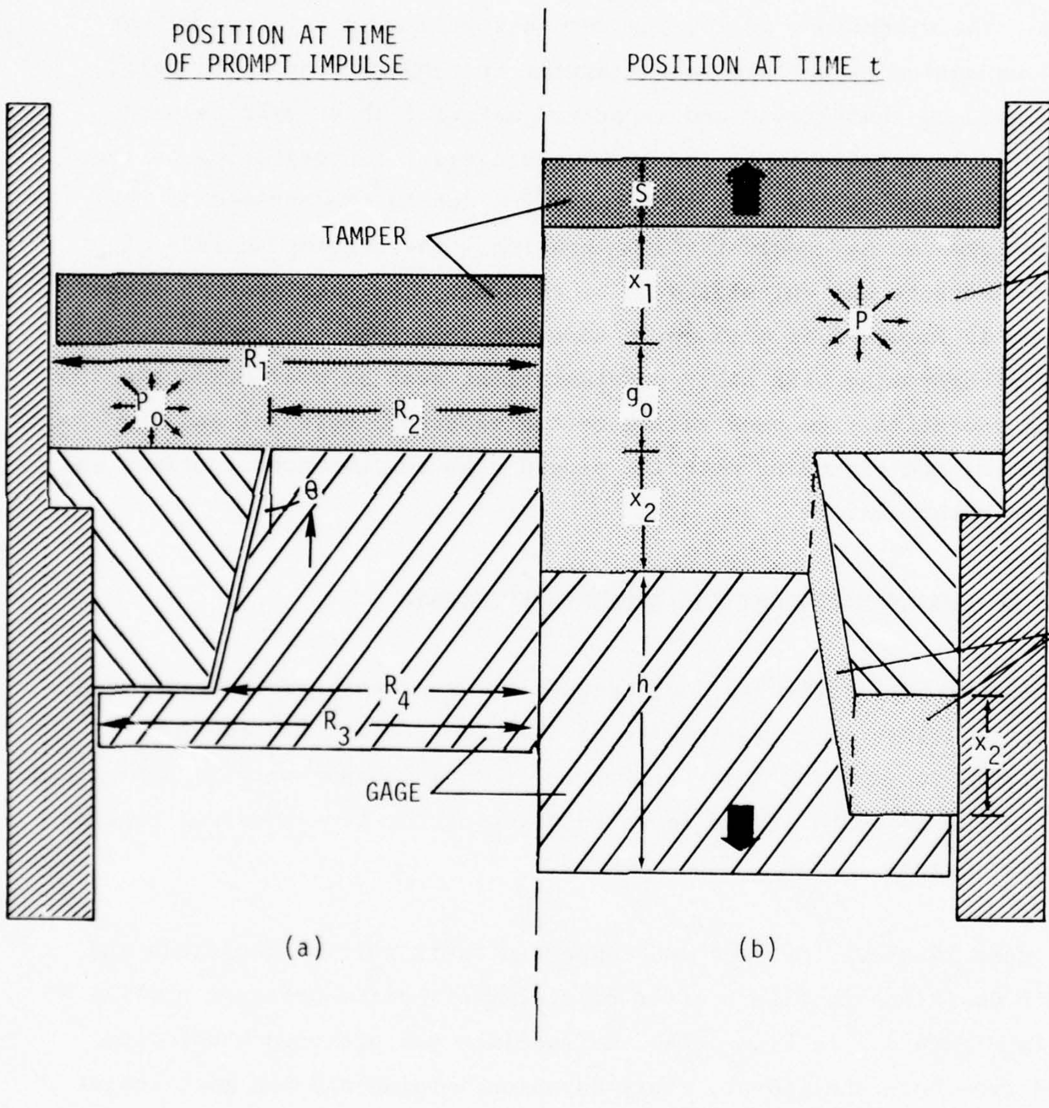


Figure 14. Gage positions at times of prompt impulse (a) and later (tamped) impulse, (b) showing gage and tamper motion and leakage of gas around gage.

tamped impulse arising from the confined gases. Two volumes are defined in the Figure. The "gap volume" consists of the volume in the initial gap, $g_o A_1$, plus the volume opened by the recession of the tamper, $A_1 x_1$, and the specimen, $A_2 x_2$. Thus

$$V_g = A_1(x_1 + g_o) + A_2 x_2 \quad . \tag{2}$$

The "leakage volume" consists of the volume within the tapered seal plus the volume of the secondary seal

$$V_L = (A_3 - A_2)\, x_2 \quad . \tag{3}$$

In order to calculate the pressure-time history of the confined gases from the measured velocity-time history of the specimen, we must make assumptions as to the pressure distribution over the various areas of the specimen upon which the gases act. Since gage motion during the prompt portion of impulse generation is on the order of only one micrometer, we can assume that the prompt pressure is applied only to the area $A_2 = \pi R_2^2$ . As the specimen recoils, however, the area increases to $A_3 = \pi R_3^2$ as gases flow past the tapered seal and act upon the secondary seal.

Two competing effects will affect the specimen motion.

1. The pressure in the original gap will be lowered as the volume available for gas expansion, $V_g + V_L$, is increased over that of the original gap volume only. The trend will be to lower the resultant specimen velocity.

2. The area over which this pressure acts will be increased over that of the initial area. The trend will be to increase the specimen velocity.

The TRI gage has been designed to minimize these effects, principally by minimizing the differences between the two areas. Note that the leakage volume, $V_L$, and the area difference, $(A_3-A_2)$, approach zero as area $A_2$ approaches $A_3$, i.e., $(R_2 \rightarrow R_3)$.

Since the leakage gases must flow through restricted passages, especially during the early stages of specimen motion, the pressure within the leakage volume will be less than that within the gap volume. Analyses made considering that the gap and leakage volume pressures have equilibrated represent a maximum (i.e., conservative) estimate of the change. Thus, a 15% area ratio is the maximum positive increment of velocity arising from area considerations with the present gage design.

For a nominal gage configuration and a nominal impulse of 5 ktaps, the negative increment of velocity due to increased gas volume is $< 1\%$ after 50 μsec. The combined effect on the total impulse of increased volume and increased area is therefore $\sim 15\%$

A more precise calculation of uncertainties from leakage requires the solution of the time-dependent motions of the specimens and tamper, including the area considerations above and the time-dependent gas flow into the leakage volume. Calculations for the UGT test results will be made, using an iterative procedure, to determine the velocity and time-dependent correction factor for each record. Three calculations will be made, assuming:

1. No gas leakage,
2. Leakage with equilibrated pressure in the leakage volume, and
3. Leakage with gas flow restricted by passage through the narrow tapered seal.

Assumption 3 is considered the best estimate of expected gage performance vs. ideal performance and is expected to reduce the uncertainties to 5-10%.

## WELDING CONSIDERATIONS

The flow of hot, dense gases and liquids past the various seals within the gage, leading to possible condensation of metal on the seal walls, is obviously a complex matter, where a few well-chosen experiments can replace a considerable amount of theory and conjecture. Such was our approach in testing the ability of the gage to perform without the welding of moving parts to stationary parts.

A series of electron-beam tests, described in Section VIII, generated an amount of metallic liquid and gas roughly approximating those predicted for the underground test. Post-test, this molten and vaporized material was found solidified on the gage interior surfaces and bridging and filling stationary gaps comparable to the size of the gaps around the moving parts.

No bridging or welding was observed, however, between the moving gage and its stationary neighbors, indicating that the motion of the gage causes bridges either never to form or to form and break without impeding gage motion.

## DESIGN OF THE TAMPER

Beryllium was chosen as the tamper material since it is relatively transparent to the incident radiation. The diameter of the tamper was based on considerations of minimizing the tamper/housing gap in order to minimize the escape of metallic vapor while still providing for tamper motion without binding.

Thermal expansion from energy deposition is less than 1μ, a negligible amount. Thermal wave propagation also increases the expansion only minimally. Expansion from heating of the inner surface of the tamper by hot metallic gases was not considered to be a problem.

After numerous trial designs, the truncated sphere shown in Figure 15 was chosen for the tamper. The distinct possibility of jamming by a cylindrical tamper moving through the tamper housing tube was the overriding consideration. Although superior gas sealing and constant tamper thickness (and thus uniform deposition on the specimen surface) are afforded by the cylindrical design, jamming of the tamper during a test would severly decrease the confidence in the test results.

The present truncated hemisphere is unlikely to jam since it can rotate freely down the housing extension if an asymmetric load is applied which causes tilting. To further decrease the chances of jamming or welding, the tamper is lined on its exterior with grafoil, a pressed graphite formed into sheets. The grafoil provides both a tight, low friction seal and a surface upon which hot gases are unlikely to condense and to cause welding or to reduce impulse.

MAGNET DESIGN

The configuration of the magnet and coils provides a reasonably linear ( ∿5% over the total coilform travel), reasonably high electrical output (5.5 mv/cm/sec), easily calibrateable electromagnetic system. Nonlinearities in the system can be reduced during data analysis to less than 2%.

A cobalt-samarium magnet with high magnetic density (∿5 times greater than Alnico V) is placed within the pole pieces as shown in Figure 16.

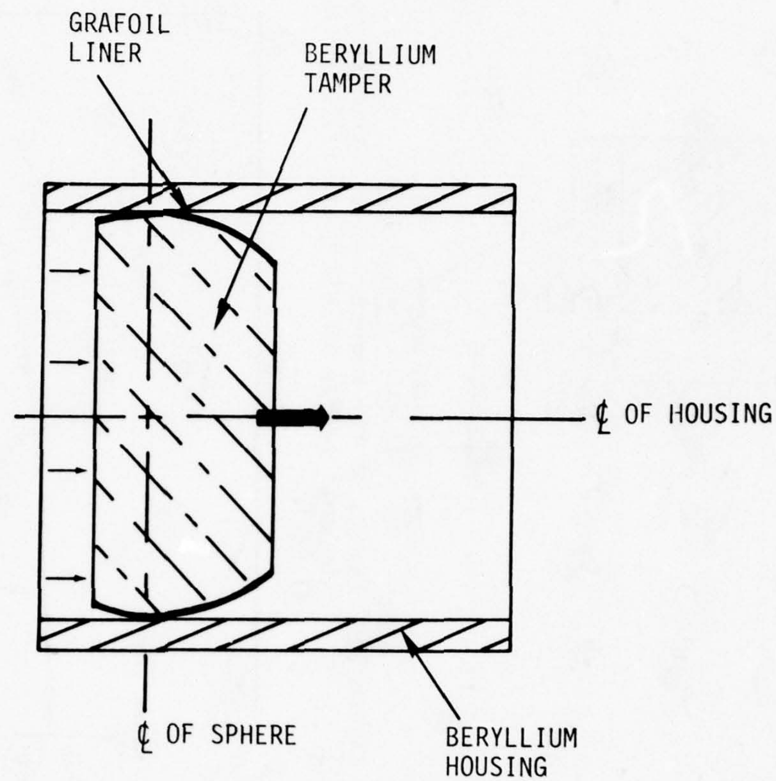


Figure 15. Design of tamper. The grafoil liner prevents welding from condensation of hot metallic gases. The truncated sphere shape prevents binding.

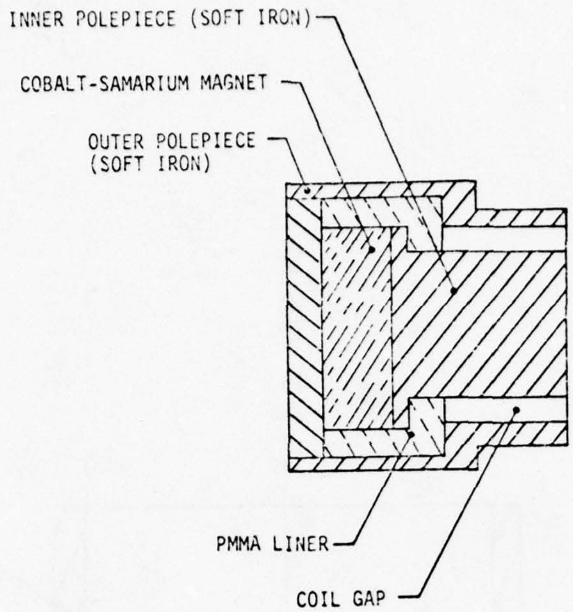


Figure 16. Design of the magnet. Field strength in the coil gap is ~0.177 tesla (1770 gauss).

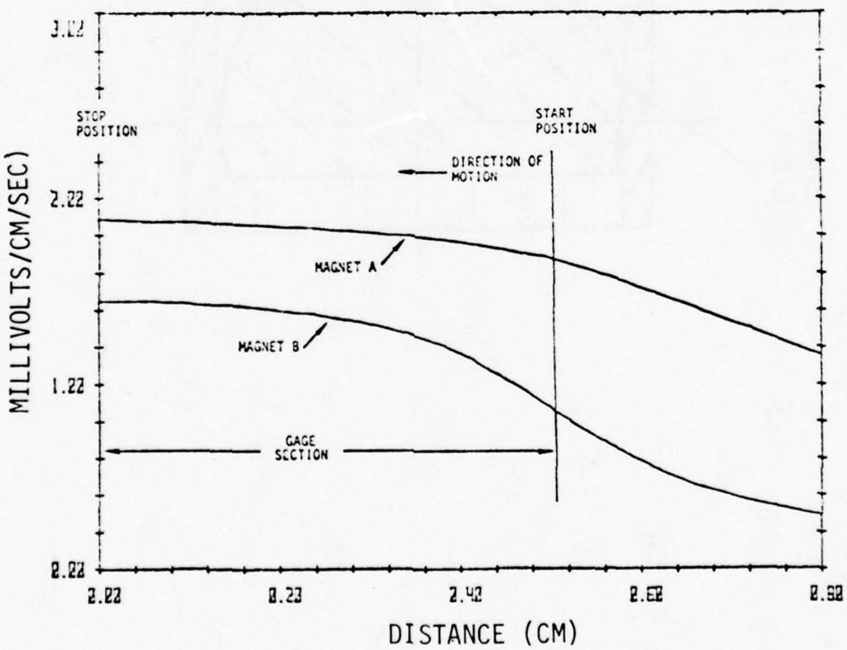


Figure 17. Gage output vs. stroke position for two magnets. Magnet A is an early version of the field design (field gage sensitivity is 7.0 mvolts/cm/sec).

A PMMA liner keeps the magnet and center pole piece centered within the outer pole piece. Pole pieces are made of soft iron. Average field strength, inferred by measurements of coilform velocity and electrical output is 0.177 tesla (1770 gauss).

Although it would have been advantageous from a reduced risetime and vibration standpoint to shorten the coilform length, a design tested in which the initial position of the coils was outside the gap between the inner and outer pole pieces, showed greatly increased non-linearity during the initial portion of the coilform travel.

Magnets and coilforms are calibrated by measuring the electrical output while dropping the coilform into the magnetic field. A precision fixture is used to align the coilform with the magnet polepieces, and a fiber optics positioning system provides measurements of coilform velocity and position as functions of the coil output. The output from such a calibration is shown in Figure 17, labeled "Magnet A." The magnet configuration is similar to the magnet used for the field version of the TRI gage, although lower in sensitivity.

The calibration curve is measured over a much longer stroke than that used by the gage itself. Only the portion of the curve marked "gage section" is used during gage operation. An alternate design, a one-piece magnet with the initial position of the coilform external to the pole pieces, gave the very non-linear output vs. position curve shown as "Magnet B" in the Figure.

While sensitivity differences of $\sim$10% are measured between different magnets, differences in coilforms are less than 2%. Because of the only minor differences in coilforms and because of the possibility of breaking the coilform wires by excessive bending during calibration, only the magnets are individually calibrated before an underground test.

## SOURCES OF VIBRATIONS IN THE GAGE ASSEMBLY

Beginning with the earliest tests and extending throughout the program, vibrations in the gage assembly (exhibited by periodic oscillations in the gage output) were a major problem. The minimizing of these vibrations became a major effort as the other problems of gage design were solved and the vibrations continued.

The very nature of the assembly, a disc fastened to a thin-walled cylinder and impulsively loaded on one surface, is ideal for exciting numerous modes of vibration. Because the dimensions of the disc and cylinder are comparable, the period of their vibrations are not too dissimilar and isolating the source of a given vibration proved quite difficult.

The output of a mechanical impact test of an aluminum specimen attached to a polymer coilform is shown in Figure 18. In Figure 19 is the spectral analysis of the output, calculated by the Fast Fourier Transform (FFT) technique discussed in the Data Analysis section. Large amplitude vibrations at 36 kHz and 72 kHz were measured, with smaller amplitude harmonics seen at 116 kHz and 153 kHz.

The frequency of the fundamental mode of vibration of a solid disc is given by

$$f = \frac{\lambda}{2\pi a^2} \left[ \frac{\dfrac{Eh^3}{12(1-\nu^2)}}{\dfrac{h\rho}{g}} \right]^{1/2}$$

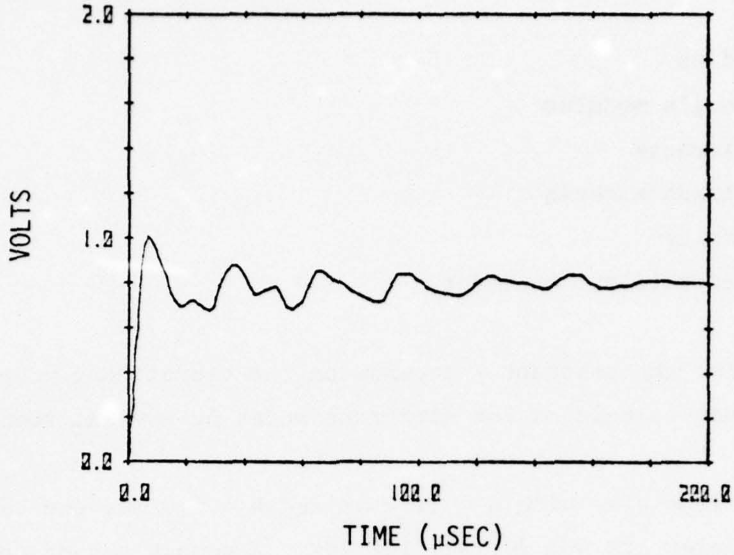


Figure 18. Output from polymer coilform and aluminum specimen.

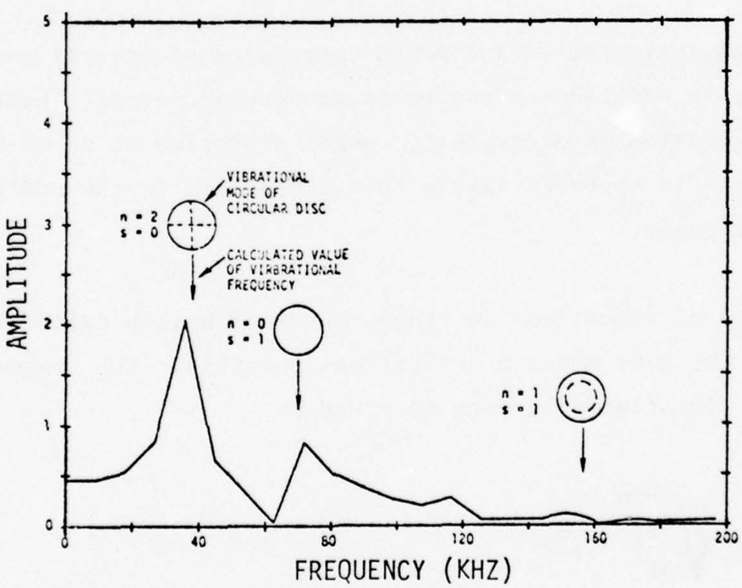


Figure 19. Spectral analysis of Fig. 18 output showing correlation of measured vibrational frequencies with different plate vibration modes.

where $a$ = radius

$E$ = Young's modulus

$h$ = thickness

$\nu$ = Poisson's ratio

$\rho$ = density

$g$ = gravitational constant.

The value used for the constant $\lambda$ depends on the vibrational mode excited and has been calculated for different modes by several researchers.[3]

For an aluminum disc with $a \approx 11.4$ mm and $h = 5.0$ mm, the calculated resonant frequencies are 40, 70, and 157 kHz. A comparison of the calculated and measured frequencies is shown in Figure 19. The agreement indicated by the comparison suggests that vibration of the specimen is an important source of oscillation in the gage output.

Other tests, using solid and porous specimens of several materials, indicated that, in addition to the resonant frequencies of a particular specimen configuration, a persistent, common vibration at 50-60 kHz was usually present. It appeared likely that vibrations in the coilform itself were the cause.

Calculation of vibrations in rings, bars and hollow cylinders is complicated by the many modes of vibrations possible. The frequency of pure radial vibration of a ring is given by

$$f = \frac{1}{2\pi}\sqrt{\frac{Eg}{\rho r^2}} = \frac{C_L}{2\pi r} \qquad (4)$$

where r is the radius and $C_L$ is the longitudinal sound speed. For the polymer coilform considered here,

$$f = 52 \text{ kHz} \qquad \text{(radial vibration)}$$

Torsional vibration, in which the centerline of the ring remains undeformed and all cross sections of the ring rotate through the same angle is given by

$$f = \frac{C_L}{2\pi r} \sqrt{1 + i^2} \tag{5}$$

where i denotes the number of wavelengths to the circumference. For the coilform tested

$$f = 74,\ 118, \ldots \text{ kHz .} \qquad \text{(torsional vibration)}$$

For flexural vibration, in which the circular cross section of the ring becomes oval and which may involve some twist (rotation), the vibrational frequency is given by

$$f_i = \frac{1}{2\pi} \frac{C_L}{r^2} \sqrt{\frac{i^2\left(1-i^2\right)^2}{2\pi\left(1+i^2\right)}} \tag{6}$$

where i = 1 denotes whole body translation and i = 2 represents the lowest vibrational frequency mode. For the coilform tested

$$f = 19 \text{ kHz} \qquad \text{(flexural vibration)}$$

The complicated picture described above was made even more complicated by the fact that the coilform is wrapped with the copper wire which provides the electromagnetic pickup. The wire, which possesses different acoustic and mechanical properties than the polymer, makes the problem intractable for simple analysis.

A 2-D finite-difference hydrocode (HEMP) calculation was made by LLL* in which the polymer and copper components were entered in a manner consistent with their placement in the actual coilform. The frequency of the fundamental mode of vibration affecting the pickup coils was

$$f \simeq 65 \text{ kHz} \qquad \text{(HEMP calculation)}$$

From the computer output, it appeared that this vibration combines features of flexural and radial motion, with the free end of the cylinder traveling both axially and radially. This calculation, along with other analytical expressions for vibrational frequency, gave guidance in the effort to identify the sources of the vibrations.

## TESTS TO ISOLATE THE SOURCE OF VIBRATIONS

Two test series were performed to attempt to isolate and to minimize the vibrations in the gage assembly. The effects of the vibrations of the specimen itself having been determined from the mechanical impact series described previously, the first of the isolation series concentrated on the mechanical impact of a coilform without a specimen. Representative outputs and corresponding spectral analyses are shown in Figure 20.

The two tests were made with slightly different initial inputs, with the input to Test 63.02 having a less steep and therefore fewer high frequency components than that of Test 63.04. Oscillations at 55-60 kHz were observed in these tests and in other test conducted under similar conditions.

*Calculations furnished by D.W. Hanner of Lawrence Livermore Laboratory.

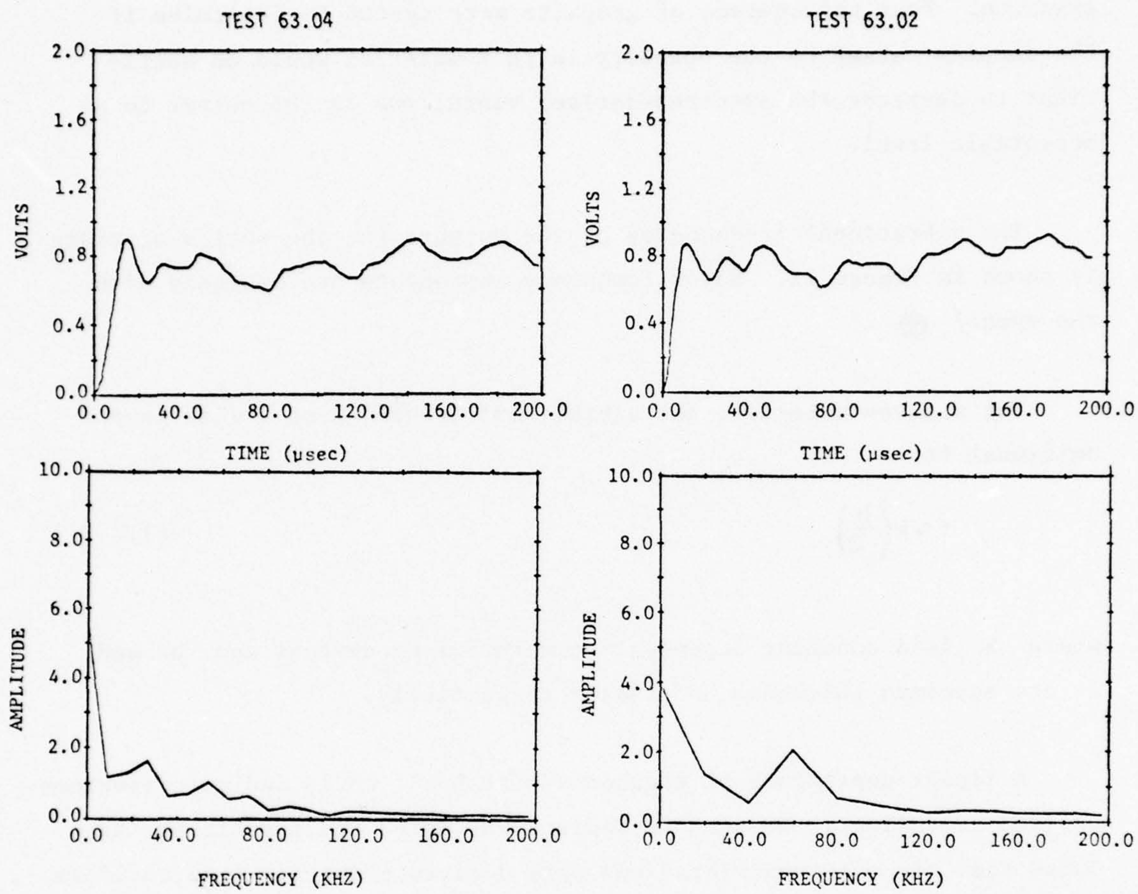


Figure 20. Outputs from bar impact tests on coilform alone. The resonant peak at $\sim$58 kHz is common to all tests using polymer coilforms.

A second test series was conducted using the short duration, low amplitude pulse from an Nd:Glass laser irradiating samples of ATJ-S graphite. Four thicknesses of graphite were tested to determine if the damping caused by the porosity in this material would be sufficient to decrease the specimen-derived vibrations in the output to an acceptable level.

The vibrational frequencies of the outputs for the series of tests is shown in Figure 21. Major frequency components are designed with the symbol $\oplus$ .

For a given material, the vibrational frequency of a disc is proportional to

$$f \sim k\left(\frac{h}{a^2}\right) \tag{7}$$

where k is a constant dependent on material parameters and h and a are specimen thickness and radius respectively.

A linear dependence of frequency with $h/a^2$ would indicate specimen-derived vibrations. No such dependency was noted and thus it was deduced that the observed vibrations were derived primarily from coilform resonances.

Resonances at $\sim$55 kHz were noted in each test, corresponding to the coilform resonances observed in the first isolation test series. As described more fully in the subsection on coilform design, additional experiments on polymer coilforms in which the coilform walls were thickened, thinned, braced, damped, etc., did little to change the amplitude and the frequency of the oscillations. As noted in the subsection, the solution to the problem was provided by changing to electromechanical damping afforded by a metallic coilform, and, in particular, by a substrate and coilform made of one piece rather than two.

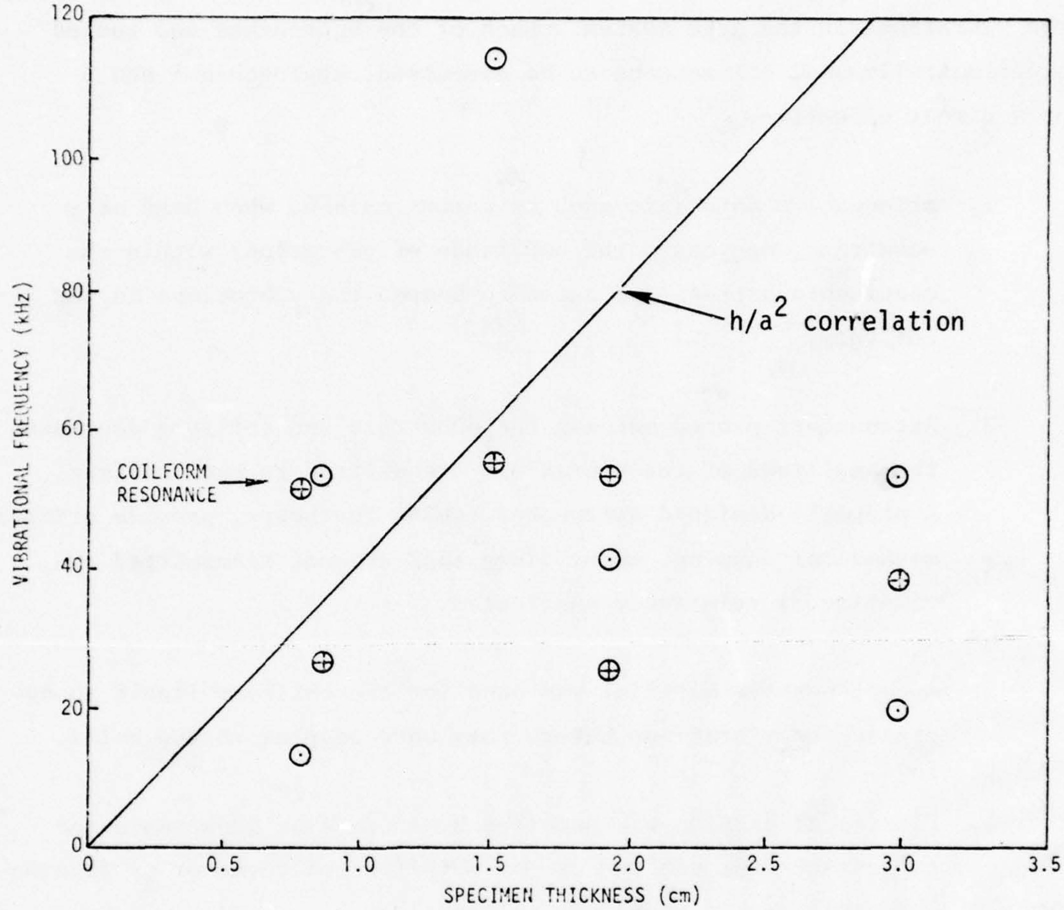


Figure 21. Laser deposition tests on graphite specimens with polymer coilforms. Correlation of resonances with the $h/a^2$ line would indicate specimen-derived vibrations. No such correlation was noted.

## MINIMIZING THE EFFECTS OF VIBRATIONS

Several approaches were explored to decrease the amplitude of the vibrations in the gage system. Each of the approaches was tested experimentally and, for reasons to be discussed, approaches 4 and 5 proved most effective.

1. Attenuative materials such as porous carbon, when used as a substrate, decreased the amplitude of vibrations within the specimen/substrate and acted to dampen the vibrations in the coilform.

2. Attenuators placed between the substrate and coilform decreased the amplitude of the vibrations transmitted to the coilform. A properly-designed attenuator could, in theory, provide critical mechanical damping, where vibrations are not transmitted and risetime is relatively unaffected.

3. An attenuative material was used for the coilform itself to decrease the vibrations before they were coupled to the coils.

4. Electrical damping was provided by increasing inductance and capacitance through the use of metallic coilforms or by placing conducting tape around the coil area.

5. Metallic coilforms also provided greater rigidity to decrease vibration amplitude.

DESIGN OF THE COILFORM

Numerous coilform designs were tested, based mainly on the configuration shown in Figure 12. Permutations of the design were based around:

1. Coilforms that were separate from the substrate and were attached by various means to the rear of the substrate,
2. Coilforms made of metallic or of polymeric materials, and
3. Coilforms that were one-piece extensions of the metallic substrate.

The goals of the coilform testing program were:

1. To minimize gage risetime,
2. To decrease noise in the gage output caused by vibrations in the coilform and substrate, and
3. To contain the coils and electrical leads in a sufficiently rigid manner such that shorting and breaking of wires would not occur.

The development progressed in approximately the following sequence.

1. Polymeric coilforms.
2. Polymeric coilforms with mechanical vibration-damping materials between the substrate and coilform.
3. Polymeric coilforms wrapped with conducting metal foil to provide electrical damping.
4. Electrically conducting coilforms made of a special, slightly porous magnesium alloy which has been used to provide mechanical damping in movie camera casings, vibration table mounts, satellite component mounts, etc.

5. The same conducting coilforms with a slot to reduce the electrical damping by eliminating the "shorted turn" configuration.
6. An integral coilform/substrate design made of stainless steel to provide greater rigidity and to eliminate problems which had arisen of bonding the coilform to the substrate in a reproducible manner.

Polymeric Coilforms

Lightweight polymeric* coilforms were fabricated and tested by mechanical impact and in the electron beam environment. While the risetime of the design was apparently quite acceptable ($\leq$10 μsec), severe vibrations occurred, such as shown previously in Figure 18.

The main characteristics of the output of the polymeric coilforms were a risetime of $\sim$10 μsec leading to a peak which overshot the average level of the succeeding vibrations by approximately 25% and then, after $\sim$20 μsec, settled down to a series of sinusoidal, exponentially damped vibrations persisting for 100-300 μsec.

The calculations discussed previously, using a 2-D finite difference code to simulate an impulsively-loaded cylinder wrapped with wire, indicated that reasonable changes in the material dimensions were not likely to lead to substantial changes in the period or amplitude of the vibrations. This was found to be the case, when a series of tests with the coilform wall thickness doubled showed only minor improvement.

*Glass epoxy, G-10, produced by General Electric Company.

## Polymeric Coilforms With Attenuators

Various types and thicknesses of attenuators were placed between the coilform and substrate to (1) provide mechanical damping of the vibrations transmitted from the substrate to the coilform and (2) to provide a vibration-absorbant material to damp out vibrations within the coilform itself.

Layers of neoprene, of latex, and of masking tape were used in the study. The damping materials were quite effective both in acceptably decreasing the amplitude of the oscillations and in unacceptably increasing the gage risetime.

A comparison of the outputs of polymeric coilforms screwed to aluminum substrates with 0.33 mm (.013") latex and with 0.79 mm (.031") neoprene attenuators at the interface is shown in Figure 22. Both the long risetimes and the lack of steady conditions atop the pulse make these configurations unacceptable.

Gage outputs with various layers of 0.1 mm thick tape are shown in Figure 23. While the risetimes of the thinner layers of attenuators is acceptable, the combination of risetime and noise to signal ratio (N/S) only minimally meets the desired specifications, shown in Figure 24 as the shaded area between risetime = 15 μsec and N/S = 10%. No additional effort was expended in the attenuator series.

## Polymeric Coilforms With Conducting Foil

Layers of copper wrapped around the coil area were also effective in decreasing the amplitude of the oscillations of the electrical output. Unfortunately (and as expected), the increase in inductance afforded by

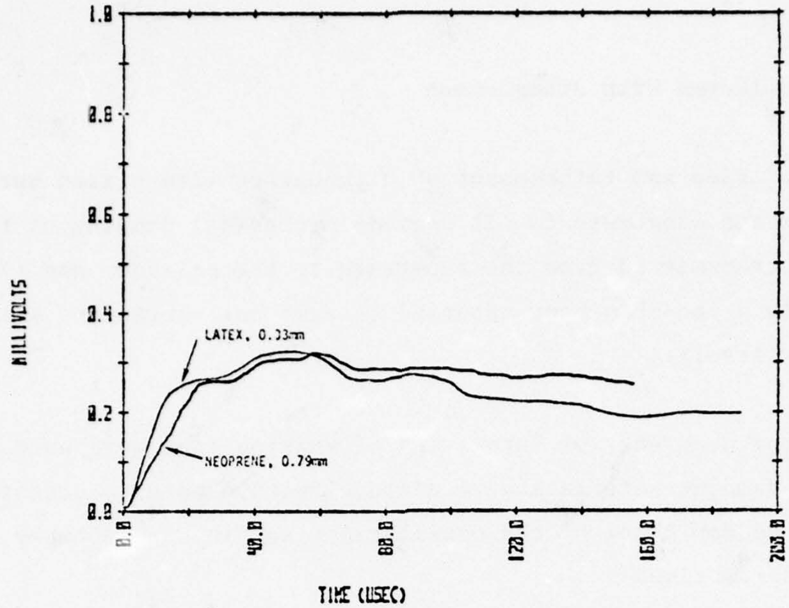


Figure 22. Neoprene and latex attenuators placed between the specimen and coilform produced unacceptable waveforms.

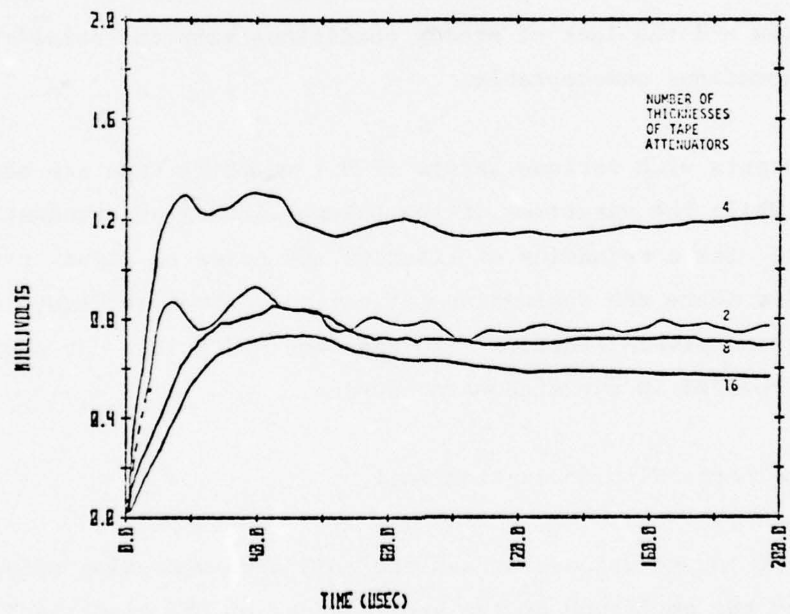


Figure 23. Tape attenuators decreased the amplitude of the oscillations but increased the risetime unacceptably.

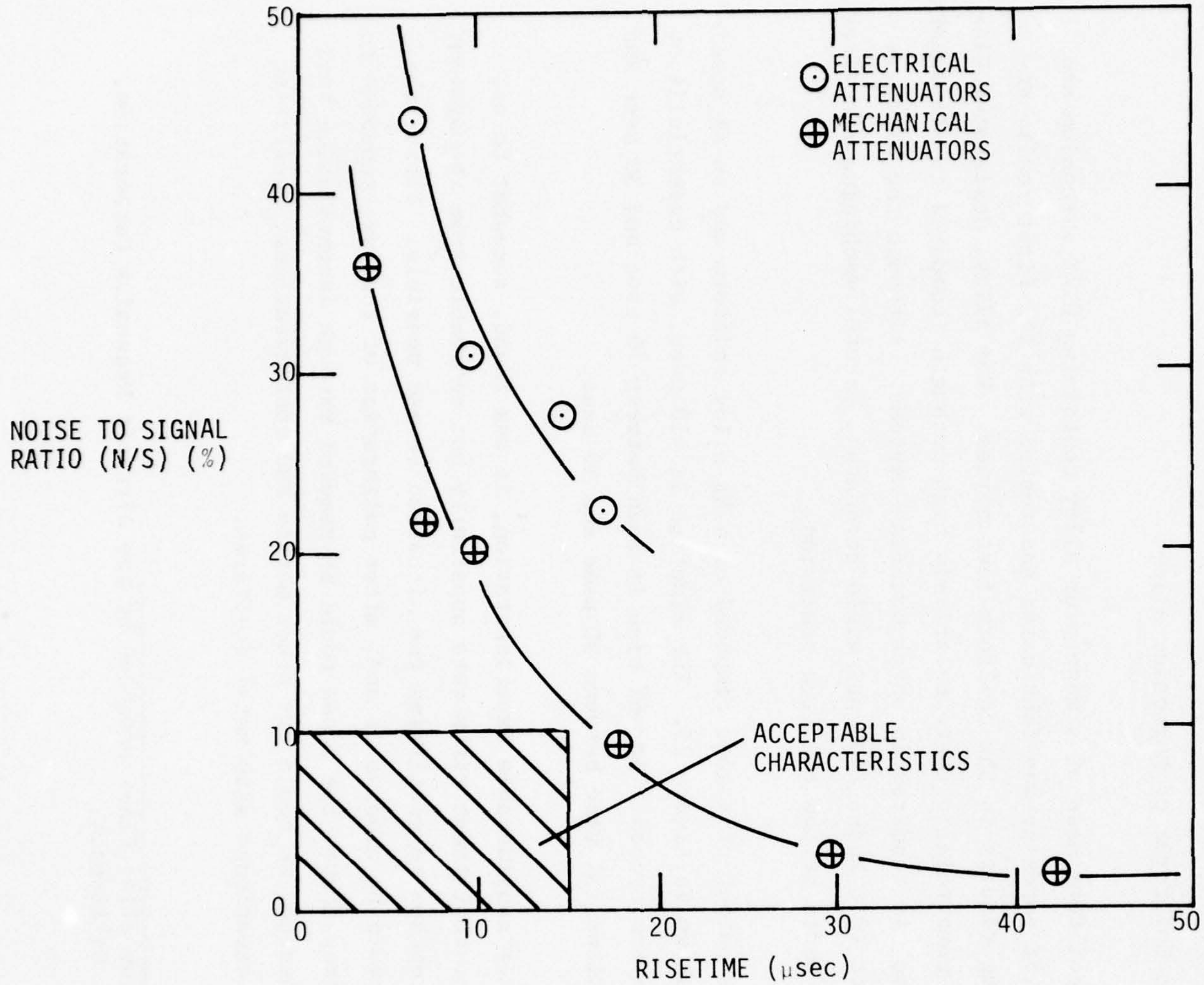


Figure 24. Mechanical and electrical attenuators were used to decrease the noise to signal ratio, but the risetimes were not compatible with the necessary gage characteristics.

the copper sheath also produced increased risetime in the gage. Various thicknesses of foil, inside and outside of the coilform, and shorted (single turn) and unshorted were tested. Figure 24 also displays the results of this test series. No acceptable tradeoff between increased risetime and decreased oscillation amplitude was found.

### Metallic Coilforms of Magnesium Alloy

A coilform made of a magnesium alloy containing 0.7% zirconium and with ∿2.5% porosity was fabricated and tested with the first really encouraging results in the coilform test series. The alloy, designated F1A-F*, is used commercially where relatively high strength (compared to elastomers and foams) is required in shock mounting systems. Although the alloy is very soft (0.6 kbar, 8400 psi yield strength), careful machining practices yielded parts of the required precision.

The output of a gage composed of a Mg alloy coilform and an Al specimen is shown in Figure 25. The risetime is <10 μsec, with essentially no noise on the record. An ∿6% rise is seen between 10 μsec and 30 μsec and an additional 3% rise between 30 μsec and 50 μsec.

After considerable experimentation, it was found, somewhat to our surprise, that these rises were apparently not removable from the system. Two approaches to rectifying the situation seemed possible. First, the system could be used as is and, after calibration of the gage response to a true step input, the rises could be removed through deconvolution analysis. Second, we could try other metals and configurations, benefiting by this experience with metal coilforms.

*Magnesium alloy F1A-F produced by the Aircraft Magnesium Corporation, Gardena, California.

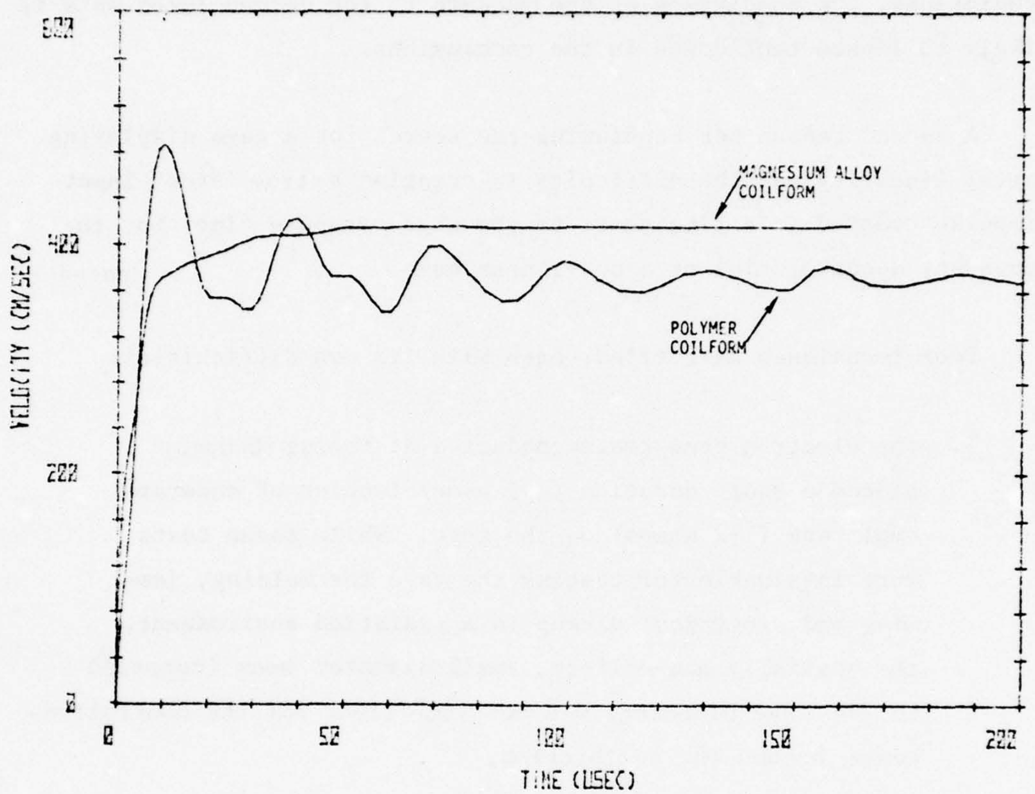


Figure 25. A magnesium alloy coilform provided a much smoother output than the polymer coilform but had a ∿10% rise over 50 μsec.

The second course of action was taken, for the following reasons. First, expected output from the tamping experiment looks very much like the undeconvoluted ("raw") record from the gage response shown in the Figure. If the impulse from the test is entirely prompt, contrary to predictions, the comparison of the raw data to the deconvoluted data is likely to lessen confidence in the conclusions.

A second reason for continuing the search for a gage displaying better linearity was the difficulty in creating a true "step" input (impulse created in a time short to the gage response time) for the necessary deconvolution of a non-linear gage.

Four techniques were tried, each with its own difficulties:

1. The electron beam tests conducted at Boeing Company placed a short duration ( <1 μsec) impulse of moderate amplitude (1-2 ktaps) on the gage. While these tests were invaluable for testing the gage for welding, jamming and electrical pickup in a radiation environment, the spatially non-uniform, small diameter beam (compared to the gage diameter) was not sufficient for the controlled tests needed for calibration.

2. The laser test series conducted at LLL provided a very short duration pulse (40 nsec) followed by a longer, lower amplitude pulse (300 nsec) arising from the plasma created by the breakdown of air at the irradiated surface. Although this pulse would have been quite satisfactory for gage calibration, the total impulse was <0.4 ktaps, insufficient for meaningful tests. A laser-initiated sheet explosive test, which promised to give sufficient planarity, duration, and impulse was found to be impractical when initiation of the H.E. proved impossible with the power level available with the laser.

3. High explosive, detonated in thin sheets on the surface of the gage, provides high impulse in reasonably short times. Conventional methods of detonating the H.E. without either unduly shocking the gage or introducing nonplanarity proved difficult, however. Light-initiated explosive sprayed onto the gage surface seemed a likely alternative, but was unavailable for this study.

4. Exploding foil-generated shock waves applied to the gage surface also appeared a likely method of creating short duration, high amplitude pulses. Initial tests showed the electrical pickup by the gage from the exploding foil bank to be greatly in excess of the signal from the gage movement and no additional testing was performed. It is likely, however, that the gage and leads can be electrically shielded in a manner sufficient to overcome this problem.

The third and deciding reason to press on with a different design was the desire to simplify the gage construction by making a one-piece, integrated substrate and coilform. The magnesium alloy was judged too soft for the integral construction design and stainless steel, which is much stronger and also non-magnetic, was substituted. This design, which resulted in the field version of the TRI gage is discussed next.

The Stainless Steel Coilform Field Gage

The one-piece "integral" substrate and coilform selected for the field version of the TRI gages is shown in Figure 26. This configuration of the gage displayed the most desirable combination of characteristics of any of the numerous configurations tested, although it is certain that additional testing would result in a more optimal design. In particular, this configuration exhibited:

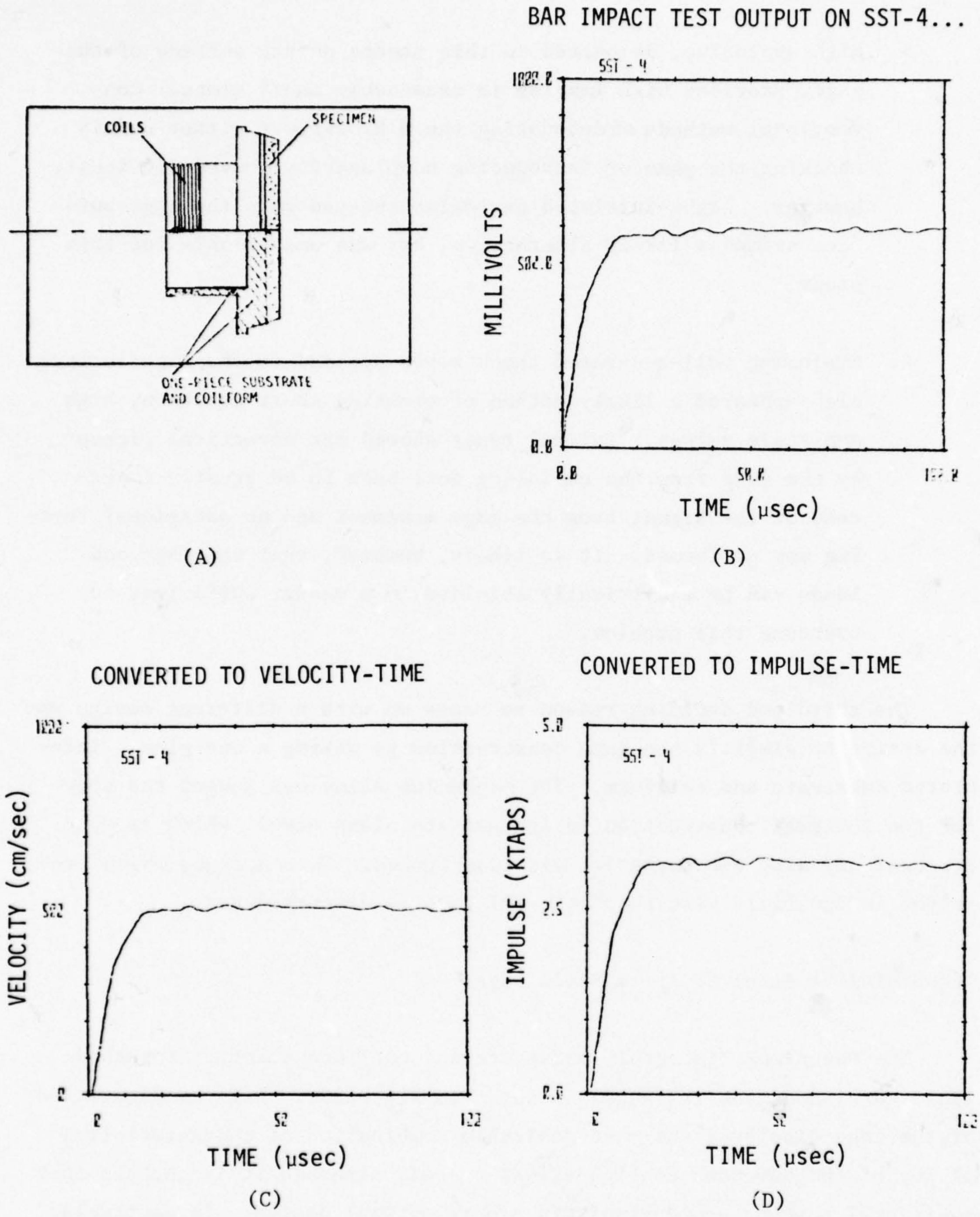


Figure 26. The one-piece, stainless steel coilform gave low noise and good risetime. The graphs show the raw data as well as the corresponding velocity-time and impulse-time data.

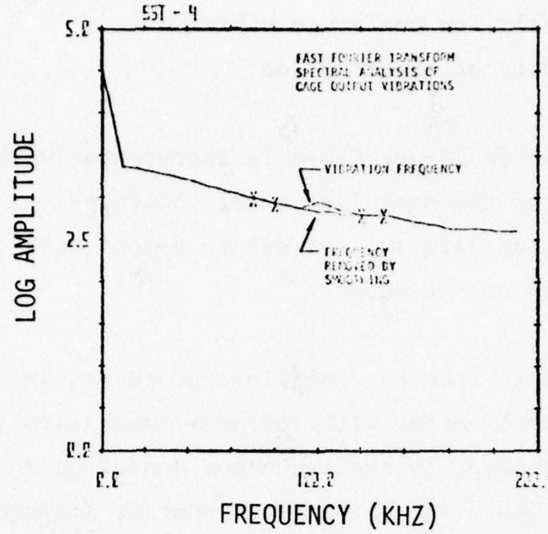


(E)

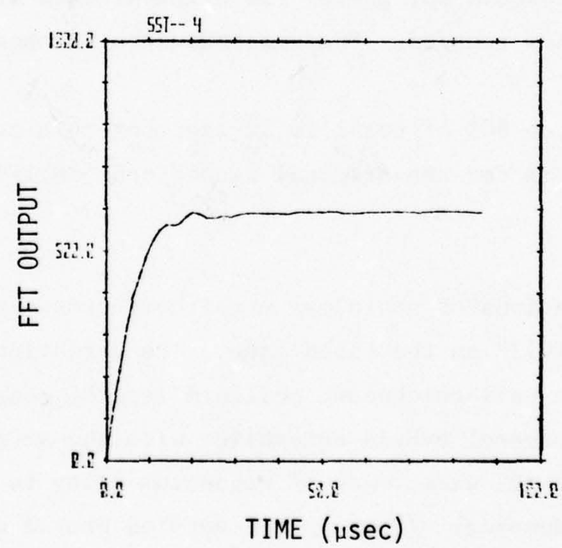


(F)

Figure 26 Continued. The remaining vibrations can be removed by the Fast Fourier Transform Technique described in the Data Analysis section.

- good linearity and risetime
- relatively low amplitude vibrations
- simplicity of construction

The record shown in Figure 26b-e is representative of the results of bar impact tests on the stainless steel coilforms. A complete set of raw and deconvoluted data is included to demonstrate the sequence of analyses performed on the data.

The digitized data from the oscilloscope record is converted to velocity-time and impulse-time with the non-linearities arising from the magnetic field removed by the technique described in the Data Analysis Section (Figure 26b-d). A Fast Fourier Transform technique (FFT) is used, if desired, to perform a spectral analysis on the artifacts on the gage output arising from gage ringing (Figure 26e). The peak at ∿100 kHz indicates the major ringing frequency in the record. This frequency range is fitted with a smooth curve between the x's and an inverse FFT is calculated, giving the original data with those frequency components now removed. The smoothed data is shown in Figure 26f.

Gage risetime to 90% of total is 12 μsec for this test. Noise to signal ratio is ∿20:1 for the original record and ∿30:1 for the smoothed record.

Thirteen variations of stainless steel coilforms were tested, hence the designator "SST-13" on the field gage. The variations included changes in coilform wall thickness, coilform length, routing of the copper wires, and several hybrid assemblies with the section of the coilform containing the wires made of magnesium alloy to provide additional mechanical damping. (This latter version proved quite promising but was discontinued due to the practical difficulty of mating the

stainless steel and magnesium parts in a reproducible manner. If vibration problems occur with the present design, it may be desirable to re-examine the hybrid configurations.)

Once the mechanical design of gage was completed, tests were made to maximize the gage output without increasing the gage risetime. In these tests, an SST-13 coilform was wrapped with a number of coils of wire and impact tested. The gage was then disassembled and rewrapped with an increased number of turns and retested. The results of the test series indicated that, in terms of gage risetime vs. number of turns, risetime is relatively constant at 10-13 μsec for $N < 45$ turns and rise nearly linearly thereafter to $\sim 25$ μsec at $N = 120$ turns. Since increasing the number of turns leads to increased inductance and thus increased risetime, one can conclude from the results that the risetime of the gage is inductance-dominated for number of turns $N > 45$. The increase in risetime due to the added mass of copper wire for increasing N is of secondary importance.

For $N < 45$ the risetime is approximately constant, possibly indicating a primary dependence of risetime on mechanical, rather than electrical characteristics. The selection of $N = 60$ turns for the field gage is a compromise between low risetime and high electrical output.

Electrical Characteristics of the Gage Circuit

The gage and the resistor terminating the coaxial cable connecting the gage with the recording system form an LCR circuit with mutual inductance to the gage housing and with the pickup coil of the gage acting as a current source. While it is possible to provide critical damping of the circuit (which will tend to minimize the electrical

risetime) by choosing the proper value for the termination resistor, it was found experimentally that varying the termination resistance over the range of interest (50-300 Ω) did little to affect the risetime. Thus the termination resistance of 95 Ω was chosen to match the RG22 twinax cable impedance rather than to provide critical damping.

## The Burnwire... A Shipping and Handling Aid

Because of the necessity for transporting and installing assembled gages at the underground test site, a positive method of assuring the proper positioning of the specimen/substrate in its holder was required. After examining several alternatives, the "burnwire" technique shown in Figure 27 was chosen.

A 0.125 mm (.005") copper wire is led through holes in the tamper and specimen/substrate and keeps the pieces from moving until the wire is vaporized by the incident radiation. The holes are drilled at slight angles to the direction of radiation to prevent radiation from passing directly through the pieces. The mass of wire vaporized within the gap is small relative to the mass of vaporized specimen material and does not contribute appreciably to the tamped impulse.

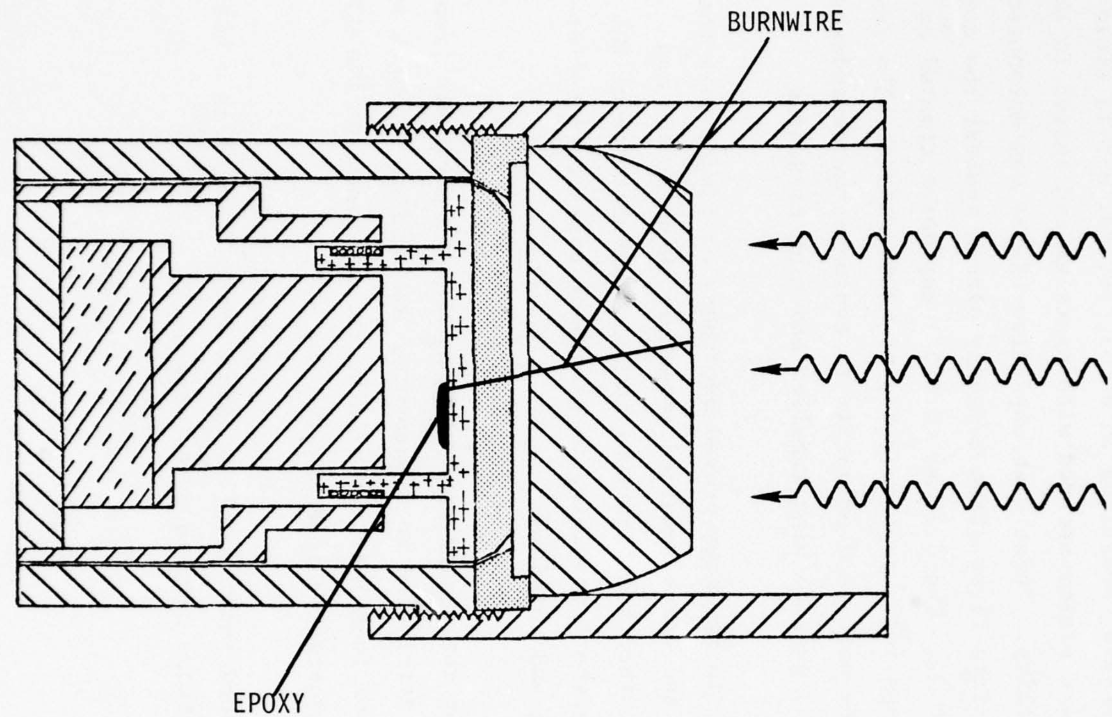


Figure 27. The field gage is secured for transportation and installation with copper "burnwire."

## SECTION VI
## HIGH EXPLOSIVE TEST SERIES

To provide a high amplitude, short duration pulse more representative of the shockwave conditions in a UGT, several SST-13 field model TRI gages were plasma-sprayed with tantalum and tested in the ETI H.E. test facility. Sheet high explosive LX-13* was detonated against a buffer plate-flyer plate assembly placed against the gage as shown in Figure 28. The 0.39 mm (0.015") explosive created an impulse of ∿15 ktaps and a gage velocity of ∿3000 cm/sec. The results of the series were used primarily to evaluate the ruggedness and risetime of the gage to high impulses and high pressures.

Modifications to the gage proved necessary to insure that the copper wire coils and leads remained intact at these stress and velocity levels. Other modifications included elimination of the gage/magnet spring, where possible, to eliminate possible interference of the spring and coilform.

A tendency for the plasma-sprayed specimen to delaminate from the substrate was attributed to a suspected low bonding strength supplied by the sprayer (not Y-12, as will be the specimens on the UGT), and to the overly-energetic impulse from the H.E.

Gages were tested individually and in a group mounted in a UGT cylinder. Interactions between gages were small.

*Furnished by G.S. Dzakowic of LLL.

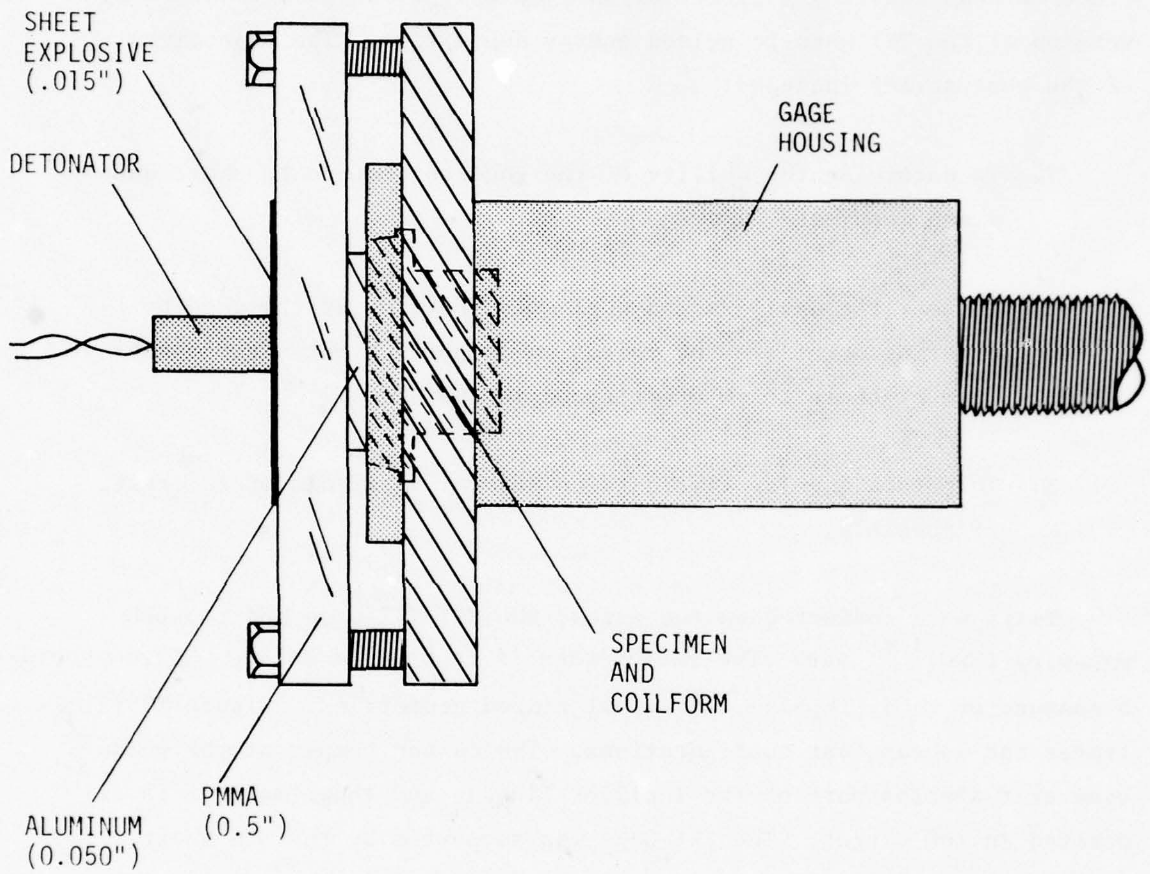


Figure 28. The H.E.-driven flyer tests produced a high amplitude, short duration pulse more closely approximating the UGT conditions.

## SECTION VII

## ELECTRON BEAM DEPOSITION TEST SERIES

Two test series conducted at the Boeing Company's FX-75 pulsed electron beam facility yielded information on the response of an early version of the TRI gage to pulsed energy deposition. The objectives of the test series included:

1. To determine the ability of the gage to respond to short duration impulses

2. To test the anti-jam and anti-weld features of the gage by creating quantities of molten and vaporized metal representative of those to be experienced in the UGT

3. To obtain impulse-time data on several materials of interest, if possible.

Tests were conducted on two gages, the ETI TRI gage and the LLL makewire (MWG)[4] gage. The latter gage is to be used in the UGT to provide a measure of total impulse in several tamped geometries. Figure 29 illustrates the e-beam test configurations. The carbon tamper at the guide cone exit absorbs part of the incident fluence and the remainder is deposited in the target. The TRI Gage was supported by the MWG shaft so that TRI and MWG data could be obtained on the same test.

The test series were conducted by Mr. N.H. Froula* and Mr. E. Stretanski,* of K-Tech Corp., co-authors of this Section. An expanded version of the following description of experiments is contained in reference 5.

---

*Currently with Corrales Applied Physics Company, Corrales, N.M.

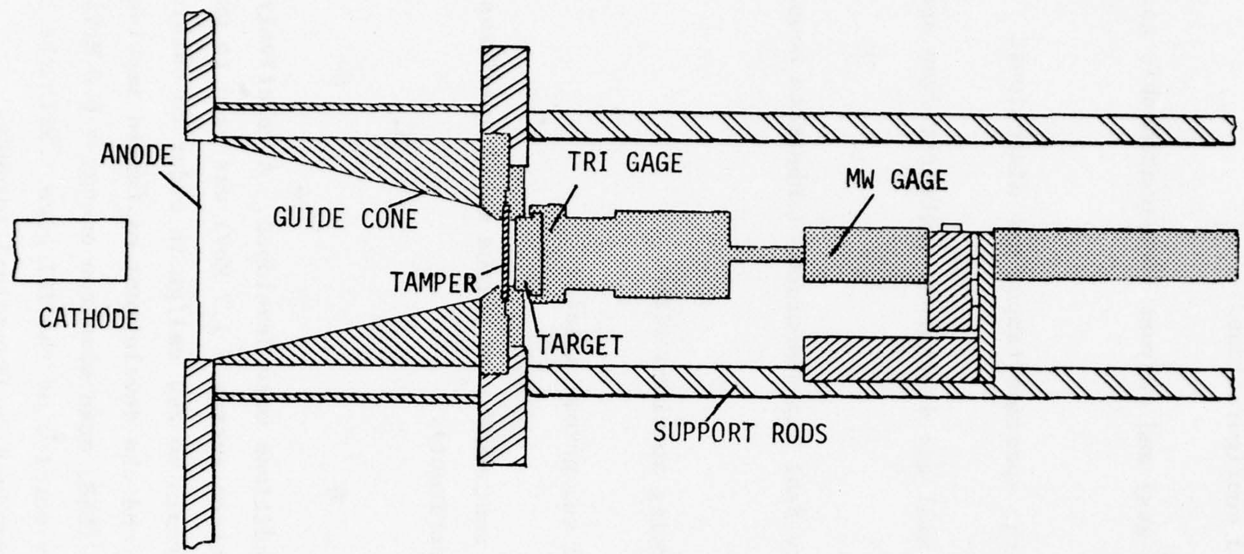


Figure 29. The TRI gage/makewire gage tamping experiment on the Boeing FX-75 electron-beam machine.

Test variables in the electron-beam series included:

1. Tamped and untamped configurations.

2. Metal (condensable gas) and polymer (non-condensable gas) specimens.

3. Effect of varying the specimen/tamper gap dimensions.

4. Effect of primary seal gap dimensions (substrate/gap spacer gap) on gage velocity.

5. Effect of secondary seal gap dimensions (substrate housing gap) on gage velocity.

6. Area effect of varying specimen sizes.

7. Impulse from solid vs. porous metals.

8. Effect of organic contaminant on porous metal specimens (an accidental experiment).

BEAM CHARACTERIZATION

Two different beam conditions were developed. A relatively high energy beam (HEB, mean electron energy = 1.2 MeV) was used to uniformly heat lead and organic materials to 260 cal/gm in order to obtain a volume of vapor to study gas flow and the development of tamped impulse. A relatively low energy beam (LEB, mean electron energy = 0.8 MeV) was used to proof test an early version of the TRI gage. With the LEB, peak doses of 600 cal/gm were obtained in (tantalum) targets.

Characteristic spectra for the HEB and LEB were derived from diode current and voltage measurements and are given in Figure 30. The deposition times for these beams (FWHM, power) are 35 and 40 nanoseconds for the HEB and LEB, respectively.

For the impulse gage experiments, the HEB was used with and without a 0.18 cm (0.33 g/cm$^2$) graphite filter (tamper). The LEB was always used with eight layers of carbon cloth (0.2 g/cm$^2$), which prevented spallation of the tamper by presenting numerous thin layers of carbon to the beam. Stress equilibration was achieved during deposition time, preventing fracture. Beam characterization was also performed under these conditions.

The beam fluence was measured with an array of five 0.71-cm-diameter total-stopping graphite calorimeter elements. A central element was symmetrically surrounded by four elements with centers on a 2-cm diameter. The data from the four peripheral elements were averaged and compared with the center measurement. The HEB data in Figure 31 represent the average for three filtered (behind tamper) and three unfiltered shots, and the bars indicate the extremes for the six shots. The LEB data represent the average for filtered shots. The radial fall-off at 1 cm is 50 percent. The relative mean fluence (i.e., fluence averaged over an area relative to the center calorimeter measurement) is shown in Figure 32. The mean fluence over a particular sample area relative to the center calorimeter can be obtained from this Figure. Fluence data and statistics for the center calorimeter are given in Table II for the HEB and the LEB.

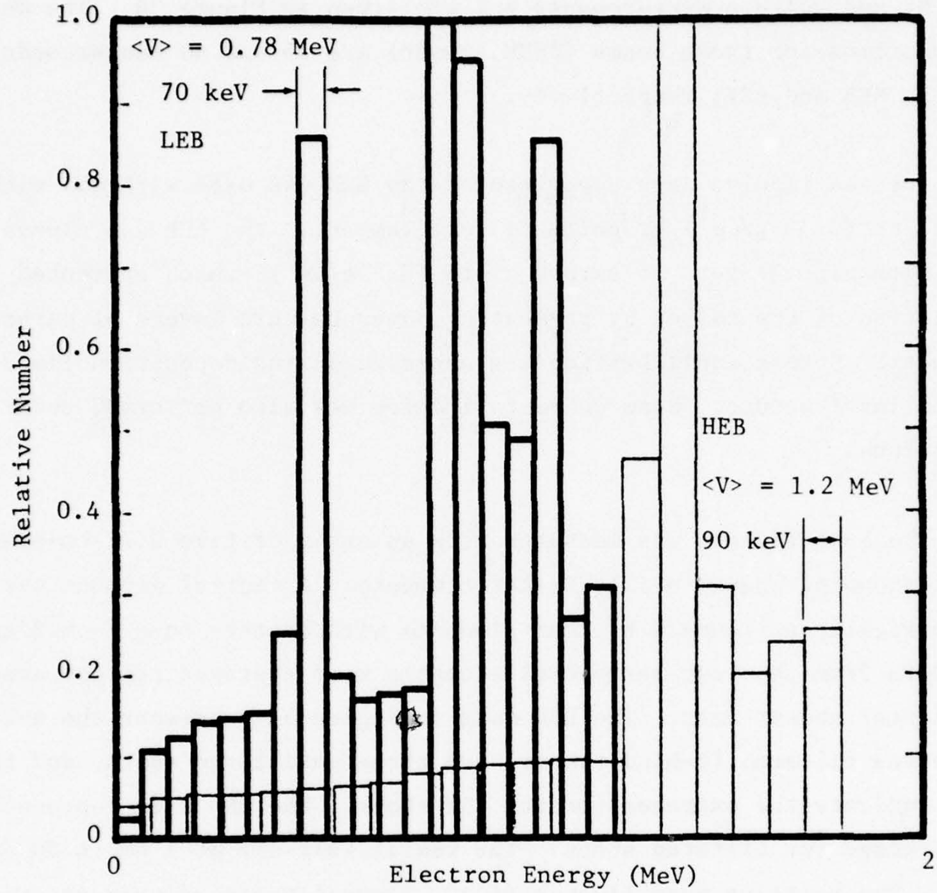


Figure 30. LEB and HEB spectra.

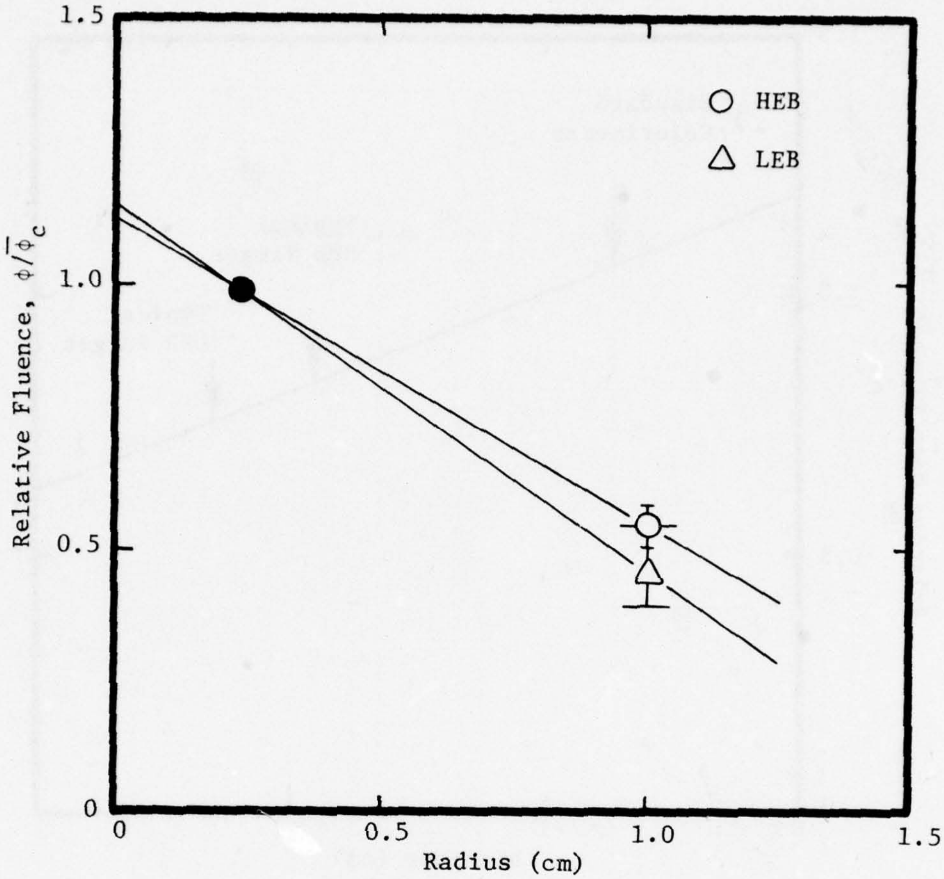


Figure 31. HEB and LEB fluence data.

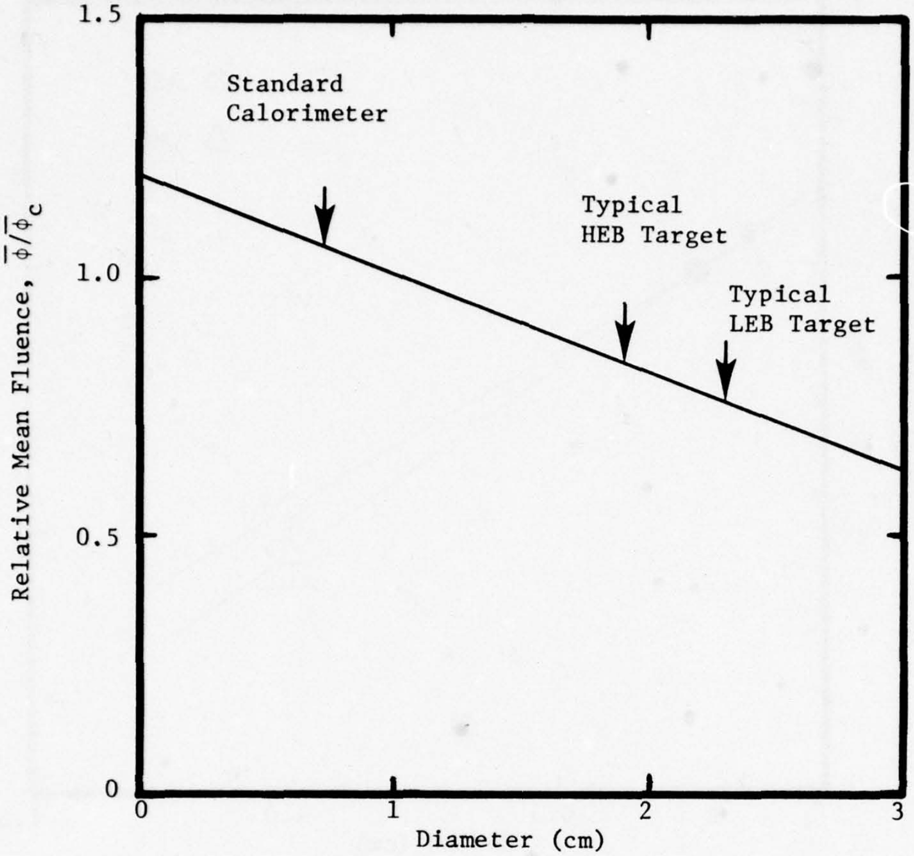


Figure 32. Mean fluence vs. diameter for LEB and HEB.

Table II

Center Calorimeter Fluence Data

| Test Series | Beam | No. of Tests | Average Fluence ($cal/cm^2$) | Average Deviation (percent) |
|---|---|---|---|---|
| 1 | HEB Unfiltered | 8 | 204 | 6 |
| 2 | HEB Unfiltered | 5 | 204 | 4 |
| 1 | HEB Filtered | 10 | 140 | 6 |
| 2 | HEB Filtered | 4 | 137 | 5 |
| 2 | HEB Filtered | 7 | 94 | 10 |

Filtered and unfiltered normalized depth-dose data obtained on the HEB with a titanium-foil-calorimeter stack are given in Figure 33. The LEB depth-dose data shown in Figure 34 are from recent transmitted fluence measurements on the same beam.[7] The mean dose characteristics over typical TRI Gage sample diameters for the HEB (1.9 cm) and the LEB (2.3 cm) were computed from the normalized depth-dose data (Figures 33 and 34), the mean fluence relative to center calorimeter fluence (Figure 32), and the average center fluence data (Table II). These results are shown in Figures 35 and 36 for the HEB and LEB, respectively. No attempt was made to adjust the depth-dose profiles for the differences in "stopping power" exhibited by the various sample materials due to their geometry (e.g., foils) and albedos.

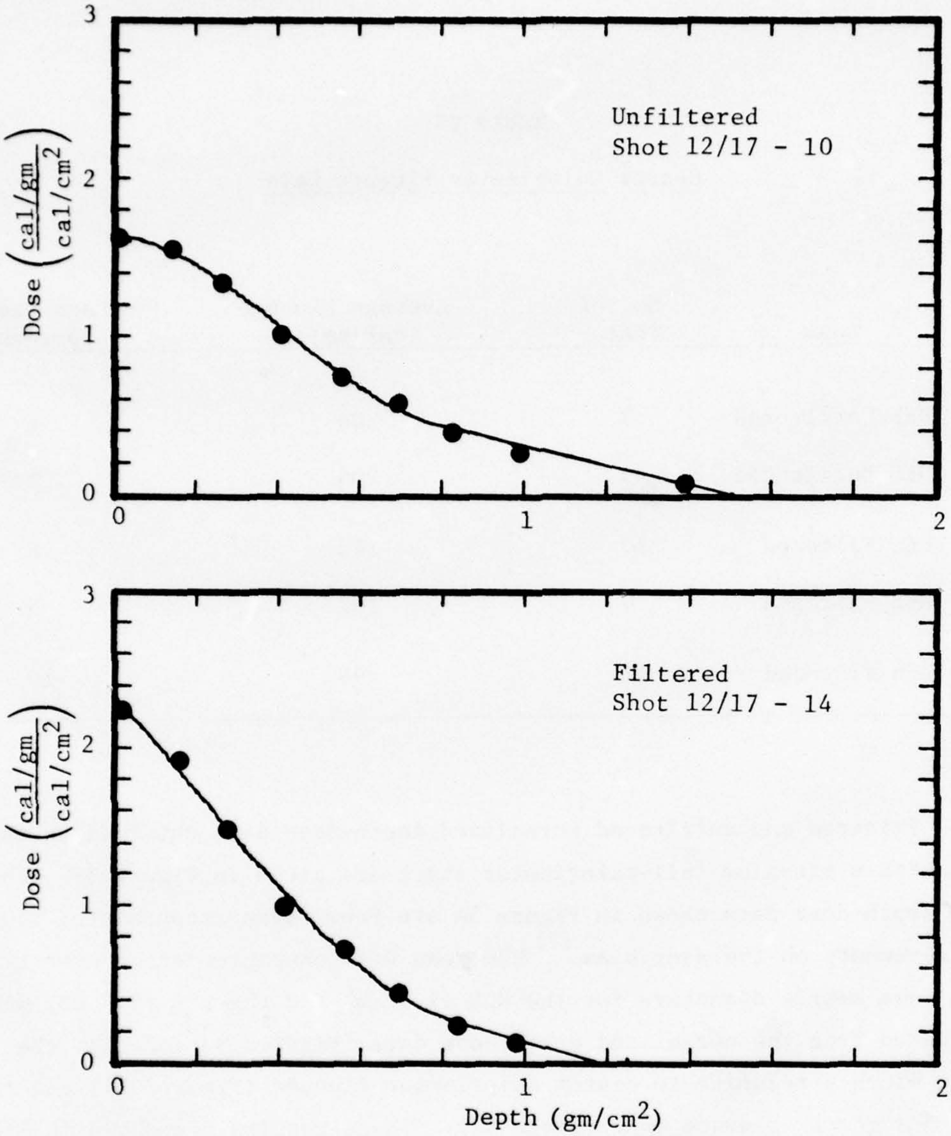


Figure 33. Normalized HEB depth-dose data.

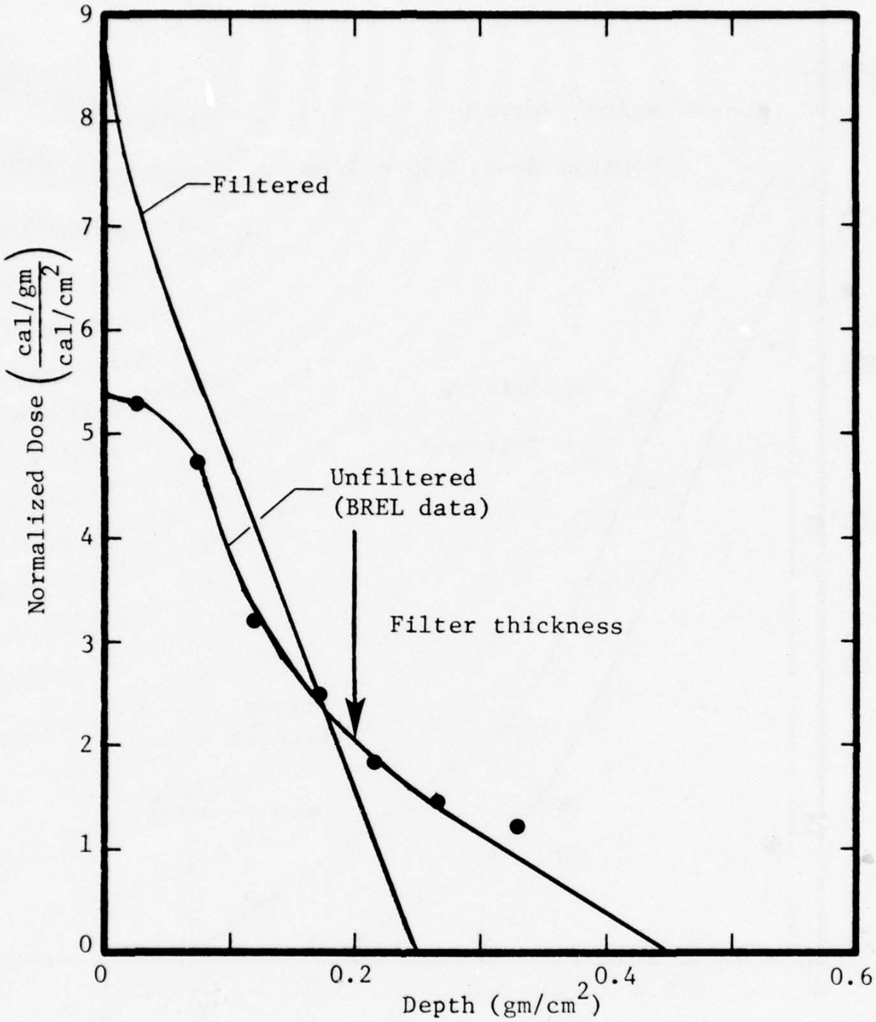


Figure 34. Normalized LEB depth-dose data.

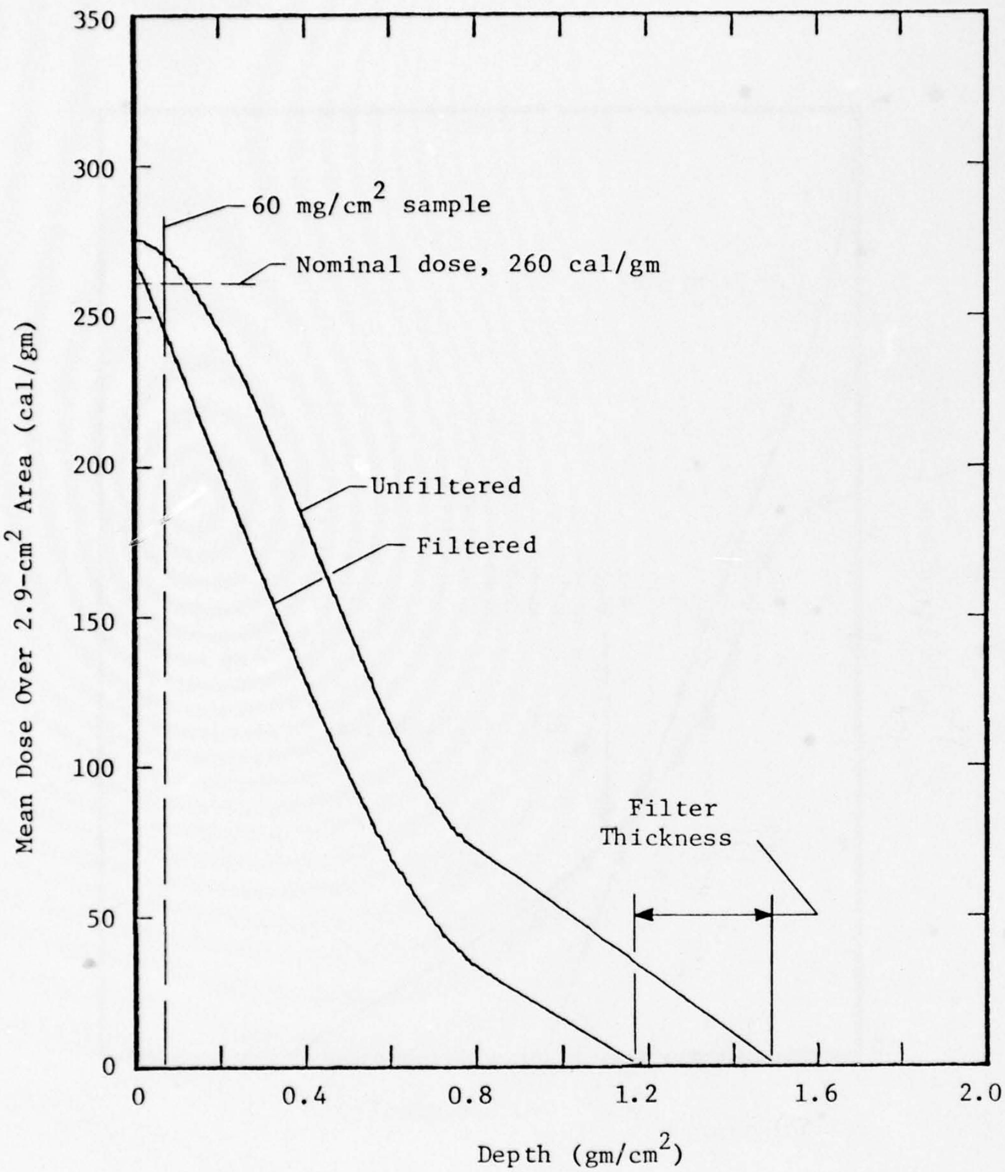


Figure 35. HEB depth-dose characteristics.

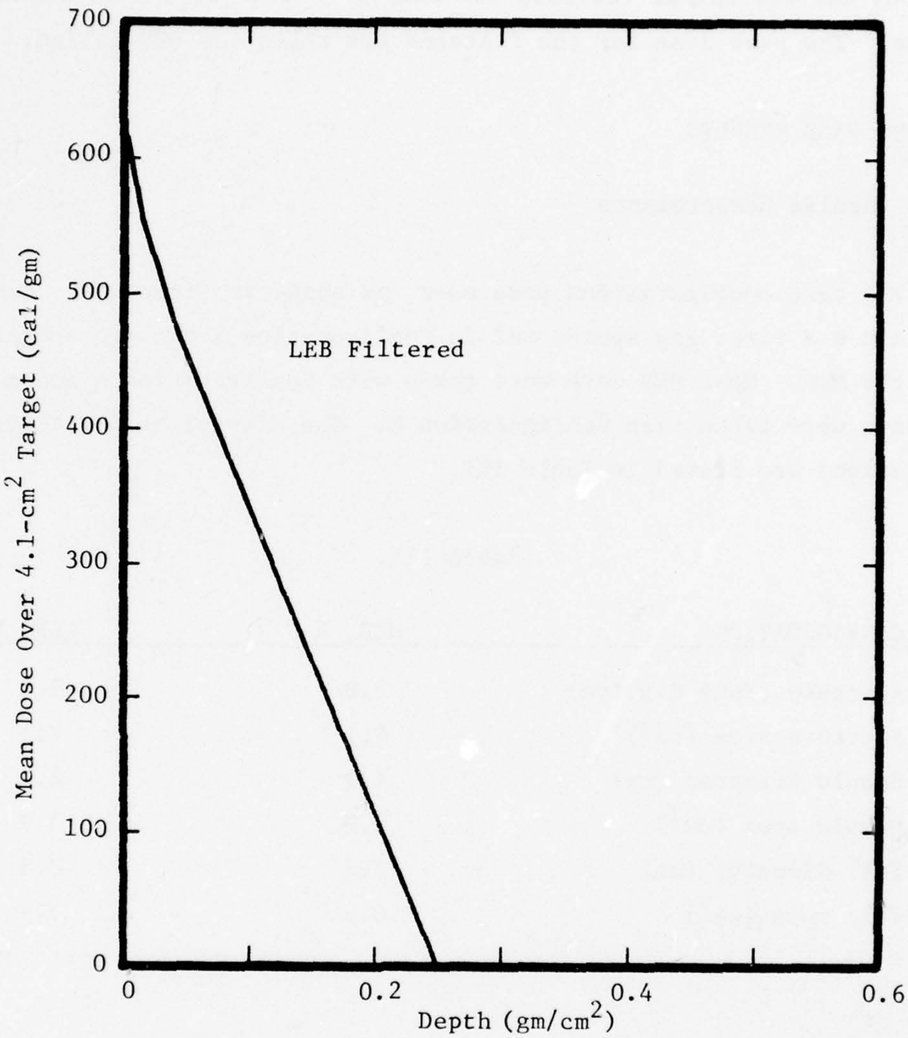


Figure 36. LEB depth-dose characteristics.

The nominal dose for the HEB samples, which were fairly uniformly heated, was 260 cal/gm for both the tamped (filtered) and untamped condition. The peak dose for the filtered LEB tests was 600 cal/gm.

## IMPULSE GAGE RESULTS

### Total Impulse Measurements

Two test configurations were used, as shown in Figure 37. Configuration A has a fixed gap spacer and in Configuration B the gap spacer moves with the MWG. Most HEB data were taken with Configuration A and most LEB data were taken with Configuration B. The dimensions for these configurations are listed in Table III.

Table III.

| CONFIGURATION | HEB, A | LEB, B |
|---|---|---|
| Aperture (MWG) dia.(cm) | 2.8 | 3.0 |
| Aperture area ($cm^2$) | 6.1 | 7.1 |
| Sample diameter (cm) | 1.9 | 2.3 |
| Sample area ($cm^2$) | 2.9 | 3.9 |
| TRI diameter (cm) | 2.3 | 2.3 |
| TRI mass ($cm^2$) | 3.9 | 3.9 |

The initial HEB tests used the MWG only and for these tests a solid graphite target was used (i.e., without the tapered plug). Note that direct comparison of tamped impulse as measured by the TRI and MWG is not generally possible because of area and mass differences. Some untamped impulse data were taken, particularly with the HEB, and reasonably

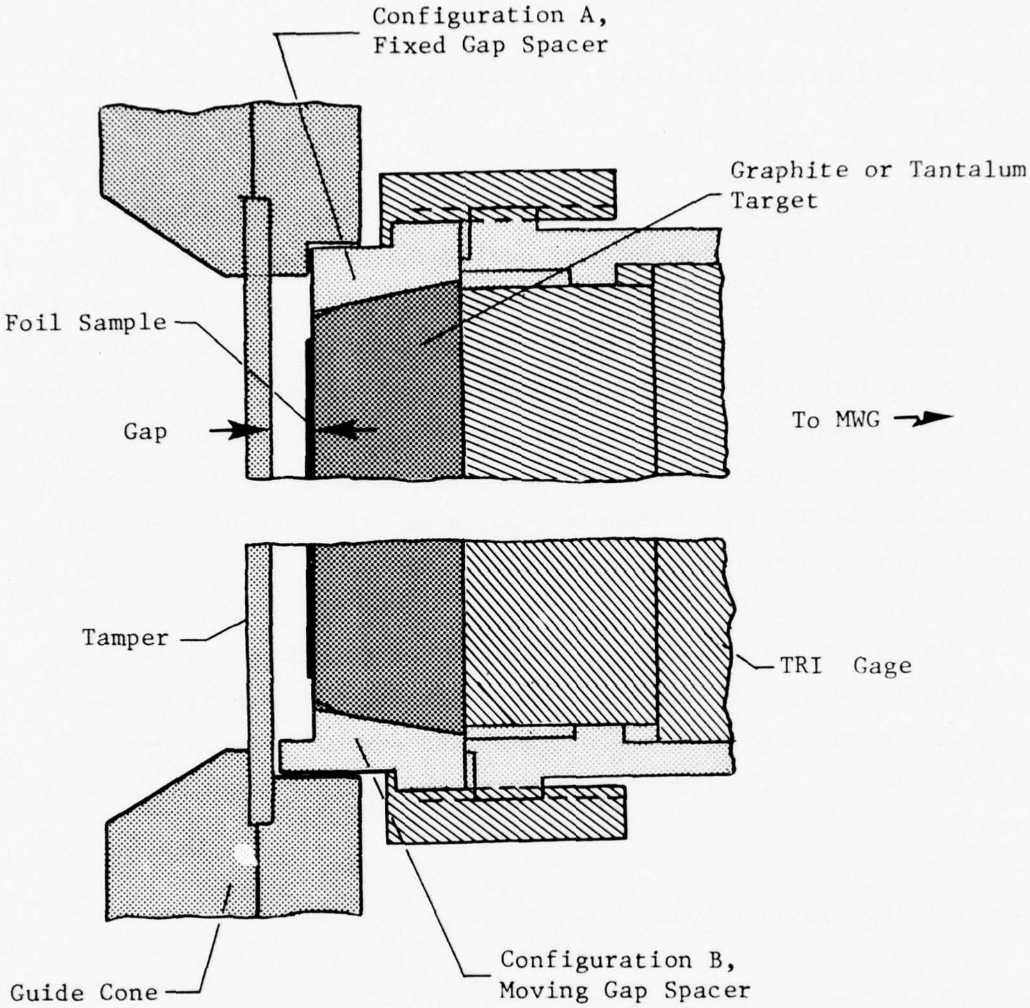


Figure 37. Test configurations.

good comparison was obtained. The gap for nearly all tamped shots was 0.13 cm.

Figure 38 presents the MWG data for acetate. The relatively low impulse achieved for the untamped configuration compared to the tamped indicates that a high volume of gas was generated and interacted with the tamper and gage in the tamped configuration. A tamper mass (or in this case, for a fixed tamper, a sample mass) effect is suggested by the lower impulse generated by the one 66 gm point, and by the very low impulse points for the two tests using the 10 gm TRI Gage. All other tests used the MWG only. Tamped impulse on other organic materials in the HEB gave the results shown in Figure 39.

Figure 40 presents the HEB MWG data for thin lead samples over graphite targets. The graphite tampers fractured slightly on nearly all tests with samples 50 $mg/cm^2$ thick and sheared out on tests with thicker samples. The tamper increased the impulses about a factor of two.

## Time-Resolved Impulse Measurements

The TRI gage prototypes available during the electron-beam test series (graphite on metal substrates with polymer coilforms) showed considerable vibration in the early portions of the record ($<100$ μsec). Smoothing the data, either by eye or by computer, allowed measurement of impulse after approximately 20 μsec, however. Although the series was designed primarily to test gage operation, interesting and possibly useful data was obtained on the physics of tamped impulse generation.

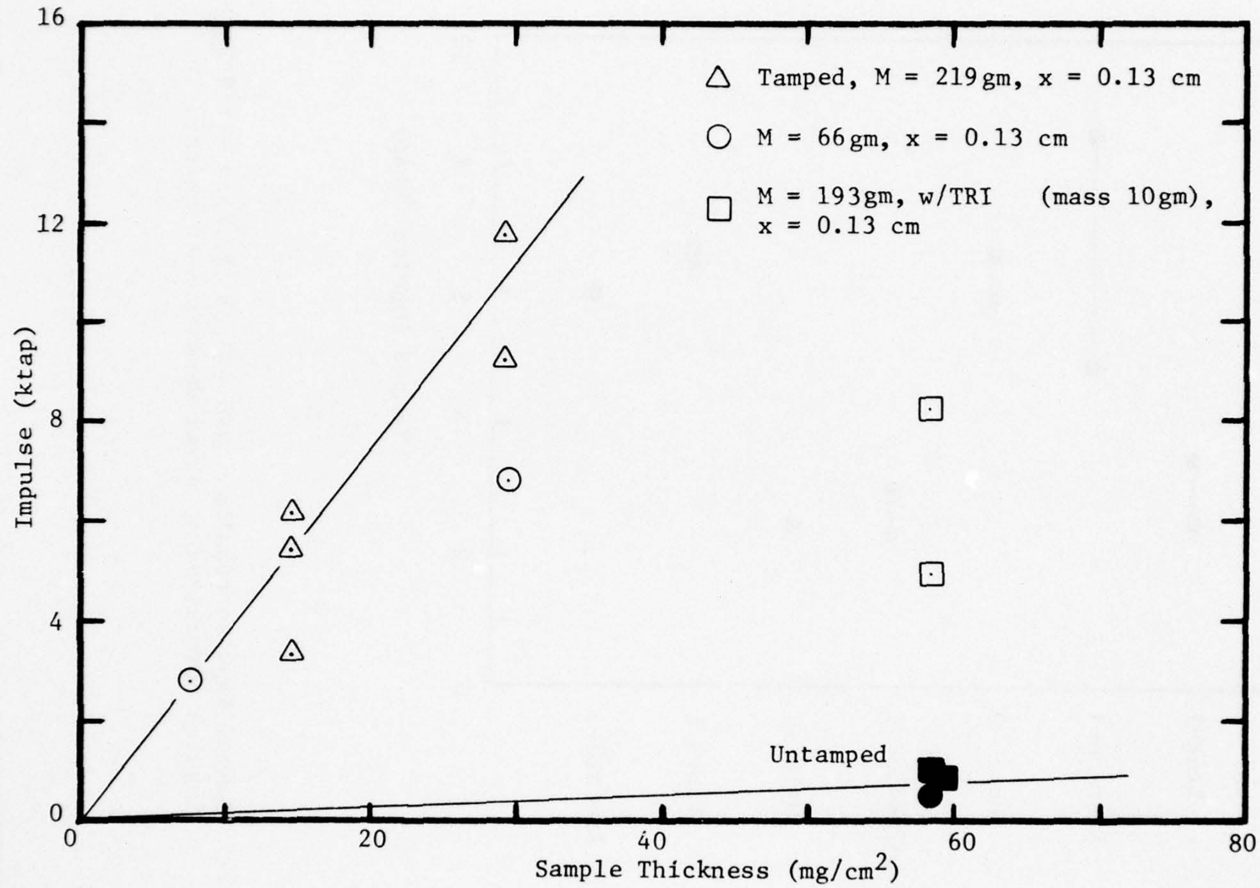


Figure 38. MWG acetate results.

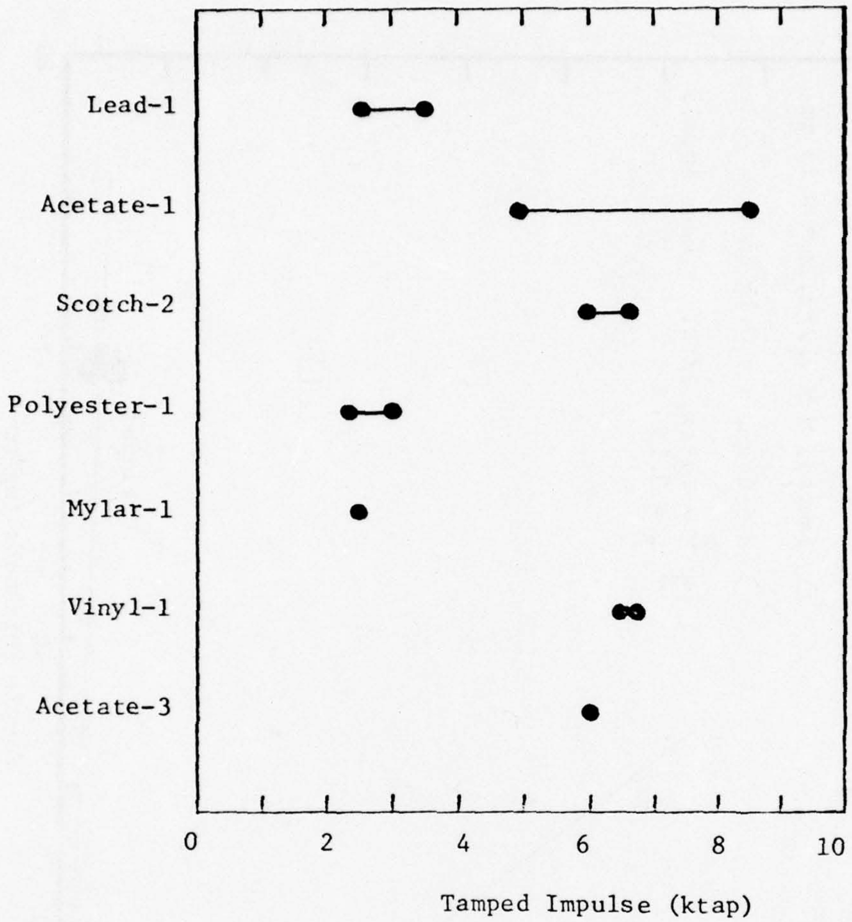


Figure 39. Tamped impulse results. gap = 0.13 cm, mass = 173 gm, impulse normalized to areal density = 60 mg/cm$^2$.

---

* Except acetate sheet = 219 gm and lead = 66 gm.

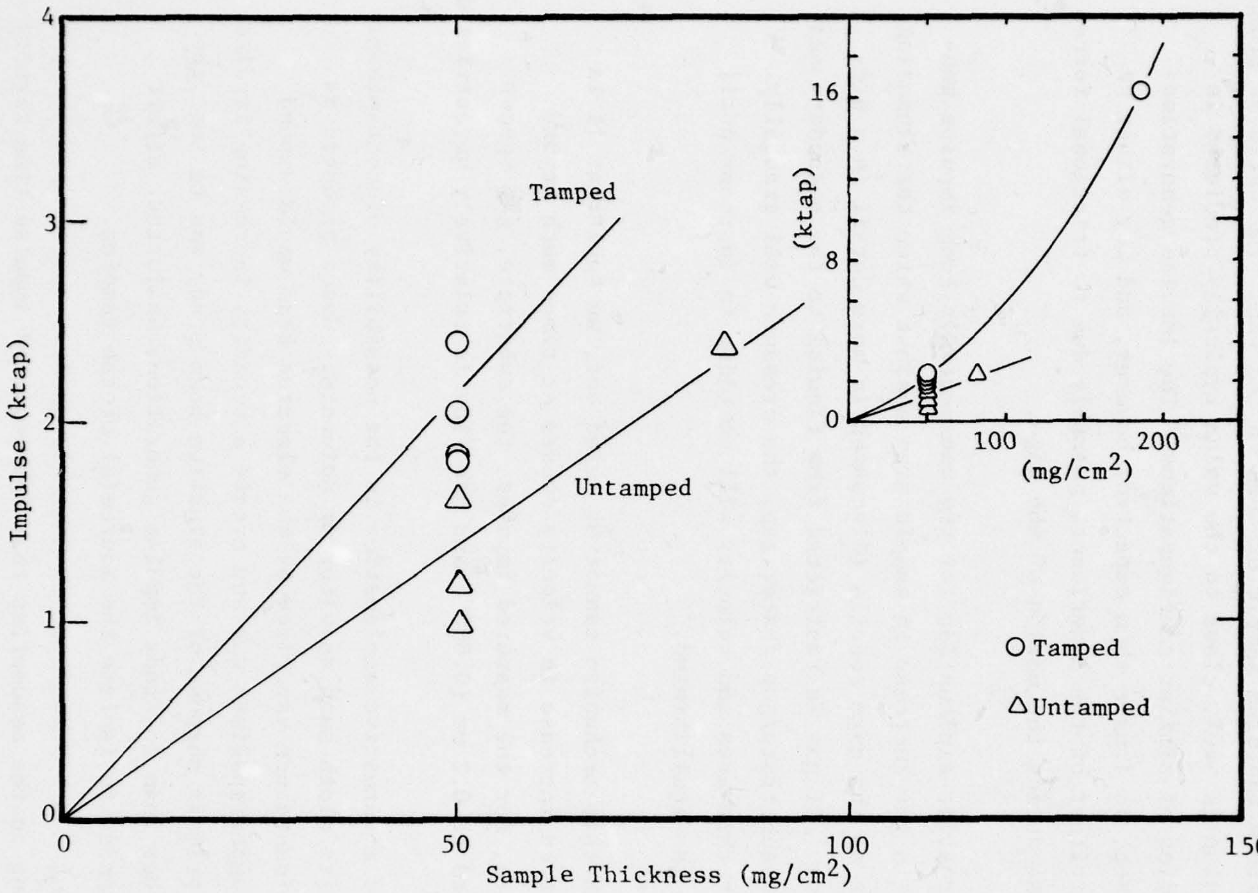


Figure 40. MWG lead results—lead samples, graphite tamper.

Figure 41 shows typical results of the TRI gage in a tamped configuration with a tantalum sample exposed in the LEB. The ratio of prompt to total impulse is ∿60%, close to the value typically predicted in computer studies of similar configurations. The impulse generation time, ∿500 μsec, is longer than expected, however, and may either be real or an artifact of the experiment, possibly due to frictional forces being overcome during the motion of the gage.

An alternative explanation for the unexpectedly long impulse generation time is the increase in sample area against which the expanding gases may act as the gage recoils (discussed in more detail in a previous Section). If gas is restricted from flowing to the secondary seal by the narrow substrate/gap spacer gap, the pressure will gradually increase over this area and velocity will continue to increase until the pressure has equilibrated.

Although this mechanism cannot be ruled out, we feel that it is unlikely that an increase in velocity occurs at times much beyond 100 μsec where, for the measured impulse, the substrate, gap spacer gap has opened to 0.2 mm (0.008") and gas flow is relatively unrestricted.

A second alternative explanation is the possibility of contaminants in the graphite cloth such as water or solvents. Gases produced as these contaminants are vaporized by the electron beam would expand within the tamper/specimen gap and create a steadily increasing impulse. Because the primary purpose of the electron beam study was to test the TRI gage rather than to study impulse generation, no further effort could be expended to isolate the source(s) of the tamping.

Operating on the assumption that the measured impulse-time history is correct, we can smooth and then differentiate the data to obtain the

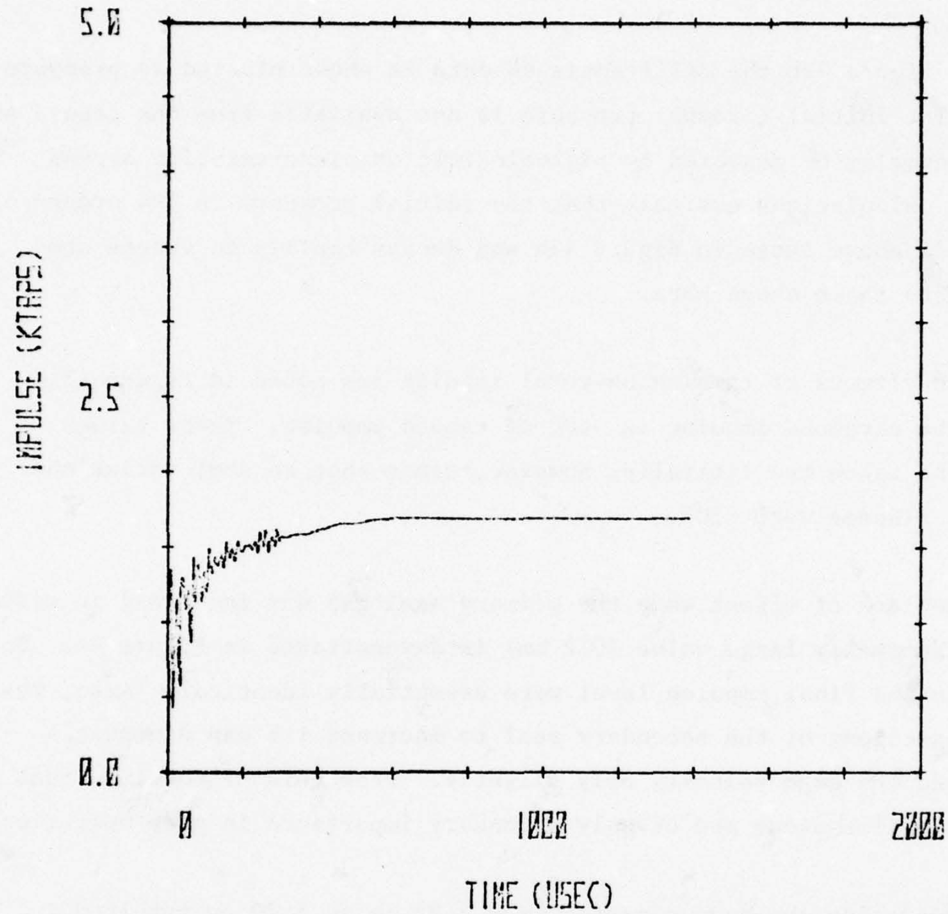


Figure 41. TRI gage tantalum data. LEB, sample area = 4.1 $cm^2$, TRI gage mass = 30 gm.

pressure-time profile which created the gage motion. The data from test 3/21-12 was smoothed using the FFT routine and is shown plotted in Figure 42a.

In Figure 42b the differentiated data is shown plotted as pressure-time. The initial (prompt) pressure is not available from the record and would normally be measured by piezoelectric or piezoresistive stress gages. Calculations estimate that the initial pressure is 3-4 orders of magnitude above those in Figure 42b and decays rapidly to values comparable to those shown here.

The effects of tamping on total impulse are noted in Figure 43, where the untamped impulse is $\sim$40% of tamped impulse. These values cannot be taken too literally, however, since shot to shot variations in beam fluence were $\sim$10%.

The lack of effect when the primary seal gap was increased in width to an abnormally large value (0.2 mm) is demonstrated in Figure 44. Both risetime and final impulse level were essentially identical. Also, removing sections of the secondary seal to increase its gap dimensions decreased the gage velocity only slightly. From this we conclude that these gap dimensions are of only secondary importance in gage operation.

Decreasing the gage diameter from 2.32 cm to 1.70 cm resulted in a 37% increase in measured impulse, as shown in Figure 45. The expected increase from the higher mean fluence in the beam center is $\sim$40% (Figure 31).

The effect of an organic contaminant on impulse production is demonstrated in the Figure. Eastman 910 cement had been used to glue a thin foil of tantalum over the tantalum specimen for an earlier test. Since it was

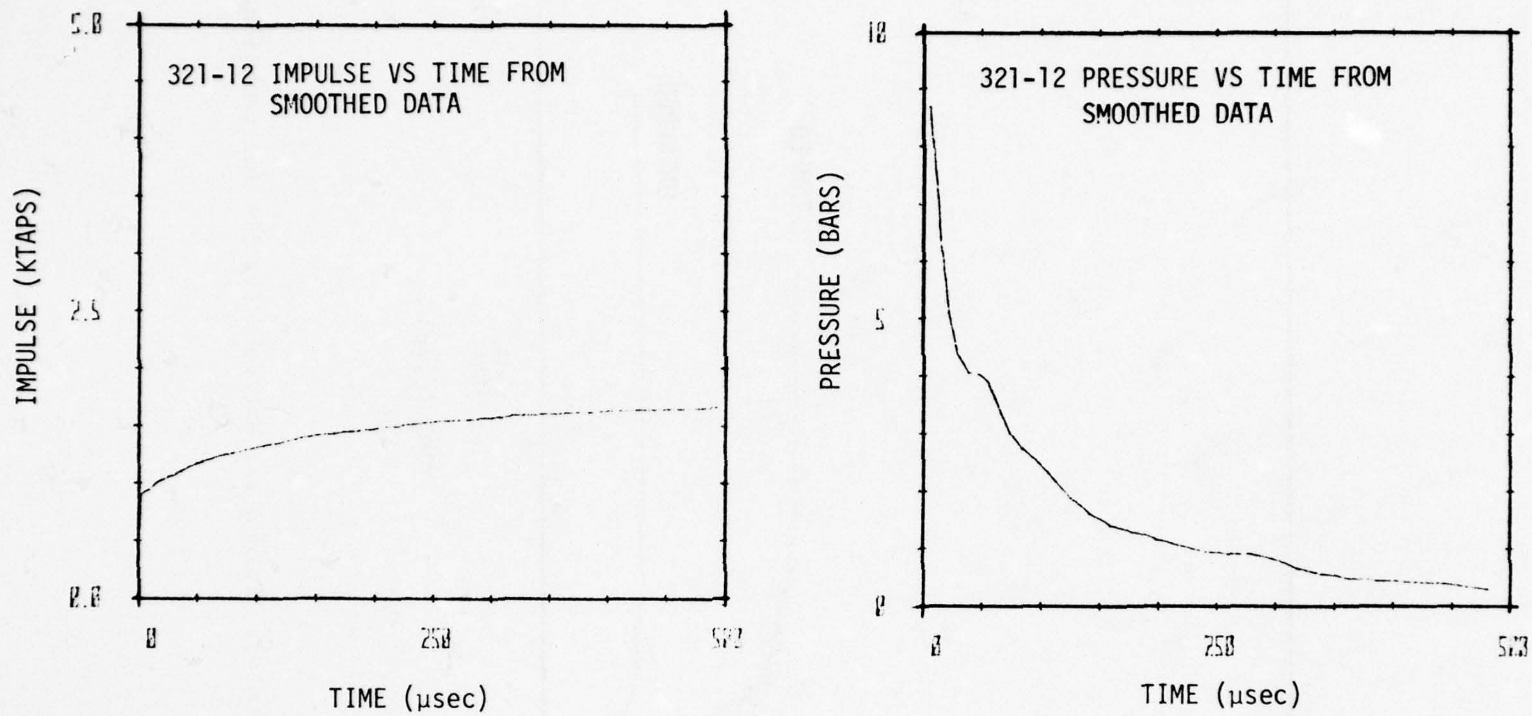


Figure 42. Smoothed data from tamped tantalum test of Figure 41 is differentiated (42b) to obtain pressure-time history of tamped impulse.

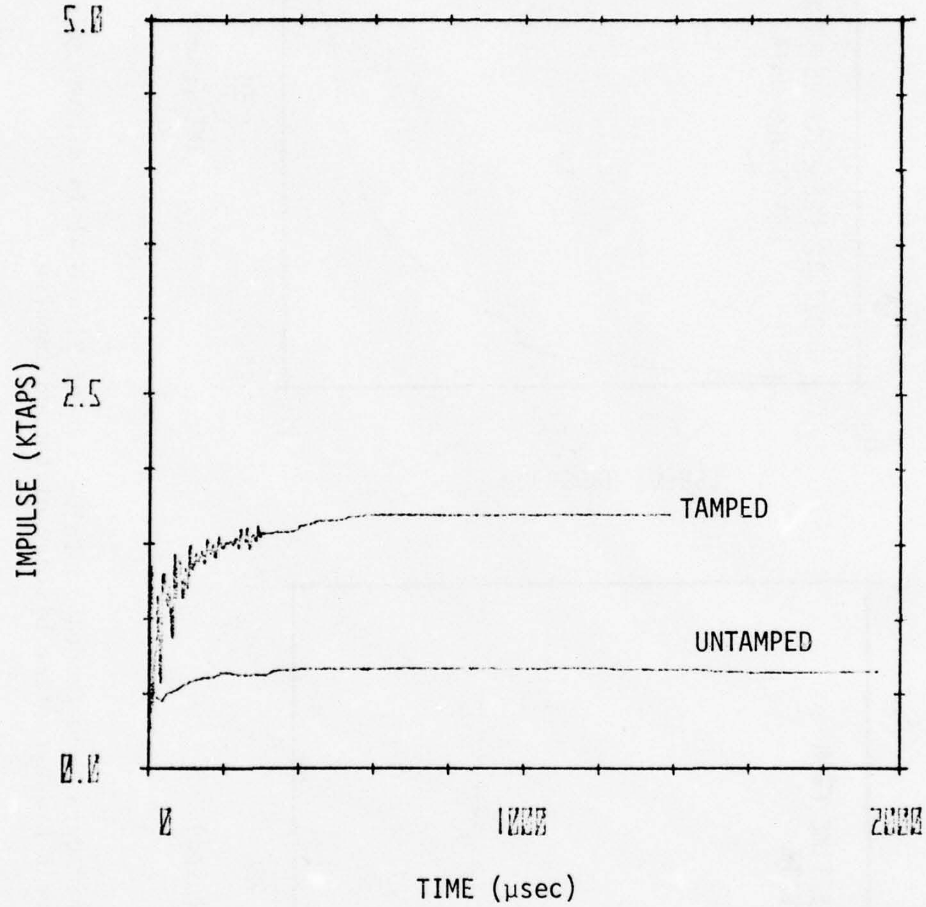


Figure 43. Tamped vs. Untamped Results for tantalum.

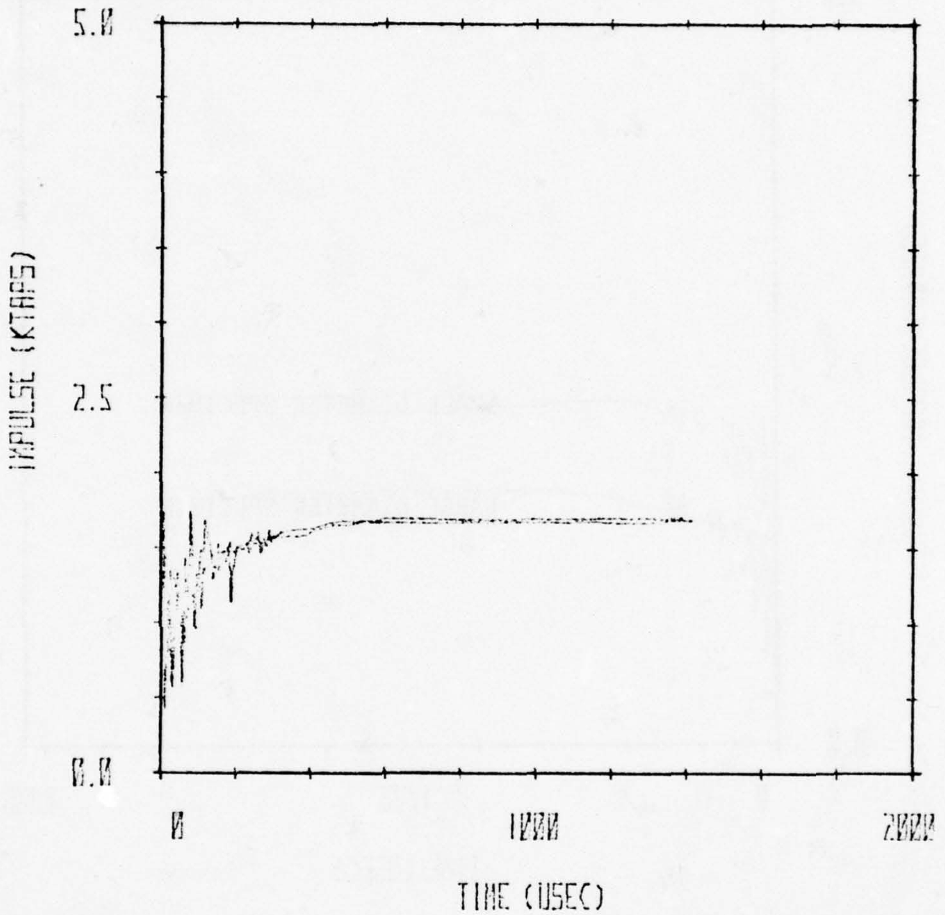


Figure 44. The effect (or lack of it) of greatly increasing the secondary seal gap is demonstrated by these tests on tantalum.

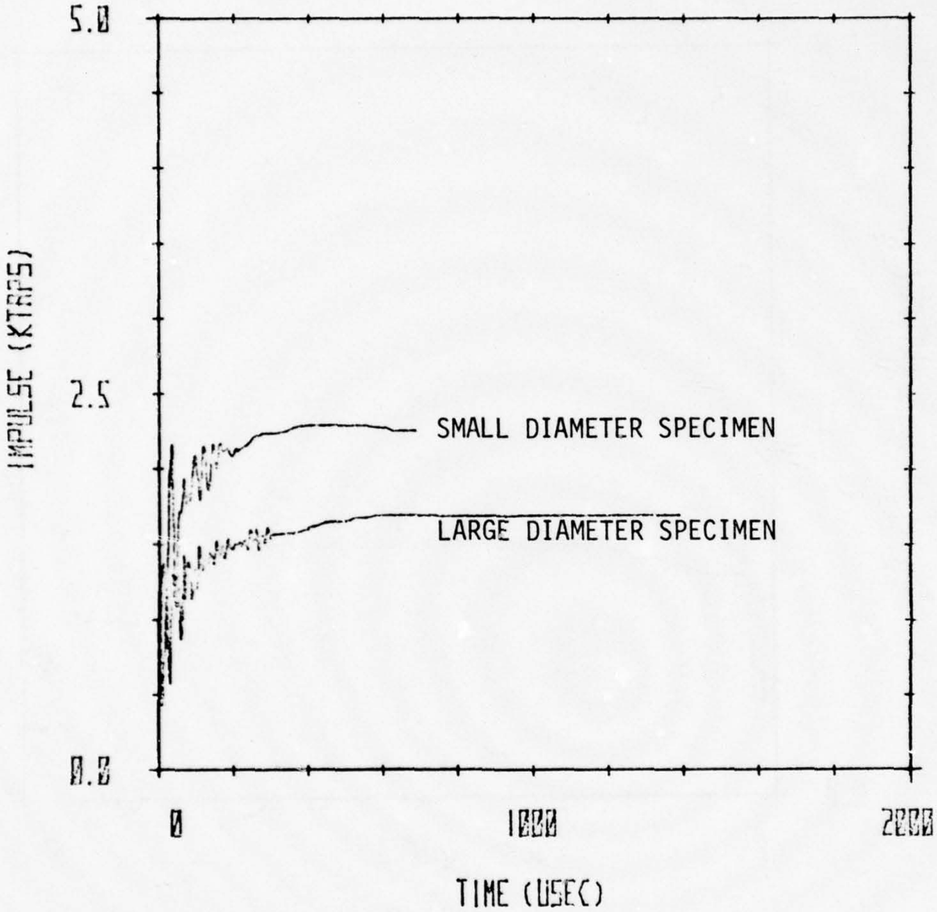


Figure 45. The effect of a small diameter specimen sampling only the higher fluence center of the beam is demonstrated by the difference in recorded impulse.

AD-A075 320 EFFECTS TECHNOLOGY INC SANTA BARBARA CA F/G 14/2
TRI-THE DEVELOPMENT OF A FAST-RESPONSE TIME-RESOLVED IMPULSE GA--ETC(U)
APR 78 W M ISBELL, W J NAUMAN DNA001-76-C-0357
UNCLASSIFIED ETI-CR-78-550 DNA-4658F NL

2 OF 2
AD
A075320

END
DATE
FILMED
11-79
DDC

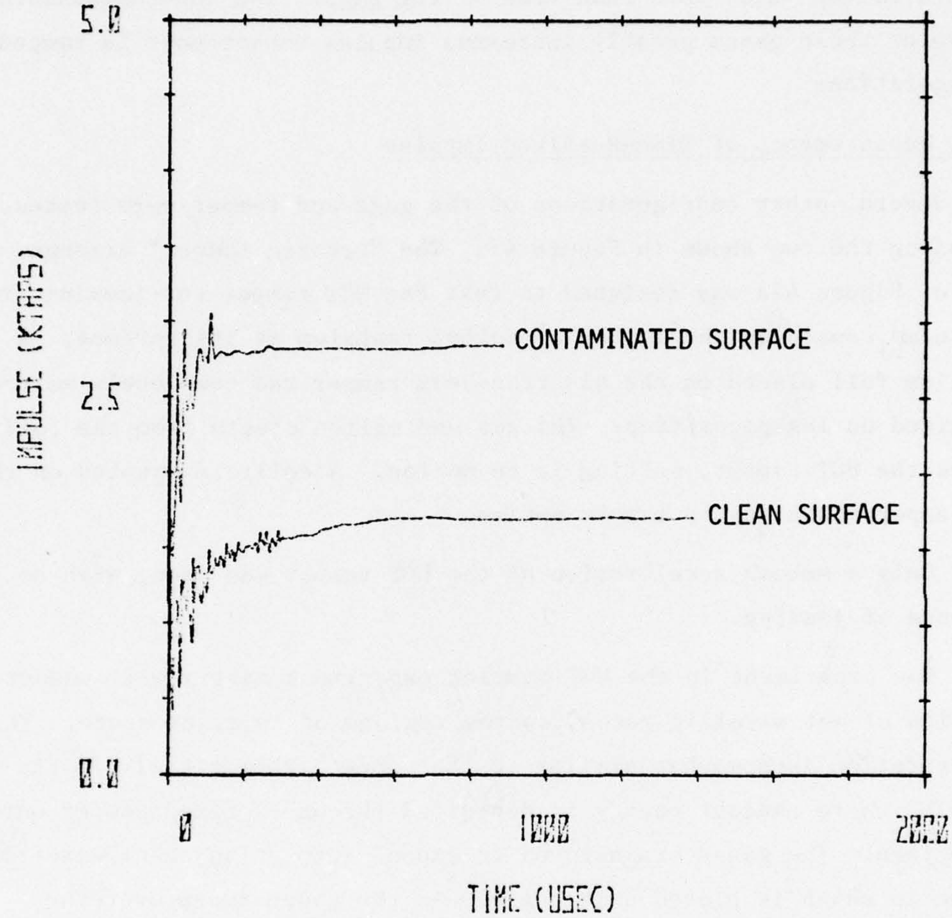


Figure 46. The sample contaminated with adhesive produced ∿65% more impulse.

impossible to completely remove the cement using solvents, we vaporized residual adhesive in an e-beam test, thus increasing the impulse by $\sim$65%.

Finally, all tests with organic materials showed risetimes comparable to the $\sim$1500 μsec read time of the gage. The non-condensable nature of these gages greatly increases impulse enhancement in tamped configurations.

Other Measurements of Time-Resolved Impulse

Several other configurations of the gage and tamper were tested, including the two shown in Figure 47. The "reverse tamper" arrangement of Figure 47a was designed to test the UGT tamper for jamming from the pulse caused by the impact of molten tantalum at its surface. A thin tantalum foil placed on the electron-beam tamper was completely melted or vaporized during deposition. The gas and molten ejecta from the foil struck the UGT tamper, setting it in motion. A coilform mounted on the UGT tamper measured the tamper motion.

Only a smooth acceleration of the UGT tamper was seen, with no evidence of jamming.

One experiment in the UGT tamping experiment matrix will measure the flow of hot metallic gases towards regions of lower pressure. The configuration is somewhat similar to that shown schematically in Figure 47b, where radiant energy is deposited through a fixed tamper onto a specimen. The gases are allowed to expand into an adjacent gas-free volume in which is placed a TRI gage. As the gases sweep over the gage, the average pressure is recorded by gage motion.

A potential problem with this arrangement is the cocking and possible jamming of the gage which may occur as the gage is asymmetrically loaded by the gases sweeping over its surface. Test 3/23-20, using acetate instead of tantalum to produce larger amounts of gases, showed no evidence of jamming and produced a smooth (though low amplitude) record.

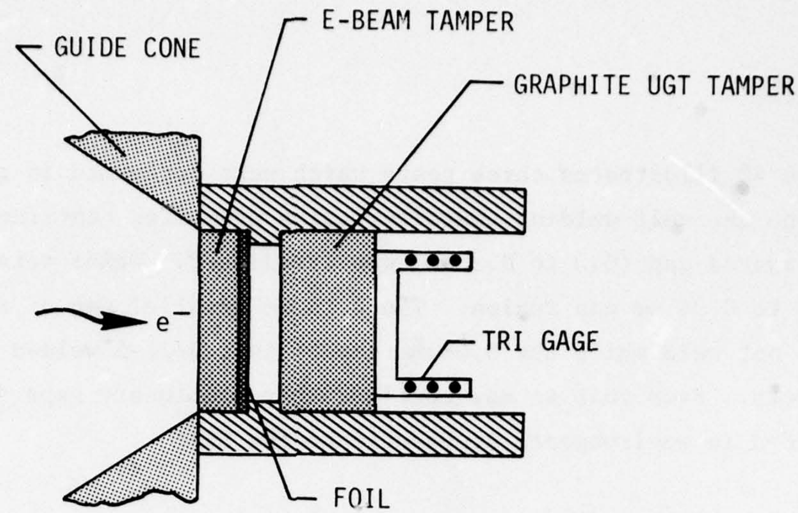


(A)

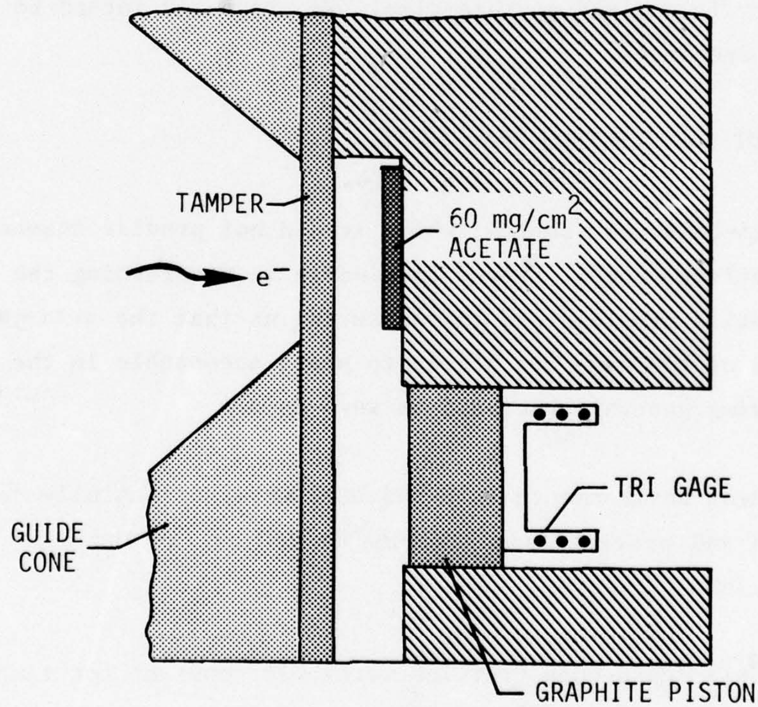


(B)

Figure 47. The "reverse tamper" arrangement (47a) tested the tamper for jamming by the impact of molten metal on its surface. The "gas flow" arrangement (47b) measured the expansion of gases towards regions of lower pressure.

## Welding Tests

Figure 48 illustrates three tests which were performed in the LEB to determine the self-welding characteristics of molten tantalum. In test 3/18-7 a tapered gap (0.0 to 0.3 mm) was irradiated. Welds were seen in the 0.0 to 0.06 mm gap region. The 0.15 mm parallel gap of test 3/21-3 did not weld while the 0.08 mm gap of test 3/21-5 welded in several spots. From this we may conclude that stationary gaps $\leq 0.10$ mm can be welded in environments comparable to the LEB.

No welds were observed between parts moving relative to one another and no evidence was seen of retardation of gage motion by the forming and breaking of weld bridges. Whether or not the bi-angle truncated cone specimen, designed to prevent welding, is really necessary or is only added safety is unclear at this time. We presently intend to include it in UGT specimens.

## CONCLUSIONS ABOUT THE ELECTRON BEAM TESTS

The electron-beam test series, while it did not provide answers for all the questions sought, proved invaluable in determining the sources of potential problems and in reassuring us that the anti-jam, anti-weld design of the gage was likely to prove acceptable in the UGT. The following general observations were made.

1. Two e-beam environments (HEB and LEB) were successfully developed and provided sample doses of 260 cal/gm and 600 cal/gm.

2. The sample depth-dose profiles were held constant for tamped and for untamped conditions.

1.0 mm

TEST 3/18-7

0 - 0.3 mm Tapered Gap. Samples welded in the 0 - 0.06 mm region.

TEST 3/21-3

0.15 mm Parallel Gap. Samples did not weld.

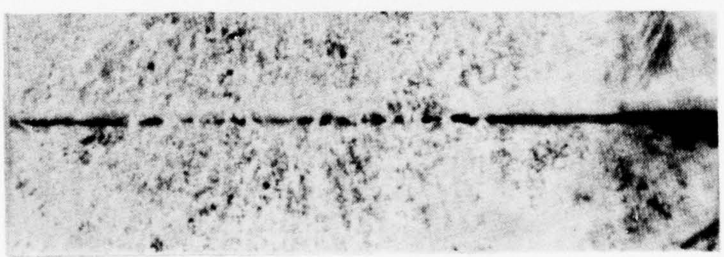

Test 3/21-5

0.08 mm Parallel Gap. Samples welded in many spots.

Figure 48. Passive weld test with tantalum samples.

3. TRI gage "proof tests" with tantalum targets were successful. Vibrations in the gage output were small enough that impulse measurements could be made microseconds after deposition.

4. Welding and gas leakage do not appear to be problems with the current TRI gage design.

5. The simulated UGT tamper and lateral gas flow gauge worked smoothly without jamming or welding.

6. Time resolved tamped impulse data for acetate, and perhaps lead and tantalum, indicate that at least 500 microseconds are required to develop 80 percent of the total impulse under the conditions of these tests.

## SECTION VIII

## GAGE CALIBRATION AND DATA ANALYSIS
(D. K. Sangster)

This Section describes the calibration technique and the computer routines used to analyze the gage records. The description here is relatively brief and describes the experimental and analytical techniques without listing the computer programs. Complete listings of the programs are available on request from the authors.

The following sequence of operations is performed to calibrate the gage and to analyze the test results:

1. Pre-test calibration of gage voltage vs. velocity output for individual gages.

2. Installation of gage and performance of test. Gage records are obtained as oscillographs or on magnetic tape.

3. Digitization of records.

4. Conversion of digitized voltage-time record to velocity-time record using data from a pre-test calibration.

5. Conversion of velocity-time record to impulse-time using gage mass and exposed area.

6. Application of Fast Fourier Transform (FFT) technique to gage record to remove periodic vibrations (optional).

7. Differentiation of velocity-time record to obtain pressure-time history at specimen surface.

The calibration and data reduction of time-resolved impulse gage output traces is performed by two computer programs written for the Hewlett-Packard 9830A calculator. The data is digitized with the use of an HP 9864A Digitizer and plots are generated by the HP 9862A Calculator Plotter. The removal of periodic electromagnetic vibrations is performed with the use of an DFFT (Discrete Fast Fourier Transform) routine, also written for the HP computer system.

Program 1 - Calibration Program

The first program digitizes and reduces the TRI Gage calibration output. The non-linear calibration function used in the data reduction program is obtained as a function of position of the gage relative to the magnet. A curve-fit is performed for each calibration curve, generating a set of coefficients which define the calibration function.

The trajectory of the magnet as it is dropped through the coilform is defined by a velocity at the stop position $V(x_s)$ and an acceleration A (usually slightly less than g, due to frictional forces in the precision drop tower). The data used to evaluate these terms include the start position of the drop $x_o = 0$, the stop position $x_s$, and the experimentally measured elapsed time between two light-port stations $\Delta t = t(x_2)-t(x_1)$. A schematic of the calibration setup is given in Figure 49. Constant acceleration is assumed through the drop, so $V(t) = At$ and

$$x(t) = \frac{1}{2} At^2$$

so

$$t(x_i) = \sqrt{\frac{2x_i}{A}} \quad .$$

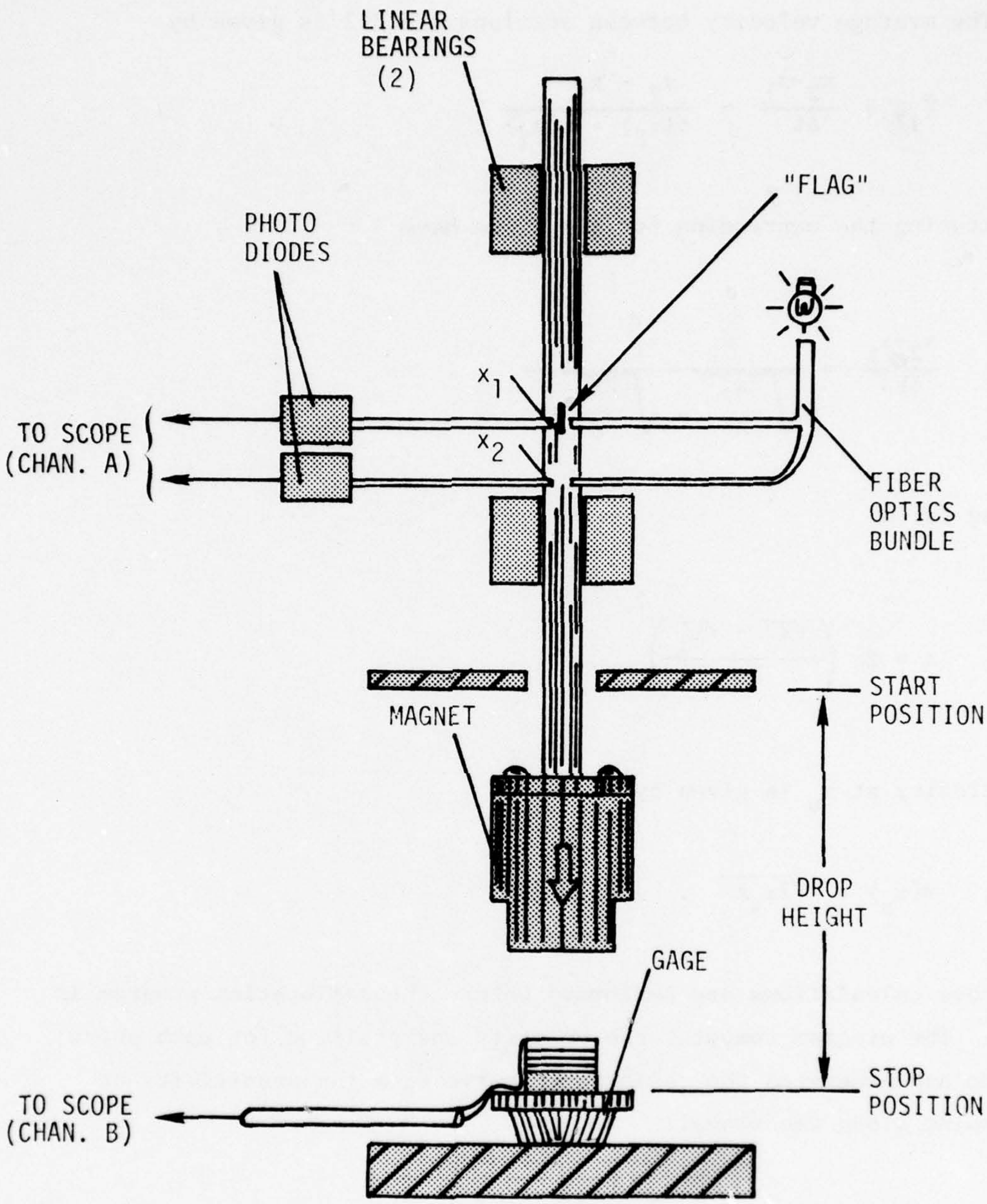


Figure 49. Schematic of the precision drop assembly to calibrate the gage magnets.

The average velocity between stations 1 and 2 is given by

$$\bar{V}_{12} = \frac{x_2 - x_1}{\Delta t} = \frac{x_2 - x_1}{t(x_2) - t(x_1)} \quad .$$

Substituting the expression for $t(x_i)$ we have

$$\frac{x_2 - x_1}{\Delta t} = \frac{x_2 - x_1}{\sqrt{\frac{2x_2}{A}} - \sqrt{\frac{2x_1}{A}}} \quad .$$

Solving for A

$$A = 2 \left( \frac{\sqrt{x_2} - \sqrt{x_1}}{\Delta t} \right)^2 \quad .$$

The velocity at $x_s$ is given by

$$V(x_s) = \sqrt{2 x_s A} \quad .$$

The above calculations are performed before the calibration program is begun. The program computes the velocity and position for each point in time and generates the calibration curve from the sensitivity at each point along the travel:

$$\text{Sensitivity } (x) = \frac{\text{Gage Output } (x)}{\text{Velocity } (x)} \quad .$$

A coordinate transformation is performed with x as the distance from the stop $x_s$. The digitized gage output versus time points are transformed to the calibration curve (versus x) by the following equations.

$$\text{Calibration } (x(t)) = \frac{\text{Gage Output (t)}}{\text{Velocity (t)}}$$

where $x(t) = \frac{1}{2} A \ (t_s - t)^2 + V(x_s) \ (t_s - t)$

and $V(t) = V(x_s) - A(t_s - t)$ .

A typical calibration trace and the resulting calibration curve is given in Figure 50. An exact curve fit of the form

$$s(x) = \frac{A_1 + A_2 x + A_3 x^2 + A_4 x^3}{1 + A_5 x + A_6 x^2}$$

is performed to 6 user chosen points on the curve. The six curve-fit coefficients, $A_1$ through $A_6$, are used by the data reduction program.

Program 2 - Data Reduction Program

The second program uses the calibration coefficients generated by Program 1 and the digitized trace of gage output versus time. Specific inputs include (initial position of the coilform relative to the magnet), (1) the initial x, (2) the mass of the specimen, and (3) the radius of the specimen (exposure area). The program proceeds to solve for the

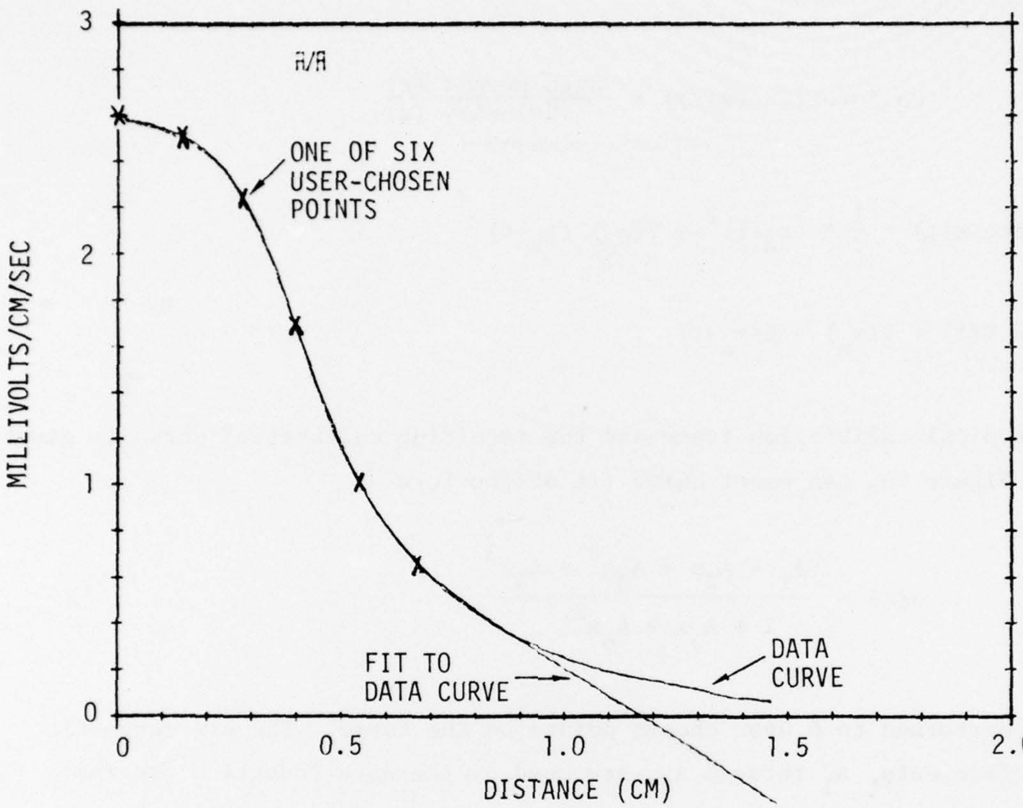


Figure 50. Calibration curve for an early magnet system showing the method of fitting the data.

velocity as a function of time and distance by using an explicit scheme to compute the x-t trajectory described as follows.

At $x_o$, the starting position, the initial velocity is 0. The gage sensitivity at that point is solved using the curve-fit coefficients:

$$s(x_o) = \frac{A_1 + A_2 x_o + A_3 x_o^2 + A_4 x_o^3}{1 + A_5 x_o + A_6 x_o^2}$$

these coefficients are also used to give the derivation of the gage sensitivity at the first point:

$$S^1(x_o) = \frac{d\, s(x_o)}{d\, x_o} = \frac{\left[\left(1 + A_5\, x_o + A_6\, x_o^2\right)\left(A_2 + 2A_3\, x_o + 3A_\mu\, x_o^2\right) - \left(A_1 + A_2\, x_o + A_3\, x_o^2 + A_\mu\, x_o^3\right)\left(A_5 + 2A_6\, x_o\right)\right]}{\left(1 + A_5\, x_o + A_6\, x_o^2\right)^2}$$

The digitized data consists of a set of gage outputs G versus time t points: $\{G_i,\ t_i,\ i = 1, n\}$. The average velocity of first time step $t_1$ is given by

$$\bar{V}_1 = \frac{\left[-s(x_o) + \sqrt{s(x_o)^2 - (t_1 - t_o)\, s'(x_o)\, (G_1 + G_o)}\right]}{\left[(t_1 - t_o)\, s'(x_o)\right]}$$

This equation is derived from the differential form of a Taylor series expansion and includes second order terms. If $s^1(x_o)$ is also zero, the alternative first order equation is used:

$$\bar{V}_1 = \frac{(G_1 + G_o)}{2} \bigg/ s(x_o)$$

The displacement at $t_1$ is

$$x_1 = x_o + \bar{V}_1(t_1 - t_o) \quad .$$

This scheme is used sequentially through the data to yield the velocity as a function of time and distance, recomputing the sensitivity and derivative as x changes.

Given the mass M and radius R of the specimen, the total impulse delivered as a function of time or distance is computed directly from the velocity:

$$I = \frac{VM}{\pi R^2} \quad .$$

Program 3 - Discrete Fast Fourier Transform (DFFT) Data Smoothing Program

A DFFT routine[6] has been modified to remove periodic vibrations from the data traces. In addition to providing a record minimizing gage

artifacts, this technique allows further differentiation of the data without large oscillations. The spectrum of a sequence of data is obtained from the discrete Fourier Transform. The inverse discrete Fourier transform allows the data to be computed from the spectrum. The Fast Fourier Transform has been used to implement the above two transforms for any sequence whose length is a power of two.

An example of the application of this program is given in Figure 51. Figure 51a is a data trace with oscillations. The DFFT routine generates the frequency spectrum of this data (Figure 51b). The frequency structure in this plot between 60 and 110 kH is eliminated at the direction of the user (a smooth curve replaces the section between the two inside x's). The inverse DFFT is then computed and given in Figure 51c and a superposition over the original data is given in Figure 51d. The smoothed velocity-time data is used to calculate smoothed impulse-time and may be differentiated to obtain pressure-time (see, for example, Figure 42b in the Electron-Beam Test Series Section).

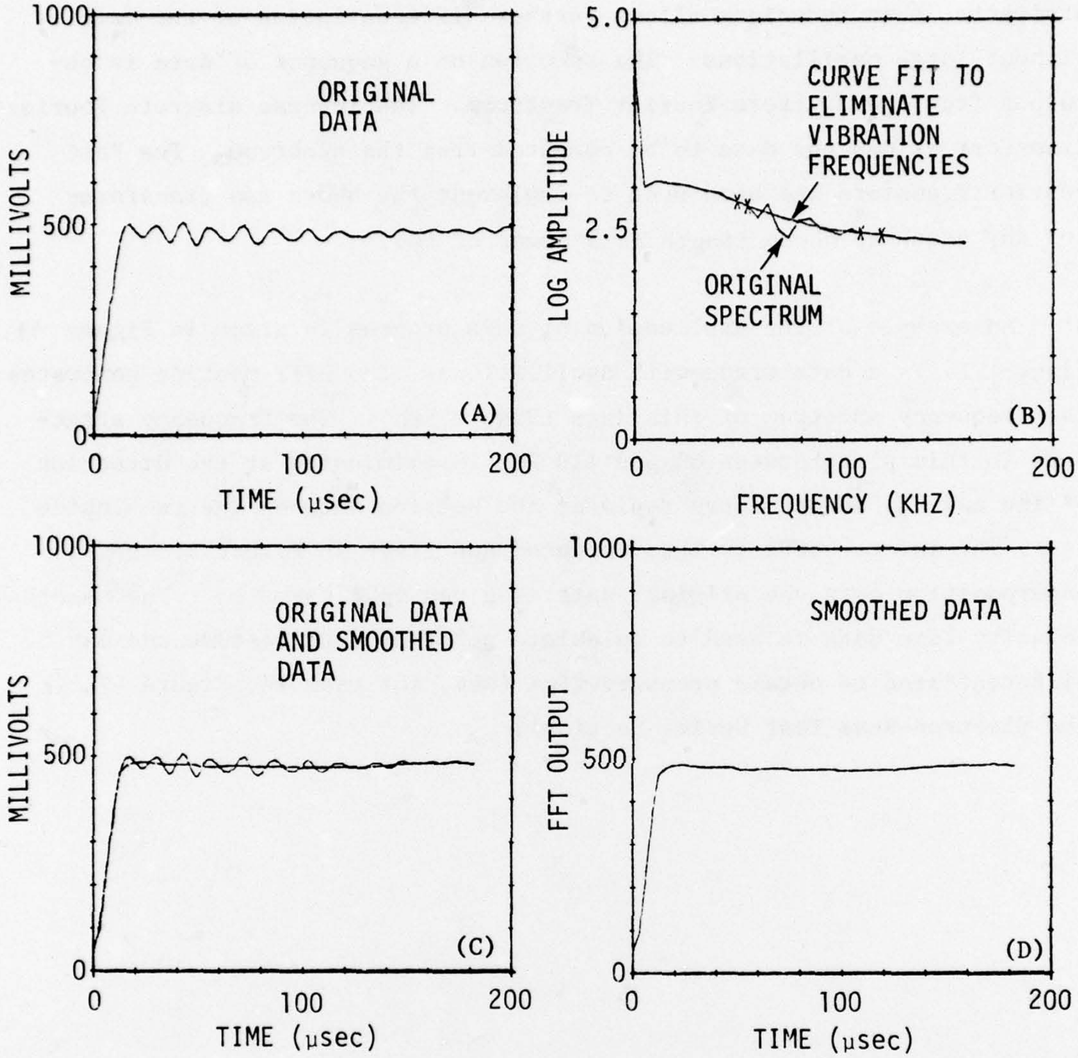


Figure 51. An example of the ability of the FFT analysis to eliminate vibrations caused by gage from the data.

# SECTION IX

## CONCLUSIONS

The gage development program has produced a gage potentially capable of operating in the difficult configurations necessitated by the tamped impulse experiments of an underground nuclear test. The response of gage to short duration impulses is in the range of 10-15 μsec and the impulse range covered is ∿0.5 to 20 ktaps.

The anti-weld and anti-jam features of the gage, while complicating both the gage design and post-test analysis, are thought necessary for proper gage operation in an environment of molten metal, high pressure metallic vapors, and high amplitude stress waves. The electron-beam test series conducted to proof test the gage indicated the ability of the gage to perform in a radiation environment approximating, in many ways, the environment to be experienced on the nuclear test.

Because of our inability to exactly reproduce UGT loading conditions in the laboratory, the final proof test of the gage will be in an underground test. Results of this test may provide guidelines for future gage development. Three areas of concern were noted during the present program:

1. Gage vibrations, induced at the specimen surface by high amplitude stress waves, produce periodic oscillations in the gage output. Although these oscillations were small in lab tests of the final design and a large portion of them are removable by Fast Fourier Transform deconvolution techniques, the removal is less likely to be complete at the higher stresses and risetimes expected in the field.

2. Delamination of the plasma-sprayed specimen from the stainless-steel substrate is possible, although both measurements and calculations indicate it is unlikely. Partial delamination would lessen accuracy but is not a cause of major concern. Complete delamination may make it impossible to accurately calculate the impulse and pressure-time history from the recorded gage output.

3. Metallic vapors escaping past interior seals make post-test analysis of records more complicated. Inaccuracies arising from this source range 5—15% on the raw data, with subsequent analysis reducing this figure to 5-10%.

The advantages of having a gage such as the TRI gage available for time-resolved impulse measurements include:

1. Time resolution of 10-15 μsec covers a largely unexplored range of impulse measurements bounded by the stress gages (<5 μsec) and other recoil gages (>50 μsec). Recording time is relatively long, from 300-1500 μsec, depending on impulse.

2. Measurements can be made over a wide dynamic range (impulses from 0.5 to 20 ktaps and pressures from bars to tens of kilobars).

3. Measurements can be made with dense metallic samples in nuclear environments and with a large variety of metallic and non-metallic specimens in electron-beam and laser environments. Different configurations of the basic gage are available to

allow exposure of low-Z materials in nuclear environments and to decrease the lower limits of the impulse range to <0.5 ktaps.

Several possible improvements to the gage indicated by the laboratory studies may be implemented if problems arise in underground tests. In particular, the bi-metallic coilform design, using a slightly porous magnesium alloy to surround the pickup coils and to dampen vibrations, may prove useful to reduce noise.

Exploding foil generated waves would provide a good simulation of the fast rising wave forms expected. Experiments late in this program indicated electrical noise reduction techniques may make this possible.

The data analysis program for removing periodic oscillations in the gage output which are caused by the gage itself and are not indicative of the pressure-time history at the gage surface is a useful method of treating a variety of mechanical and electrical data. Although care must be taken not to remove real information with the technique, proper application gives smoothed results much more representative of the forces measured.

## SECTION X

## ACKNOWLEDGMENTS

Mr. D. Hanner of LLL provided numerous computer calculations and considerable guidance throughout the effort. Dr. G. Dzakowic of the same laboratory furnished both his pulsed laser equipment and Mr. J. Claar to operate it. Dr. E. Fitzgerald of McDonnell-Douglas Aircraft Corporation was helpful in defining the UGT nuclear test matrix and the operating parameters of the gage.

At Effects Technology, Inc., Mr. V. Hall conducted the H.E. tests and Mr. J. Wogulis strained his eyesight digitizing dozens of oscillographs for analysis. Mr. D. Sangster devised the data analysis and data deconvolution programs.

Mr. N. Froula and Mr. E. Stretanski of K-Tech Corporation (now with Corrales Applied Physics Company) provided their very capable services in conducting the electron-beam tests on the Boeing FX-75 machine.

## REFERENCES


1. L.W. Kennedy and O.E. Jones, "Longitudinal Wave Propagation in a Circular Bar Loaded Suddenly by a Radially Distributed End Stress," J. Appl. Mech., (September, 1969).

2. L. Abbatiello, Union Carbide Y-12 plant, private communication.

3. See, for instance, S. Timoshenko, Vibration Problems in Engineering, p. 439, D. Van Nostrand Co., (third edition, 1955).

4. R. Stone, "A Digital Velocity Transducer," Rev. Sci. Instru., 45 (1974).

5. N.H. Froula, "Summary of FX-75 E-Beam Test Series," KTech Corp. report TR 77-03 (1977).

6. J. Markel and G. Gray, Linear Prediction of Speech, Springer-Verlag (1976).

7. Adamski, J.L., Lempriere, B.M., and Schrader, J.E., Advanced Electron Beam Diagnostics, The Boeing Co., TR-D180-19431-1, to be published as an Air Force Weapons Laboratory Technical Report.

# DISTRIBUTION LIST

DEPARTMENT OF DEFENSE

Assistant to the Secretary of Defense
Atomic Energy
ATTN: Executive Assistant

Defense Advanced Rsch. Proj. Agency
ATTN: TIO

Defense Documentation Center
12 cy ATTN: DD

Defense Intelligence Agency
ATTN: DT-2

Defense Nuclear Agency
ATTN: SPSS
ATTN: STSP
ATTN: SPTD
ATTN: SPAS
ATTN: DDST
4 cy ATTN: TITL

Field Command
Defense Nuclear Agency
ATTN: FCPR
ATTN: FCTMD

Field Command
Defense Nuclear Agency
Livermore Division
ATTN: FCPRL

Joint Chiefs of Staff
ATTN: J-5, Nuclear Division
ATTN: SAGA/SFD
ATTN: J-5, Force Planning & Program Div.
ATTN: SAGA/SSD

Joint Strat. Tgt. Planning Staff
ATTN: JPTM
ATTN: JLTW-2

Under Secy. of Def. for Rsch. & Engrg.
Department of Defense
ATTN: Strategic & Space Systems (OS)

DEPARTMENT OF THE ARMY

BMD Advanced Technology Center
Department of the Army
ATTN: ATC-T, M. Capps

BMD Program Office
Department of the Army
ATTN: Technology Division

BMD Systems Command
Department of the Army
ATTN: BMDSC-H, N. Hurst

Deputy Chief of Staff for Ops. & Plans
Department of the Army
ATTN: DAMO-NCZ

DEPARTMENT OF THE ARMY (Continued)

Deputy Chief of Staff for Rsch. Dev. & Acq.
Department of the Army
ATTN: DAMA-CSS-N

Harry Diamond Laboratories
Department of the Army
ATTN: DELHD-N-P, J. Gwaltney
ATTN: DELHD-N-RBC, D. Schallhorn
ATTN: DELHD-N-P

U.S. Army Ballistic Research Labs.
ATTN: DRDAR-BLV, W. Schuman, Jr.
ATTN: DRDAR-BLE, J. Keefer
ATTN: DRDAR-BLV

U.S. Army Material & Mechanics Rsch. Ctr.
ATTN: DRXMR-HH, J. Dignam

U.S. Army Materiel Dev. & Readiness Cmd.
ATTN: DRCDE-D, L. Flynn

U.S. Army Missile R&D Command
ATTN: DRDMI-TKP, W. Thomas

U.S. Army Nuclear & Chemical Agency
ATTN: Library

U.S. Army Research Office
ATTN: Technical Library

DEPARTMENT OF THE NAVY

Naval Research Laboratory
ATTN: Code 6770, G. Cooperstein
ATTN: Code 2627
ATTN: Code 7908, A. Williams

Naval Sea Systems Command
ATTN: SEA-0351
ATTN: SEA-0352, M. Kinna

Naval Surface Weapons Center
ATTN: Code F31
ATTN: Code R15, J. Petes
ATTN: Code K06, C. Lyons
ATTN: Code K06

Naval Weapons Evaluation Facility
ATTN: L. Oliver

Office of the Chief of Naval Operations
ATTN: Op-604E14, R. Blaise
ATTN: Op-981
ATTN: Op-604

Strategic Systems Project Office
Department of the Navy
ATTN: NSP-273
ATTN: NSP-272

DEPARTMENT OF THE AIR FORCE

Aeronautical Systems Division, AFSC
ATTN: ASD/ENFTV

Air Force Materials Laboratory
ATTN: MBC, D. Schmidt
ATTN: MBE, G. Schmitt
ATTN: LLM, T. Nicholas

Air Force Rocket Propulsion Laboratory
ATTN: LKCP, G. Beale

Air Force Systems Command
ATTN: XRTO
ATTN: SOSS

Air Force Weapons Laboratory, AFSC
ATTN: DYS
ATTN: DYV
ATTN: NT
ATTN: DYT
ATTN: SUL

Deputy Chief of Staff
Research, Development, & Acq.
Department of the Air Force
ATTN: AFRDQSM
ATTN: AFRD

Foreign Technology Division, AFSC
ATTN: TQTD
ATTN: SDBS, J. Pumphrey
ATTN: SDBG

Space & Missile Systems Organization/DY
Air Force Systems Command
ATTN: DYS

Space & Missile Systems Organization/MN
Air Force Systems Command
ATTN: MNNR
ATTN: MNNH

Space & Missile Systems Organization/RS
Air Force Systems Command
ATTN: RSMA
ATTN: RSS
ATTN: RSSE

Strategic Air Command/XPFS
Department of the Air Force
ATTN: XPQM
ATTN: XPFS
ATTN: DOXT
ATTN: XOBM

DEPARTMENT OF ENERGY

Department of Energy
ATTN: Document Control for OMA/RD&T

DEPARTMENT OF DEFENSE CONTRACTORS

Acurex Corp.
ATTN: J. Huntington

Battelle Memorial Institute
ATTN: M. Vanderlind

DEPARTMENT OF DEFENSE CONTRACTORS (Continued)

Aerospace Corp.
ATTN: R. Crolius
ATTN: R. Mortensen
ATTN: W. Mann
ATTN: R. Strickler

Avco Research & Systems Group
ATTN: W. Broding
ATTN: J. Gilmore
ATTN: P. Grady
ATTN: J. Stevens
ATTN: G. Weber
ATTN: Document Control

Boeing Co.
ATTN: B. Lempriere

California Research & Technology, Inc.
ATTN: K. Kreyenhagen

Effects Technology, Inc.
ATTN: R. Wengler/R. Bick
ATTN: W. Naumann
20 cy ATTN: W. Isbell

Ford Aerospace & Communications Corp.
ATTN: P. Spangler

General Electric Co.
Space Division
ATTN: G. Harrison
ATTN: D. Edelman

General Electric Co.
Re-Entry & Environmental Systems Div.
ATTN: P. Cline

General Electric Co.-TEMPO
ATTN: DASIAC

General Research Corp.
ATTN: R. Rosenthal

Institute for Defense Analyses
ATTN: Classified Library
ATTN: J. Bengston

Ion Physics Corp.
ATTN: R. Evans

Kaman AviDyne
ATTN: R. Ruetenik

Kaman Sciences Corp.
ATTN: R. Sachs/R. O'Keefe
ATTN: F. Shelton
ATTN: T. Meagher

Lockheed Missiles & Space Co., Inc.
ATTN: O. Burford
ATTN: R. Walls

Lockheed Missiles and Space Co., Inc.
ATTN: F. Borgardt

Lockheed Missiles and Space Co., Inc.
ATTN: T. Fortune

DEPARTMENT OF DEFENSE CONTRACTORS (Continued)

Martin Marietta Corp.
    ATTN: L. Kinnaird

McDonnell Douglas Corp
    ATTN: L. Cohen
    ATTN: H. Berkowitz
    ATTN: M. Schneider
    ATTN: J. Peck

Pacific-Sierra Research Corp.
    ATTN: G. Lang

Physics International Co.
    ATTN: J. Shea

Prototype Development Associates, Inc.
    ATTN: J. McDonald
    ATTN: N. Harington

R & D Associates
    ATTN: W. Graham, Jr.
    ATTN: P. Rausch
    ATTN: C. MacDonald
    ATTN: F. Field

Rand Corp.
    ATTN: R. Rapp

Science Applications, Inc.
    ATTN: O. Nance
    ATTN: W. Yengst

Science Applications, Inc.
    ATTN: W. Seebaugh
    ATTN: W. Layson

Southern Research Institute
    ATTN: C. Pears

SRI International
    ATTN: H. Lindberg
    ATTN: D. Curran
    ATTN: G. Abrahamson

DEPARTMENT OF DEFENSE CONTRACTORS (Continued)

Systems, Science & Software, Inc.
    ATTN: T. McKinley
    ATTN: G. Gurtman
    ATTN: R. Duff

Terra Tek, Inc.
    ATTN: S. Green

TRW Defense & Space Sys. Group
    ATTN: J. Farrel
    ATTN: W. Wood
2 cy ATTN: P. Dai/D. Jortner

TRW Defense & Space Sys. Group
    ATTN: L. Berger
    ATTN: V. Blankenship
    ATTN: W. Polich

DEPARTMENT OF ENERGY CONTRACTORS

Lawrence Livermore Laboratory
    ATTN: Document Control for L-125, J. Keller
    ATTN: Document Control for L-92, C. Taylor
    ATTN: Document Control for L-96, L. Woodruff
    ATTN: Document Control for D. Hanner

Los Alamos Scientific Laboratory
    ATTN: Document Control for R. Skaggs
    ATTN: Document Control for R. Dingus
    ATTN: Document Control for D. Shover
    ATTN: Document control for J. McQueen/
    J. Taylor

Sandia Laboratories
    ATTN: Document Control for C. Broyles
    ATTN: Document Control for R. Boade
    ATTN: Document Control for C. Mehl
    ATTN: Document Control for M. Cowan

Sandia Laboratories
Livermore Laboratory
    ATTN: Document Control for T. Gold
    ATTN: Document Control for H. Norris, Jr.